Computer simulation of the pure and defective surface properties of -aluminium oxide, lanthanum cuprate and neodymium cuprate

Kenway, P. R.

Award date:
1991

Awarding institution:
University of Bath

Computer Simulation of the Pure and Defective Surface properties of α-Aluminium Oxide, Lanthanum Cuprate and Neodymium Cuprate

submitted by **P.R.Kenway**

for the degree of PhD

at the University of Bath

1991

ProQuest LLC
789 East Eisenhower Parkway
P.O. Box 1346
Ann Arbor, MI 48106-1346

Abstract

The aim of the work described in this thesis is to investigate the pure and defective surface properties of ceramic oxides, specifically aluminium oxide, lanthanum cuprate and neodymium cuprate using computer simulation techniques. α-Al_2O_3 is a model system for ceramic oxides and is used to establish the reliability of the techniques. An important unresolved question that is addressed is how dopants control the surface properties and sintering behaviour of α-Al_2O_3. La_2CuO_4 and Nd_2CuO_4 are important because they are the parent compounds of high temperature superconductors. The structure and composition of their interfaces play a decisive role in influencing the surface conductivity and the intergranular weak links.

Chapter 1 provides an introduction to recent developments in ceramic oxides and a brief discussion on the current state of experimental and simulation techniques for determining their surface properties. The following two chapters (Chapter 2 and 3) outline the theoretical methods and the methods used for deriving the potential models employed in this thesis respectively. The calculation of surface Madelung energies and surface vibrational properties are described. The use of potentials, originally derived from bulk properties, in surface calculations is discussed.

The remainder of this thesis presents the calculated results. In Chapter 4, the segregation of magnesium and calcium to the basal and $\{10\bar{1}0\}$ prism surfaces of α-Al_2O_3 is discussed. Calculations on surface and segregation potential energies are compared to surface segregation free energies. The results establish the importance of the vibrational entropy contribution to calculated free energies in corundum structured oxides.

In Chapter 5, the structures and energies of the {100} and {001} surfaces of La_2CuO_4 and Nd_2CuO_4 are considered. They are compared to the calculations on the energies of the higher index surfaces of the two cuprates. The results are used to

demonstrate that an adequate account of surface relaxation must be included when comparing the relative stabilities of ternary oxide surfaces.

The formation energies of intrinsic defects and the solution energies of divalent and tetravalent impurities at the {100} and {001} surfaces of La_2CuO_4 and Nd_2CuO_4 are discussed in Chapter 6. The methods are used to calculate the non-stoichiometry and the composition of the surfaces and the results are compared with bulk behaviour. Space charge effects in the two cuprates are also discussed.

Acknowledgements

First, I would like to thank Dr. S.C.Parker for his help, advice and support throughout the course of my work.

I would also like to thank my CASE supervisor, Dr. W.C.Mackrodt for his help, advice and thought provoking discussion.

I would like to acknowledge Dr. N.L.Allan for many useful comments and discussions.

I am grateful to the Science and Engineering Research Council and Imperial Chemical Industries Ltd. for financial support and the provision of computer time.

The contribution of my friends and colleagues are numerous and gratefully acknowledged. I would particularly like to thank Don, Pete, Richard and Mandy, my parents and my brother and sister for their support, understanding and encouragement.

Finally, I would like to thank Dr. A.Wall for her help in assembling this thesis.

Contents

Chapter 1

Introduction

A knowledge of the composition, structure and energetics of ceramic oxide surfaces is a prerequisite for understanding many processes in materials science. Such processes include catalysis, corrosion, crystal growth and high T_C behaviour. Despite recent developments in surface analytical techniques (1,2), however, data on the surface atomic arrangements of oxides are still difficult to obtain and hence sparse (3). Atomistic simulation is therefore not only of use in the interpretation of existing experimental data, but also in the investigation and prediction of surface properties outside usual or accessible experimental conditions. A brief review of recent developments in experiment and simulation is given after a discussion on why interest in ceramic oxides has increased dramatically over the last few years.

1.1 Recent Developments

1.1.1 Ceramic Oxides

Among other properties, ceramic oxides exhibit a wide range of electrical behaviour (4). For example, ceramic oxides include the best insulators (e.g. Al_2O_3 with a band gap of about 9.9 eV (5)); both wide band gap and narrow band gap semiconductors (e.g. TiO_2 and Ti_2O_3 with band gaps of about 3.0 eV (6) and 0.1 eV (4) respectively); metals (e.g. V_2O_3, Na_xWO_3 and ReO_3 (7)) and superconductors (e.g. $BaPb_{1-x}Bi_xO_3$ (8)). However, until recently the material with the highest superconducting critical temperature (T_C) of about 22 K was not a ceramic oxide, but the alloy Nb_3Ge (9,10). This situation changed dramatically in 1986 when Bednorz

and Mueller (11) discovered superconductivity in a phase of composition La-Ba-Cu-O with a $T_C > 30$ K. Soon afterwards, it was shown that the phase $La_{2-x}Ba_xCuO_4$, which possesses the K_2NiF_4 structure, was responsible for this superconductivity (12). Further research into new high temperature ceramic superconductors concentrated on similar layered perovskites. Replacement of barium by strontium led to an increase in T_C (13) and this could also be achieved by the application of pressure (14). Work on systems within the phase, Y-Ba-Cu-O, by Wu et al. (15) led to the discovery that superconductivity could be sustained above the boiling point of liquid nitrogen (77 K). The structure (16,17) of this 'new' quaternary high temperature superconductor was different from that of $La_{2-x}Ba_xCuO_4$, but still included two dimensional planes of CuO_2. Compounds of bismuth also form layered compounds (18) and this feature prompted Michel et al. (19) to search for superconductivity in Bi-Sr-Cu-O phases. The resulting material, $Bi_2Sr_2Cu_2O_7$ has a low T_C of 22 K but this can be increased significantly by doping with calcium (20,21,22). Sheng and Herman (23) noted that the T_C was also influenced by the size and charge of the lanthanide ions, rather than by their magnetic properties. They, therefore, replaced the rare earth cation with thallium which, in the trivalent state, has a similar ionic radius to Eu^{3+}. The resulting thallium (III) barium copper oxide phase had a T_C of about 81 K. The critical temperature of this phase was subsequently increased by Hazen et al. (24) and Parkin et al. (25) by doping with calcium. The discovery of both the bismuth and thallium compounds showed that lanthanides were not needed for high temperature superconductors. The use of thallium brought its own problems because thallium oxide is not only volatile but also toxic.

Two common features of the high T_C compounds mentioned so far are (a) they all contain copper oxide planes and (b) under the right conditions they are hole or p-type superconductors. However, it has been shown recently that CuO_2 planes are not an essential prerequisite for high T_C superconductivity. This is exemplified by the

ceramic superconductors $La_{2-x}Sr_xNiO_4$ (26), with the K_2NiF_4 structure and $Ba_{1-x}K_xBiO_3$ (27), which has a three dimensional network of BiO bonds. The other common feature of the above compounds i.e. p-type superconductivity was also demonstrated to be non-essential for high T_C behaviour by Tokura et al. (28,29). They found evidence for electron or n-type superconductivity in the cuprates $RE_{2-x}Ce_xCuO_{4-y}$ (RE=Pr, Nd, Sm). Further work using thorium instead of cerium (30) also led to n-type behaviour as did fluorine substituted for oxygen (31).

The phase of stoichiometric composition $Tl_2Ba_2Ca_2Cu_3O_x$, originally identified by Parkin et al. (25) over two years ago, presently holds the record for the highest T_C of 125 K.

1.1.2 Experiment

The surfaces and grain boundaries of ionic solids in general, and metal oxides in particular, are difficult to investigate and characterise experimentally. This is partly because it is difficult to obtain pure well characterised single crystals (32). A further deficiency is the surface charging problem. Charged particles used in many surface spectroscopic techniques interact with the surfaces of ceramic oxides making it difficult to resolve and interpret experimental data (33). This problem has recently been reduced by increasing the resolution, sensitivity and detection limits of electron optic techniques and has facilitated the probing of the outermost layers of the surface.

The current methods used in surface analysis can be divided roughly into those which give information on the chemical composition, the lattice structure, and the energetics of surfaces. The latter can be further sub-divided into investigations on electrons and phonons at surfaces. Determination of the lattice structure can be achieved either by exploiting the periodic long-range nature of the surfaces e.g. LEED (low energy electron diffraction) (34) or by investigating the surface structure with

atomic resolution e.g. STM (Scanning Tunnelling Microscope) (1,35) and AFM (Atomic Force Spectroscopy) (2). The composition and energetics of surfaces can also be determined by investigating their interaction with electrons, ions, atoms and photons. Some of these techniques are non-destructive e.g. AES (Auger Electron Spectroscopy) (36) while others erode the surface structure (37). This latter effect can be used to investigate the composition with depth from the surface (37). A recent review of the versatility of the available surface techniques is given by Hirschwald (38).

1.1.3 Lattice Simulation

The development of efficient computer simulation techniques over the last twenty years has provided a notable complement to experiment in determining the properties of a wide range of materials. Initially, the defect structures of simple binary ionic solids were investigated. Norgett and Lidiard (39) showed that atomistic simulation could be used to reliably calculate the bulk defect properties of alkali halides. Catlow (40) extended the scope of atomistic simulation to include fluorite structured halides and oxides. The methods were further used to study both cubic (41) and non-cubic (42) oxides and, more recently, to study ternary (43) and multi-component systems (44). The development of surface codes built on the knowledge gained from the bulk defect simulation techniques. Initially surface studies were confined to alkali halides (45). Following the determination of reliable potentials describing the interatomic forces in ionic solids, cubic (46) and non-cubic binary oxide surfaces (47) were investigated.

The work on interfaces has not just been confined to the study of the structure and composition of free surfaces. Duffy and Tasker (48,49) have used atomistic simulation to investigate tilt grain boundaries in NiO and cation boundary diffusion

(50). The scope of atomistic simulation has also been extended by Stoneham and Tasker (51) in their investigation of the structure of the boundary between the different dielectrics NiO and BaO. The inclusion of image charge effects, which influence many of the properties of interfaces between metals and ionic solids (52) will further increase the understanding of such processes as catalysis and corrosion (53).

Most simulations have neglected the vibrational contribution to the free energy and hence give structures and energies at 0 K. Calculations at elevated temperatures have been facilitated by Parker and Price (54) who developed a computer code based on lattice statics and dynamics to calculate the solid state phase diagrams of minerals (55). A similar approach has been used by Tasker (56) and Masri et al. (57) to study the vibrational properties of the {001} surfaces of LiF and MgO respectively.

The critical test of the quality of atomistic simulations is their ability to reliably reproduce the results of experimentally well-characterised systems. Where such comparisons have been made for surface segregation (58) the agreement is excellent. The inclusion of temperature effects has also led to some interesting and perhaps surprising observations e.g. some zeolites are predicted (59) to contract on heating and this has recently been confirmed by experiment (60).

1.2 Aims of this Work

Previously, atomistic simulations have been used to calculate the composition, structure and stability of binary halide (45) and oxide (46,47) surfaces. Even though the vibrational contribution to the free energy of the lattice has been neglected in these simulations the agreement with experiment has been favourable (58). This implies that the calculated free energies are dominated by the internal energy of the

lattice and this has been confirmed by simulations on cubic systems (57,61). The aim of the work described in Chapter 4 is to extend atomistic simulations to include the calculation of the free energy of non-cubic oxide surfaces. Calculations of the surface potential energies of α-Al_2O_3 and segregation potential energies of calcium and magnesium in α-Al_2O_3 are discussed and compared with surface and segregation free energies. Small additions of MgO are known to promote the sintering of alumina to full density, whereas the addition of CaO does not (62). The reason for this is still unclear, but is thought to involve differences in impurity segregation behaviour (62).

Multicomponent oxides are also important in materials research (63). For polycrystalline applications, the structure and composition of interfaces will influence the properties of these oxides (64). In Chapter 5 and Chapter 6, calculations on the surface structure and composition of two important ternary oxides are described. These are La_2CuO_4 and Nd_2CuO_4. In their stoichiometric forms they are semiconductors, but when doped they become superconducting (see section 1.1.1). Previous atomistic simulations on the parent compounds of these high T_C oxides have been concerned with their bulk defect properties. The calculated defect chemistry demonstrates why the materials properties of these two compounds are different (65). An understanding of their surface properties will also be important because they form superconducting weak links in the granular materials (66,67).

Chapter 2

Theoretical methods

2.1 Introduction

In this chapter, the methods that are used in this thesis to determine lattice and defect energies of ionic and semi-ionic solids are described. The calculation of the lattice energy is complicated because of the long range nature of the Coulomb sums. This difficulty can be overcome by using the Ewald method (68) and is described in section 2.2. The methods can then be used to determine the energetically preferred structure by adjusting the ion positions until the lattice energy is at a minimum. This is achieved by an iterative Newton-Raphson technique which is discussed in section 2.3. The treatment of isolated point defects uses a related procedure to find the minimum defect energy in the bulk. This was achieved by Norgett (69) who developed a computer code for partitioning the crystal into two regions surrounding the defect. Many accounts (70,71) of this method are available and so only the salient features of the technique will be given.

When modelling surfaces, two dimensional boundary conditions are used. This has important consequences for simulations, particularly in the calculation of the Coulombic interaction energy. Thus in section 2.5, the way in which the Ewald technique, originally derived for 3-dimensional problems, is adapted to study interfaces is described. This has since become known as the Parry Method (72,73). The treatment of charged defects at surfaces and interfaces is similar to that in 3-dimensions but, again, is complicated by the presence of the boundary. The extra interactions that must be included are given in section 2.6.

Lattice and defect energies calculated by these methods strictly correspond to

potential energies at constant volume and 0 K. They can be extended to include the effects of temperature using lattice dynamics and molecular dynamics. Lattice dynamics is used in this thesis and is described in section 2.7.

2.2 The Coulombic Contribution to the Lattice Energy

The electrostatic or Coulomb term dominates the cohesive energy of ionic or semi-ionic crystals. In 3-dimensions it can be written as:

$$U(\underline{r}_{ij}) = \Sigma_{i \neq j} q_i q_j (\Sigma |\underline{r}_{ij} + \underline{l}_1 a_1 + \underline{l}_2 a_2 + \underline{l}_3 a_3|)^{-1} \quad (2.1)$$

where q_i and q_j are the charges of ions i and j separated by $\underline{r}_{ij}$, $\underline{l}_n$ represent the lattice vectors associated with the 3 dimensional unit cell and a_n are integers. The evaluation of the $\underline{r}_{ij}^{-1}$ term is problematic because it converges slowly with increasing ion separation. However, Ewald showed that by exploiting the periodic nature of the 3 dimensional lattice the electrostatic energy can be converted into two rapidly converging series. This is achieved by separating the identity (74):

$$1/r = 2/\pi^{1/2} \int_0^{\infty} \exp(-r^2t^2)\, dt \quad (2.2)$$

into two terms:

$$1/r = 2/\pi^{1/2} [\int_0^{\eta} \exp(-r^2t^2)\, dt + \int_{\eta}^{\infty} \exp(-r^2t^2)\, dt] \quad (2.3)$$

where t is a variable and η is a parameter chosen to give fast convergence of the final result. The first term, I_1, in equation 2.3 can be transformed into reciprocal space by

Fourier analysis to give:

$$I_1 = 2/\pi^{1/2}\int_0^{\eta} dt\ 1/(2t\pi^{1/2})^3. \int_0^{\infty} d^3\underline{K}\ \exp(-K^2/4t^2)\exp(-i\underline{K}.\underline{r}) \qquad (2.4)$$

The first integral can be evaluated by making the variable change $s = -K^2/4t^2$. The second integral, $\int_0^{\infty} d^3\underline{K}$, can be replaced by a summation over $\underline{K}$ vectors defined so that:

$$\underline{K} = 2\pi(n_1\underline{k} + n_2\underline{k} + n_3\underline{k}) \qquad (2.5)$$

where n_1, n_2 and n_3 are integers. $\underline{k}_1$, $\underline{k}_2$ and $\underline{k}_3$ satisfy the relation $\underline{k}_i\underline{a}_j = \delta_{ij}/N^{1/3}$ where a_i is a fundamental lattice vector, δ_{ij} is the Kroenecker delta (one when i=j but otherwise 0) and N is the number of unit cells in the crystal. The volume per $\underline{K}$ vector is $(2\pi)^3\underline{k}_1.(\underline{k}_2 x \underline{k}_3)$ which is $(2\pi)^3/NV_c$ where V_c is the volume of the unit cell. Thus, I_1 becomes:

$$I_1 = 4\pi/NV_c\ \Sigma_K(1/K^2)\exp(-K^2/4t^2)\ \exp(-i\underline{K}.\underline{r}) \qquad (2.6)$$

The second term, I_2, in equation 2.3 is evaluated in real space using the identity:

$$I_2 = 1/\underline{r}\ \mathrm{erfc}(\eta\underline{r}) \qquad (2.7)$$

where erfc($\underline{r}$) is the complementary error function and is related to erf($\underline{r}$), the error function by:

$$\mathrm{erf}(\underline{r}) = 1 - \mathrm{erfc}(\underline{r}) \qquad (2.8)$$

The Coulombic energy can then be determined by substituting 2.3 into 2.1 once 2.6 and 2.7 have been found. Note that the evaluation of 2.6 can be simplified because the sum $\Sigma_l \exp(-i\underline{K}.\underline{r}_l)$ is zero if the sum over lattice vectors, $\underline{l}$, is complete and vector $\underline{K}$ is other than 2π times a reciprocal lattice vector. When $\underline{K}$ is 2π times a reciprocal lattice vector, which is defined as $\underline{G}$, then the sum over a complete set of lattice sites is N, the number of unit cells in the crystal. The Coulombic contribution to the lattice energy is then:

$$U(\underline{r}_{ijl}) = 4\pi/V \, \Sigma_G \, (1/G^2)\exp(-G^2/4\eta) \, \Sigma_{ij}{}' \, q_i q_j \exp(-i\underline{G}.\underline{r}_{ij})$$

$$+ \Sigma_{ijl}{}' \, q_i q_j \, \mathrm{erfc}(\eta \underline{r}_{ijl})/\underline{r}_{ijl} \qquad (2.9)$$

where the self interaction terms are omitted.

The electrostatic contribution to the cohesive energy of a 2 dimensional lattice can be calculated by an analogous method and this is discussed in section 2.5. In the following section, the approach that is used to determine the minimum energy configuration is discussed.

2.3 Minimisation Method

The minimum energy configuration of the lattice can be determined by either minimising the internal bulk strains or minimising both the bulk and basis strains acting on the unit cell. These alternative methods are referred to as minimisation to constant volume and minimisation to constant pressure respectively. A common feature of both these techniques is the use of the Newton-Raphson variable metric

method (75) which requires the first and second derivatives of the lattice energy with respect to the strains. The convergence of the lattice energy is rapid using this approach. However, when large numbers of ions are considered the calculation may require excessive amounts of computer resources because of the time taken to calculate and store the inverse of the second derivative matrix. The way in which this is incorporated in the constant volume minimisation is now described.

2.3.1 Constant Volume Minimisation

The aim of this approach is to remove the net forces acting on the ions in the lattice. This is achieved by expanding the lattice energy to second order about a point $\underline{r}$ (76):

$$U(\underline{r}') = U(\underline{r}) + \underline{g}^T\underline{\delta} + 1/2\underline{\delta}^T.\underline{\underline{W}}.\underline{\delta} \qquad (2.10)$$

where $\underline{\delta}$ is the displacement of a given ion,

$$\underline{\delta} = \underline{r}' - \underline{r} \qquad (2.11)$$

$\underline{g}$ is the force acting on the ion,

$$\underline{g} = \partial U/\partial \underline{r} \qquad (2.12)$$

and $\underline{\underline{W}}$ is the second derivative matrix:

$$\underline{\underline{W}} = \partial^2 U/\partial \underline{r}\partial \underline{r} \qquad (2.13)$$

By utilising the condition that the net forces on the ions at equilibrium are zero then:

$$\underline{\delta} = -\underline{\underline{W}}^{-1}\underline{g} \qquad (2.14)$$

The minimum energy configuration can be obtained by updating the coordinates by $\underline{\delta}$ over a number of iterations. The inherent difficulties associated with this approach lie with the storage of the inverse of the second derivative matrix, and the time taken to evaluate it. The second problem can be reduced by finding an approximation for $\underline{\underline{W}}^{-1}$ and recalculating $\underline{\underline{W}}^{-1}$ explicitly after a specified number of iterations (75). Equation 2.14 is rewritten as:

$$\underline{\delta} = -\lambda\underline{\underline{H}}.\underline{g} \qquad (2.15)$$

in which $\underline{\underline{H}}$, the Hessian matrix, is set initially to $\underline{\underline{W}}^{-1}$ and λ is a linear parameter. Therefore, for the n+1 iteration the new coordinate positions are given by:

$$\underline{\delta}_n = \lambda_n\underline{\underline{H}}_n.\underline{g}_n \qquad (2.16)$$

with

$$\underline{\delta}_n = \underline{r}_{n+1} - \underline{r}_n \qquad (2.17)$$

Then, using an approximation developed by Davidson (77), Fletcher and Powell (78), the Hessian for the next iteration can be estimated by:

$$\underline{\underline{H}}_{n+1} = \underline{\underline{H}}_n - (\underline{\delta}_n.\underline{\delta}_n^T)/(\underline{\delta}_n^T.\underline{\gamma}_n) - (\underline{\underline{H}}_n.\underline{\gamma}_n).(\underline{\gamma}_n^T.\underline{\underline{H}}_n)/(\underline{\gamma}_n^T.\underline{\underline{H}}_n.\underline{\gamma}_n) \qquad (2.18)$$

where $\underline{\gamma} = \underline{g}_{n+1} - \underline{g}_n$. This approach requires the recalculation of the first derivatives $\underline{g}$ and is much less time consuming than recalculating the second derivative matrix every iteration.

2.3.2. Constant Pressure Minimisation

The aim of the constant pressure energy minimisation is to remove the bulk strains acting on the unit cell as well as the basis strains acting on the ions. The bulk strains are defined by (79):

$$\underline{r}' = (\underline{\underline{I}} + \underline{\underline{\epsilon}})\underline{r} \qquad (2.19)$$

where $\underline{\underline{\epsilon}}$ is the strain in the original coordinates and lattice vectors, $\underline{\underline{I}}$ is the identity matrix and $\underline{r}'$ the resultant coordinates and lattice vectors after applying the strains. The strain can be calculated from Hooke's law (stress is proportional to strain) and requires the determination of the first and second derivatives of the lattice energy with respect to the strain. The first derivative is the stress or mechanical pressure $\underline{P}$, while the second derivatives are the elastic constants $\underline{\underline{C}}$. The strain $\underline{\underline{\epsilon}}$ is then:

$$\underline{\underline{\epsilon}}_j = \underline{P}_j(\underline{\underline{C}})^{-1} \qquad (2.20)$$

where the constant of proportionality $\underline{\underline{C}}^{-1}$ is the elastic compliance tensor.

The mechanical pressure is calculated from:

$$\underline{P}_j = dU/d\underline{\underline{\epsilon}}_j = (dU/d\underline{r}).(d\underline{r}^2/d\underline{\underline{\epsilon}}_j).(d\underline{r}/d\underline{r}^2) \qquad (2.21)$$

where $d\underline{r}^2/d\underline{\underline{\epsilon}}_j$ is evaluated from the square equation 2.19 at zero strain. The

transformation of $\underline{r}$ to $\underline{r}$' will also result in changes in the reciprocal lattice vectors and unit cell volumes. The expressions describing these changes are analogous to equation 2.19 and are given by:

$$\underline{G}' = (\underline{\underline{I}} + \underline{\underline{\epsilon}})^{-1}.\underline{G} \qquad (2.22)$$

and

$$V'_c = \det(\underline{\underline{I}} + \underline{\underline{\epsilon}}).V_c \qquad (2.23)$$

The second derivatives of the lattice energy with respect to both the bulk and basis strains are evaluated by writing equation 2.10 as:

$$U(\underline{r}') = U(\underline{r}) + 1/2\underline{\delta}^T.\underline{\underline{W}}_{rr}.\underline{\delta} + \underline{\delta}^T.\underline{\underline{W}}_{r\epsilon}.\Delta\underline{\underline{\epsilon}}$$

$$+ 1/2\Delta\underline{\underline{\epsilon}}.\underline{\underline{W}}_{\epsilon\epsilon}.\Delta\underline{\underline{\epsilon}} \qquad (2.24)$$

where $\underline{\underline{W}}_{r\epsilon} = \partial^2U/\partial\underline{r}\partial\underline{\underline{\epsilon}}$ and $\underline{\underline{W}}_{\epsilon\epsilon} = \partial^2U/\partial\underline{\underline{\epsilon}}\partial\underline{\underline{\epsilon}}$. As before, applying the equilibrium condition gives:

$$\underline{\delta} = -(\underline{\underline{W}}_{rr}^{-1}.\underline{\underline{W}}_{r\epsilon}.\Delta\underline{\underline{\epsilon}}) \qquad (2.25)$$

Then

$$U(\underline{r}') = U(\underline{r}) + 1/2\Delta\underline{\underline{\epsilon}}.(\underline{\underline{W}}_{\epsilon\epsilon} - \underline{\underline{W}}_{\epsilon r}.\underline{\underline{W}}_{rr}^{-1}.\underline{\underline{W}}_{r\epsilon}).\Delta\underline{\underline{\epsilon}} \qquad (2.26)$$

The elastic constants are defined as the second derivative of the lattice energy with respect to strain and normalised with respect to the unit cell volume. They are therefore given by:

$$\underline{\underline{C}} = 1/V_c(\underline{\underline{W}}_{\epsilon\epsilon} - \underline{\underline{W}}_{\epsilon r}.\underline{\underline{W}}_{rr}^{-1}.\underline{\underline{W}}_{r\epsilon}) \qquad (2.27)$$

Thus substituting equations 2.27 and the relationships for the mechanical pressure (equations 2.20, 2.21) into equation 2.19 the strain can be found to give the new lattice vectors and coordinate positions. As the energy is not harmonic the bulk strains must be recalculated over a few iterations before the minimum energy configuration is reached.

2.4 Calculation of Point Defect Energies in a 3 Dimensional Lattice

The major problem associated with the calculation of defect energies is the treatment of relaxation about the defect. This can be overcome by assuming that relaxation is greatest in the immediate vicinity of the defect and falls of fairly rapidly at distances away from the defect. Thus the approach (69) is to treat the crystal as being composed of two regions (figure 2.1); an inner region, region I, which surrounds the defect where the ions are relaxed explicitly and an outer region where the effect of the defect is estimated by a continuum approximation. The defect energy is then the difference in the lattice energy with and without the defect.

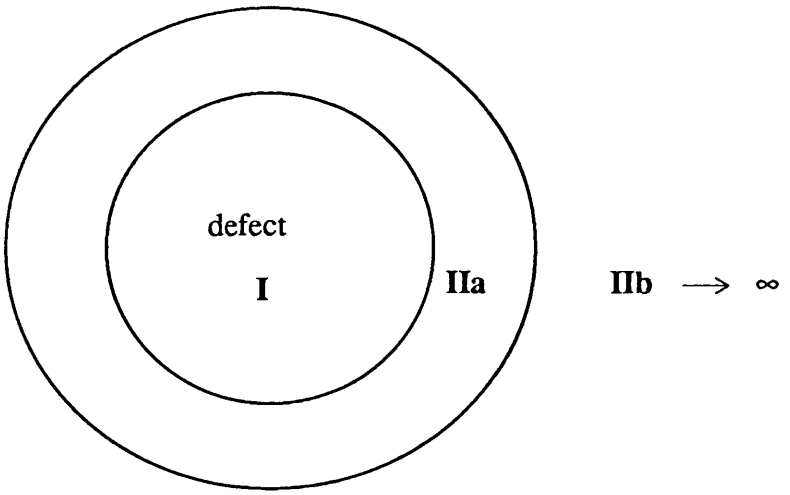

(a) Bulk calculations

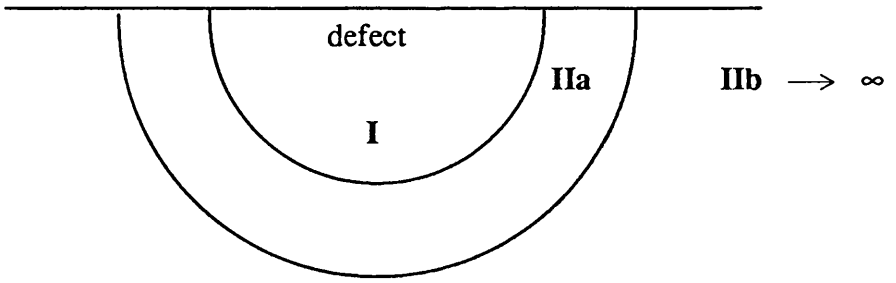

(b) Surface calculations

Figure 2.1: 'Two-region' strategy used for defect calculations. Region I is the explicitly relaxed region including and surrounding the defect. Region IIa is constructed for charged defects. Region IIb extends to infinity

The total energy of the system is written as the sum of three terms:

$$U(\underline{x},\underline{y}) = U_I(\underline{x}) + U_{I,II}(\underline{x},\underline{y}) + U_{II}(\underline{y}) \qquad (2.28)$$

where $U_I(\underline{x})$ is the energy of the inner region, $U_{I,II}(\underline{x},\underline{y})$ is the interaction between the two regions and $U_{II}(\underline{y})$ is the energy of the outer region. $\underline{x}$ represents the coordinates of ions in region I and $\underline{y}$ refers to the displacements in region II. The energy of the outer region, $U_{II}(\underline{y})$, cannot be solved exactly because it contains an infinite number of displacements. This problem can be overcome by writing this term as a quadratic function of the displacements in region II:

$$U_{II}(\underline{y}) = 1/2\underline{y}^T.\underline{\underline{A}}.\underline{y} \qquad (2.29)$$

and also by assuming that the ions in region II are at their equilibrium positions. The latter is ensured by using the structure of the perfect lattice which has been minimised by the method described in section 2.3 and then increasing the size of region I until the defect energy has converged. On substituting for $U_{II}(\underline{y})$ into equation 2.28 and applying the equilibrium condition; $\underline{y} = \bar{\underline{y}}$ for equilibrium values of $\underline{y}$ i.e. the net forces acting on the ions in region II are zero, then:

$$\partial U/\partial \underline{y}|_{y=\bar{y}} = \underline{A}.\underline{y} + \partial U_{I,II}(\underline{x},\underline{y})/\partial \underline{y}|_{y=\bar{y}} = 0 \qquad (2.30)$$

Equation 2.28 then becomes:

$$U = U_I(\underline{x}) + U_{I,II}(\underline{x},\underline{y}) - 1/2\partial U_{I,II}(\underline{x},\underline{y})/\partial \underline{y}|_{y=\bar{y}}.\underline{y} \qquad (2.31)$$

and, therefore, the equilibrium configuration of the defective lattice can found by minimising the net force acting on the ions in region I.

In the approach outlined above, the energy of the defect is calculated without the need to determine $U_{II}(\underline{y})$ explicitly. The interaction between region I and region II is evaluated by dividing region II into two regions; region IIA which surrounds region I and region IIB which extends to infinity. The short range interactions between ions in region I and region IIA are calculated explicitly, whereas the interaction between region I and IIB is described by a continuum approximation developed from classical polarisation theory by Mott and Littleton (80). In this approach the displacements in region IIB arise solely from the electric field produced by the total charge of the defect based at the origin. The polarisation $\underline{P}$ depends on the static dielectric constant of the material and at a distance $\underline{r}$ is given by:

$$\underline{P} = 1/4\pi\ (1 - 1/\epsilon_o)\ Ze\underline{r}/r^3 \qquad (2.32)$$

which leads to an r^{-4} interaction term in the energy.

The theory outlined above is adopted in the CASCADE (Cray Automatic System for the Calculation of Defect Energies) code (81) which a derivative of the HADES (Harwell Automatic Defect Evaluation System) code (69).

2.5 Calculation of the Energies of Extended Planar Defects

In this section, the calculation of the lattice energy of extended planar defects is described. This approach is embodied in the MIDAS program developed by Tasker (82). The crystal is described as a stack of charged planes which are periodic in two dimensions. The stack is divided into two regions (figure 2.2); region I which is adjacent to the surface and region II which represents the bulk of the crystal.

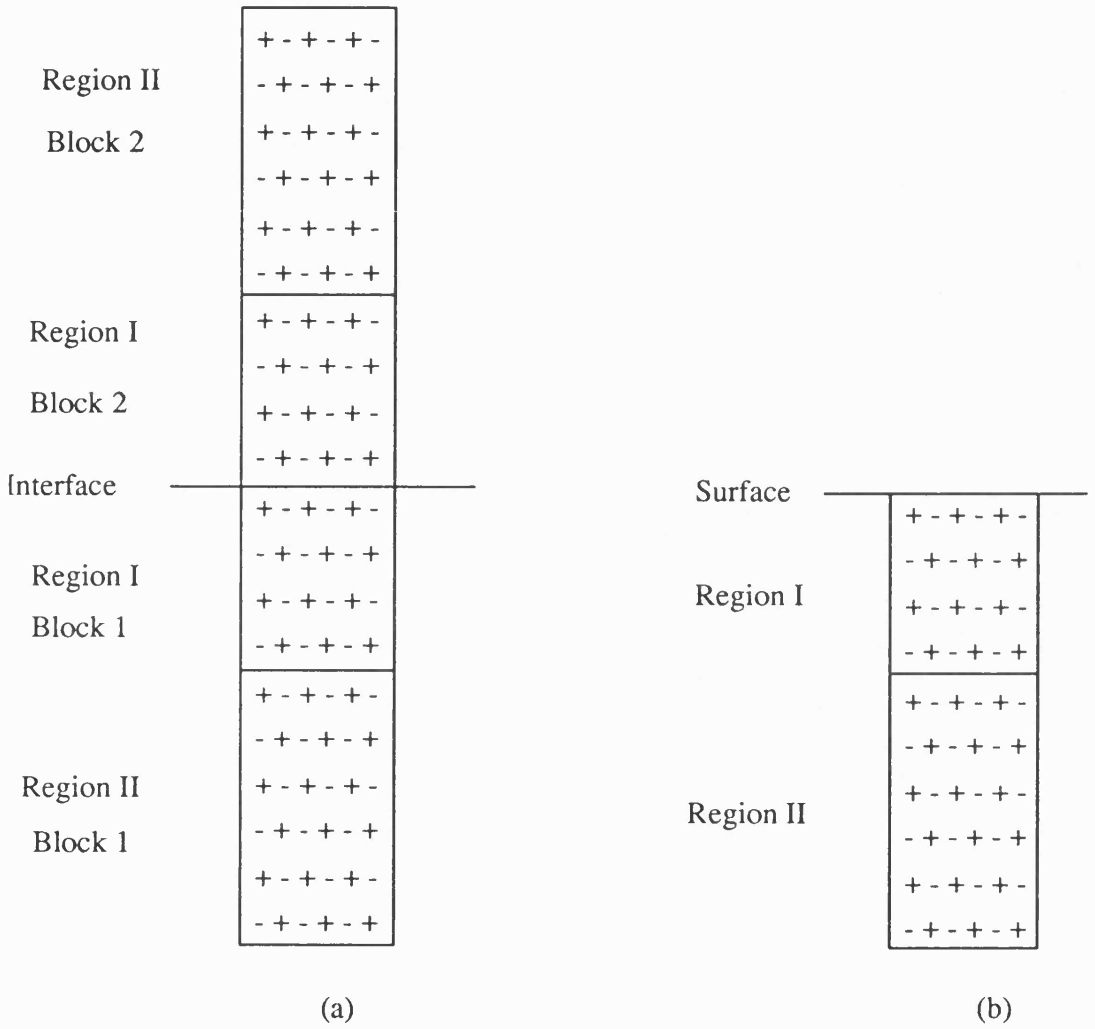

Figure 2.2: Schematic representation of the crystal regions for

a) a block calculation b) a surface calculation

In region I the ions are allowed to relax to mechanical equilibrium while the ions in region II are held fixed relative to each other, although the region as a whole may move. Thus, energies at constant area are calculated. Free surfaces and grain boundaries can be investigated using this approach. Defects and impurities can also be considered provided that the net charge on the crystal is zero (83).

The surface energy U^s per unit area is defined as:

$$U^s = \Sigma_{\lambda=1}^{m} [U(\lambda) - U(m)]/A \qquad (2.33)$$

where

$$U(\lambda) = 1/2\ \Sigma^{N} \Sigma_{j\neq 1} \phi(r_{ij}) \qquad (2.34)$$

and i is summed over all the ions in plane λ, m is a bulk plane, A the unit cell area and N the number of ions in region I. $\phi(r_{ij})$ is the potential between ions i and j.

The method by which the Coulomb energy is calculated is described by Parry (72,73) although a better description of it is given by Heyes et al. (84) and contains the $\underline{G}$=0 term ($\underline{G}$ is the reciprocal lattice vector in section 2.2) erroneously omitted in Parry's original derivation (72). This method is analogous to that given in section 2.2 except that the two dimensional periodicity of the lattice is exploited. The expression corresponding to equation 2.1 is

$$U(\underline{r}) = 1/2\ \Sigma_i^{N(I)} q_i \Sigma_j^{N(II)} q_j (|\underline{r}_{ij} + \underline{l}_1 a_1 + \underline{l}_2 a_2|)^{-1} \qquad (2.35)$$

where the sum is taken over the number of ions in region I, N(I) and region II, N(II). q_i, q_j, i, j, $\underline{r}_i$, $\underline{r}_j$ and a_n have the same definition as before but $\underline{l}_n$ is now a two dimensional lattice vector. As before, $U(\underline{r})$ is determined by dividing the identity

given in equation 2.2 into two parts; a real space contribution and a reciprocal space contribution. The real space contribution is evaluated from equation 2.7 without the inclusion of the self interaction term. The summation of the reciprocal space term is different however and must include the contribution to U(r) when G=0. In the Ewald summation this term vanishes because of the charge neutrality condition of the unit cell. At surfaces the calculations are performed by summing the Coulomb contribution of each plane in the crystal stack. Thus, if all the planes are charge neutral, the G=0 also vanishes e.g. unrelaxed MgO {100}. However, on relaxation the planes in the stack rumple and induce a dipole perpendicular to the surface. This leads to a finite value of the G=0 term. For charged planes this term is also non-zero. Consequently, it must be implicitly included in all surface relaxations. The reciprocal lattice contribution to the Coulomb energy thus becomes:

$$I_2 = \pi/A\ [\ -2\underline{u}_{ij}\mathrm{erf}(\eta\underline{u}_j) - 2\exp(-\eta\underline{u}_{ij})/\eta\pi^{1/2}]$$

$$+\ \pi/A\ \Sigma_{G\neq 0}\ (1/\underline{G})(B + C)\exp(i\underline{G}.\underline{p}_{ij}) \qquad (2.36)$$

where A is the area of the unit cell and

$$B = \exp(\underline{G}.\underline{u}_{ij})\ \mathrm{erfc}(\underline{G}/2\eta + \eta\underline{u}_{ij}) \qquad (2.37)$$

$$C = \exp(-\underline{G}.\underline{u}_{ij})\ \mathrm{erfc}(\underline{G}/2\eta - \eta\underline{u}_{ij}) \qquad (2.38)$$

In equation 2.36 $\underline{r}_{ij}$ has been resolved into two components $\underline{u}_{ij}$ perpendicular to the surface and $\underline{p}_{ij}$ in the plane:

$$\underline{r}_{ij} = \underline{u}_{ij} + \underline{p}_{ij} \qquad (2.39)$$

$2\eta/\pi^{1/2}$ is subtracted from equation 2.36 to remove the self interaction term.

2.6 Calculation of Isolated Defect Energies Near Interfaces

In this section, the way in which the HADES program, outlined in section 2.4, has been modified to calculate point defect energies near interfaces is described. The resulting program, CHAOS (Computer simulation HAdes On Surfaces) (85), developed by Duffy and Tasker uses as a starting configuration the relaxed interface structure generated by MIDAS. The crystal is again divided into two regions (figure 2.1). Region I is composed of circular discs of ionic planes which decrease in radius as the distance from the defect increases. Region II, the rest of the crystal, is treated as a dielectric continuum in which the ionic displacements are calculated by the Mott-Littleton method. The defect energy is the difference in energy between the pure and defective lattice.

Although the two region strategy is retained in CHAOS, the approach developed to cope with the electrostatic component of the point defect energy is different from HADES because of the presence of the interface. The interface removes the periodicity in one direction of the reference crystal and, therefore, the Coulomb contribution to the energy must be calculated by the Parry Method. The treatment of the ionic displacements and the energy of region II must also be modified because the r^{-4} summation does not allow for any structural variation around the planar defect. In CHAOS this energy is calculated by a combination of a discrete sum of planar integrals around the interface, and a volume integral over the remainder of the crystal. The planar integrals take explicit account of the dilation at the crystal boundary and are carried out for all planes in region I and II of the MIDAS stack. The energy of region IIB is then given by:

$$E_{IIB} = -Q^2/2\ [E_{planar} + E_{volume}] \qquad (2.40)$$

with

$$E_{planar} = \Sigma_{p\epsilon I,IIa}\ \Sigma_k\ q_k K_k \int_{\tau}^{\infty} 2\pi r/(r^2 + r_p^2)\ dr \qquad (2.41)$$

and

$$E_{volume} = 1/2\ \Sigma_k\ q_k K_k \int_{RIIB}^{\infty} (1/r^4) 2\pi r^2 dr \qquad (2.42)$$

where r_p is the perpendicular distance from the origin and plane p and τ is $(RIIB^2 - r_p^2)^{1/2}$.

When point defect energies are calculated for free surfaces E_{volume} is reduced by a factor of 2 and the interaction of charged defects with image charge must be included. The image charge, q_i, at an interface between dielectrics with different dielectric constants ϵ_1 and ϵ_2 is given by (86):

$$q_i = q_{def}(\epsilon_1 - \epsilon_2)/(\epsilon_1 + \epsilon_2) \qquad (2.43)$$

where q_{def} is the net charge of the defect and $\epsilon_1 > \epsilon_2$. In this thesis, only dielectric discontinuities at free surfaces are considered and, therefore, ϵ_2 is equal to 1, the value for free space. The field due to the image charge must also be included when calculating the displacements of the ions in region IIA and the polarisation energy of region IIB. The image charge is situated half an interplanar spacing above the outermost plane of ions.

The image charge reduces the stability of isolated charged defects as they

approach the free surface from the interior of the crystal (87). When two oppositely charged defects are brought towards the free surface from the crystal interior as a bound pair, the charge on one of the defects will interact with the image charge of the other and vica versa. Hence, the repulsion exerted by the dielectric discontinuity on the bound pair is reduced and its binding energy and stability are increased.

2.7 The Calculation of the Vibrational Free Energy

In the calculations described in the previous sections, no account was taken of the vibrational properties of the solid. Thus the calculated energies correspond to potential energies of the pure or defective lattice at 0 K. The vibrational component to the free energy can be determined by either molecular dynamics (88) or lattice dynamics (76). The way in which the two approaches differ is that with molecular dynamics the ions are simulated to move according to Newtons Laws of Motion whereas in lattice dynamics the ionic vibrations are calculated by the method of Born and Huang (76). The advantage of the former method is that the full anharmonicity of the potential energy surface is investigated. This is because the atoms move and, thus, sample different parts of configurational space. In contrast, the atoms in lattice dynamics only sample the energy at specific lattice sites where the shape of the potential energy well is assumed to be harmonic. The disadvantage of molecular dynamics is that it is very computer time intensive (89,90) which precludes an adequate description of electronic polarisation. As the structures and stabilities of surfaces depend on the electronic polarisability (91), surface calculations were only performed using lattice dynamics.

The free energy is calculated by determining the vibrational frequencies of a periodic lattice (57) which can be found from:

$$\underline{\underline{m}}\omega^2(\underline{q})\underline{e}(\underline{q}) = \underline{\underline{D}}(\underline{q})\underline{e}(\underline{q}) \qquad (2.44)$$

which is an eigenvalue problem. In this equation $\underline{\underline{m}}$ is the diagonal matrix of ionic masses, $\underline{q}$ is the reciprocal-lattice vector of lattice vibrations, $\underline{e}(\underline{q})$ is the polarisation vector describing the atomic displacement in the vibration, and $\underline{\underline{D}}(\underline{q})$ is the dynamical matrix given by:

$$\underline{\underline{D}}(\underline{q}) = \Sigma_{ij}(\partial^2 U/\partial \underline{r}_i \partial \underline{r}_j)\exp(i\underline{q}.\underline{R}) \qquad (2.45)$$

where $\underline{R}$ is the interionic separation, and $\underline{r}_i$ and $\underline{r}_j$ are the atomic displacements from equilibrium positions of ions i and j. Note the dependence of $\underline{\underline{D}}(\underline{q})$ on the second derivative of the lattice energy. For a unit cell containing n atoms, there are 3n solutions for a given value of $\underline{q}$. The polarisation vectors are the eigen vectors of equation 2.44 while the square root of the eigenvalues give the vibrational frequencies. The vibrational contribution to the Helmholtz free energy is then given by:

$$F = kT\,\Sigma_q[\,h\omega/2kT + \ln(1 - \exp(-h\omega/2kT)] \qquad (2.46)$$

where k is Boltzmanns constant, h is Plancks constant and equation 2.46 is summed over all wave vectors $\underline{q}$ in the Brillouin zone. In practice, it is impractical to calculate the frequencies for all wave vectors and, therefore, some selective sampling method must be used. Ideally this method would predict the free energy accurately but sample as few points as possible. A variety of approaches for choosing sampling points have been suggested (92,93,94) but only those derived by the Fillippini method (94), which compares favourably with the other methods (95), were used in this thesis. In this method the points are chosen to lie on a general grid in 2 or 3 dimensions with

appropriate weighting factors. The weighting factors depend on the number of times a point appears in the Brillouin zone and the area it represents. They are given in tables 2.1 and 2.2 along with their respective sampling points for bulk and surface calculations.

Equation 2.46 gives the Helmholtz free energy at a given lattice volume. In the harmonic approximation the volume is taken to be that of the 0 K structure and, therefore, as the temperature is increased lattice expansion is neglected. In the quasi-harmonic approximation, the vibrational frequencies are assumed to vary with volume. The kinetic pressure is then minimised to calculate the volume of the unit cell at the required temperature. The kinetic pressure is the derivative of the Helmholtz free energy with volume and for a cubic material can be found by rewriting the free energy as (96):

$$F = kT \Sigma_q[h\omega/2kT + \ln(1 - \exp(-h\omega/2kT)] + (\Delta V)^2/2\kappa V \qquad (2.47)$$

where κ is the compressibility. The first term comes from equation 2.46 and the second term represents the increase in the elastic energy due to lattice expansion. Putting $(\partial F/\partial V)_T$ as zero, the volume is found from:

$$\Delta V/V = -\kappa kT \Sigma_q 1/\omega ((q))(\partial\omega (q)/\partial V) \qquad (2.48)$$

Once the kinetic pressure is evaluated, the constant pressure minimisation technique (section 2.3.2) can be employed for predicting the thermally equilibrated structure. In this case the total pressure becomes the sum of the kinetic, mechanical and applied hydrostatic pressure.

Table 2.1: Reciprocal lattice points used for 3D calculations

Number of Points	x	y	z	weighting
1	0.25000	0.25000	0.25000	1.0
8	0.08333	0.08333	0.08333	1.0
	0.08333	0.08333	0.03333	2.0
	0.08333	0.33333	0.08333	2.0
	0.08333	0.33333	0.33333	4.0
	0.33333	0.08333	0.08333	2.0
	0.33333	0.08333	0.33333	4.0
	0.33333	0.33333	0.08333	4.0
	0.33333	0.33333	0.33333	8.0

Table 2.2: Reciprocal lattice points used for 2D calculations

Number of Points	x	y	z	weighting
1	0.00000	0.25000	0.25000	1.0
4	0.00000	0.06250	0.06250	0.015625
	0.00000	0.06250	0.31250	0.046875
	0.00000	0.31250	0.06250	0.046875
	0.00000	0.31250	0.31250	0.140625

The disadvantage of the quasi-harmonic and the harmonic approaches is that the expansion of the lattice potential energy with respect to atomic position is truncated to second order (the harmonic term). The importance of higher order or anharmonic terms can thus be investigated by comparing the calculated and observed lattice expansion coefficients, β:

$$\beta = 1/V \, dV/dT \qquad (2.49)$$

The theoretical method outlined above is the basis of the PARAPOCS code and is described in greater detail by Parker and Price (97).

The reliability of the calculations outlined above depend critically on the potential models that are used to describe the interionic forces in the crystal. Therefore, the focus of the following chapter is the derivation of reliable potential models.

Chapter 3

Potential Models

3.1. Introduction

The introduction of sophisticated quantum simulations such as the Car Parrinello approach (98) has enabled researchers to calculate defect energies in metals (99) and the structures of semiconductor interfaces (100,101) without defining a potential model. The treatment of oxides by these methods is still in its infancy (102) because the required computational power is currently not available. Consequently, a more traditional technique was used to study the surface properties of oxides. This is atomistic simulation, in which the Born model of solids is used to describe the interactions between ions. Two methods can be used to derive the potential models that are necessary for the Born model. These are a non-empirical method, where the potentials are determined by numerical methods, and an empirical method, where the potentials are determined by fitting to experiment. Both types of potential were used in this thesis. Therefore, the methods by which they were derived is described, and their applicability to surface calculations is discussed. First, the nature of the Born model is presented.

3.2 The Born Model of Solids

In the Born model of solids the lattice energy, $U(r_{ij})$, is given by:

$$U(r_{ij}) = \Sigma_{ij}{}' \, q_i q_j / r_{ij} + \Sigma_{ij}{}' \, \phi_{ij}(r_{ij}) \qquad (3.1)$$

where q_i and q_j represent the integral ionic charges associated with the ions i and j, r_{ij} is the distance between these ions and ϕ_{ij} is the short range interaction beween ions i and j.

The first term in equation 3.1 represents the electrostatic energy due to the interaction between charged ions. Although it converges slowly in real space, methods have been developed to sum it in rapidly in two (84) and three (68) dimensions. Both methods are used in this thesis and they were discussed in Chapter 2. The second term in equation 3.1 represents the short range interaction energies. These act between the centres of neighbouring ions, are highly repulsive at small r, and describe the overlap of the electron clouds. As the distance between ions i and j increases the interaction may include an attractive component arising from the effects of induction and covalency. A third term is sometimes incorporated into equation 3.1 which corresponds to a three body or 'bond bending' interaction and gives information on the directional nature of the bonding in crystals. It must be included in models of α-quartz (103) and other silicate minerals (55) to reproduce the correct elastic and dielectric data. However, three body terms were not found to be a necessary component of the potentials used in this work.

The two methods that were used to determine the short range potential are discussed in section 3.4. First, the inclusion of ionic polarisation in the model is discussed. This is particularly important when considering the dielectric response of the lattice to charged defects.

3.3 Ionic Polarisability

In rigid ion models, ion polarisability is neglected completely i.e. the high frequency dielectric constant of the material is unity. This type of potential must be used in molecular dynamical studies (104) because computer resources preclude the

explicit inclusion of electronic polarisability. Rigid ion models can also be used in defect studies (105) if the short range parameters are chosen such that they correctly reproduce the static dielectric constants of the material. This is essential for modelling the response of the lattice to charged defects (106).

The neglect of ion polarisability limits the ability of the potential to reproduce the dynamical properties of the lattice because lattice vibrations are strongly influenced by ionic polarisation (107). It also restricts the treatment of defects at boundaries (108). As an adequate description of these is required for the work outlined here, an explicit representation of polarisability is required. The simplest model that does this is the point polarisable ion model which is now described.

3.3.1 Point Polarisable Ion (PPI) Model

In this model, the polarisability is fixed for an ion and is introduced via a dipole, $\underline{m}$, induced by an electric field $\underline{E}$ where $\underline{m}$ is given by:

$$\underline{m} = \alpha \underline{E} \qquad (3.2)$$

and α is the ion polarisability. Hence, the energy of the interacting dipoles can be calculated. This method has been employed in defect calculations but unfortunately it is found to be unsatisfactory because the calculated defect energies are substantially lower than the experimental ones (109). The problem lies with the inability of the model to allow the electronic charge distribution to distort as the ion environment changes i.e. the polarisability, α, does not change with a change in environment. This leads to an instability in the model which occurs when two dipoles increase without bound because their mutual dipole-dipole interaction outweighs the self-energy of polarisation. It is particularly acute for calculations that bring ions close together.

Faux (110) showed that there is a critical distance r_{crit} as the two ions approach each other after which the interaction energy becomes divergent:

$$r_{crit} = (4\alpha_i\alpha_j)^{1/6} \qquad (3.3)$$

This problem is overcome by the use of the shell model which is able to take account of the displacement of electrons when the ion is placed in a potential gradient i.e. the polarisability of the ion will change with a change in its environment.

3.3.2 The Shell Model

The shell model was originally proposed for use in defect calculations by Lidiard and Norgett (111) and is based on the model developed by Dick and Overhauser (112). It provides a simple mechanical description of coupling the core of nucleus, X, of an ion to the electronic charge cloud or shell of zero mass, Y, via a harmonic spring with force constant, k. The total ionic charge being the sum of X and Y. The interaction between the shell and core of an ion i is therefore:

$$\varphi_i(r_i) = k_i r_i^2 \qquad (3.4)$$

where the polarisability, α, of an ion is:

$$\alpha_i = Y_i^2/K_i \qquad (3.5)$$

and $K_i = k_i + r_i$ with $k_i >> r_i$. In principle the parameters Y and K can be calculated by quantum mechanical methods. However, in practice this approach has been found to be unsatisfactory and, therefore, the parameters are derived by fitting to dielectric and

elastic constants and phonon frequencies. A review of polarisability and its effect on defect calculations is given by Catlow and Mackrodt (113).

The shell parameters, derived from bulk properties, were used in the surface calculations described in Chapters 4, 5 and 6. Fowler and Tole (114) used an ab initio SCF method to calculate the electronic structures of O^{2-} and F^- ions at unrelaxed surfaces, steps and corners of MgO and LiF and compared them to bulk calculations. They found that the anion polarisabilities increase with decreasing coordination. The rate of increase was much greater for O^{2-} ions but was partially reduced by surface relaxation. Thus the present method for determining Shell parameters might introduce inadequacies into the calculations. However, Martin and Bilz (115) used a shell model that incorporated extra parameters to allow for such a variation between bulk and surface ions in MgO and concluded that surface topography was not influenced by this extra degree of freedom. Also, previous workers have found that the parameters do appear to be transferrable (116).

The short range forces forces are considered to act between the shells of ions. In this way the shell model allows for the distortion of the electron clouds by short range forces.

3.4 Derivation of Short Range Potential $\phi_{ij}(r)$

As noted above, two types of potential model were used in this work and they differ in the way in which the short range pairwise interactions (equation 3.2) were calculated. In the first method the two-body potentials are derived by fitting to observed bulk crystal properties. In the second approach these interactions are obtained by an approximate quantum mechanical or non-empirical method.

As the surface environment is different from the bulk the use of bulk potentials in surface calculations must be justified. Lawrence (117) calculated two

sets of short range potentials for Cr_2O_3 by non-empirical methods which reproduced the experimental bulk crystal properties. The difference in these potentials was that two Madelung well depths were chosen to calculate the electron densities of the O^{2-} ion. This reflected the difference in the potential well in the bulk and at the surface. Comparison of the relaxations of the {0001}, {11$\bar{2}$0}, {10$\bar{1}$0}, {10$\bar{1}$2} and {10$\bar{1}$1} surfaces showed that they were insensitive to the change in potential. Fowler and Tole (114), who calculated the bulk and surface polarisabilities of O^{2-} and F^- ions discussed in the previous section, also used their ab initio SCF method to investigate other properties. They found that at the surface the effective anion size and shape was little different from that of the bulk. The insensitivity to environment was attributed to the cancellation of two competing factors. The electron density has more freedom to move at the surface because it has fewer neighbours. This serves to reduce the Madelung well depth and so the stabilising potential well is shallower. This effect is counterbalanced by the increase in the electrostatic field at the ion site pulling the electrons back into the solid. A similar conclusion was reached by Causa et al. (118). The transferability of potentials is also demonstrated by the good agreement between experimental and calculated segregation energies (58). The two ways in which the short range potentials are derived are now described.

3.4.1 Empirical Derivation of Short Range Parameters

In this approach, the repulsive interaction is assumed to be related to the ionic separation by the equation:

$$\phi_{ij}(r) = A_{ij}\exp(-r_{ij}/\rho_{ij}) \qquad (3.7)$$

where the parameters A_{ij} and ρ_{ij} represent the relevant ion size and hardness (119).

Equation 3.6 is known as the Born-Mayer expression and was extended by Buckingham to take account of attractive van der Waals dispersive and covalent interactions:

$$\phi_{ij}(r) = A_{ij}\exp(-r_{ij}/\rho_{ij}) - C_{ij}/r_{ij}^{6} \qquad (3.7)$$

The parameters A_{ij}, ρ_{ij} and C_{ij} are determined by least squares fitting to the known experimental crystal properties e.g. structural dielectric properties, cohesive energy, elastic constants, and phonon frequencies (120). Although this description of the short range interactions has been used successfully for a wide range of materials (121,122), there are two points that must be noted. The first is that it is often not possible to determine all the parameters A_{ij}, ρ_{ij} and C_{ij} uniquely for each pair of ions because there is insufficient experimental data. Thus, to reduce the number of variables cation-cation interactions were neglected. This interaction is small, particularly at the distances that are of interest in solids and thus the approximation would seem to be adequate. The second point to note is that for properties calculated at interatomic distances far removed from the equilibrium lattice positions, the agreement with the non-empirical model outlined in the next section is not entirely satisfactory. This is particularly true for oxygen interstitials (117). In general though the comparison between these two methods is favourable.

The empirical potential was used in the work described in Chapter 4 to model alkaline earth impurity segregation in α-Al_2O_3. The parameters used are given in table 3.1 and were derived by Lewis and Catlow for CaO, MgO and α-Al_2O_3 (120).

Table 3.1: Empirical Potential Parameters used in Chapter 4

	A(eV)	ρ(Å)	C(eV.Å^{-6})
Aluminium-Oxygen	1474.4	0.3006	0.0
Calcium-oxygen	1090.4	0.3437	0.00
Magnesium-oxygen	1428.5	0.2945	0.0
Oxygen-oxygen	22764.3	0.149	27.88
Aluminium ion: Al^{3+}	Y_+ (|e|)	1.458	
	K_+ (eVÅ^{-2})	1732.0	
Calcium ion: Ca^{2+}	Y_+ (|e|)	3.135	
	K_+ (eVÅ^{-2})	110.2	
Magnesium ion: Mg^{2+}	Y_+ (|e|)	1.585	
	K_+ (eVÅ^{-2})	361.6	
Oxygen ion: O^{2-}	Y_- (|e|)	-3.0	
	K_- (eVÅ^{-2})	60.78	

3.4.2 Non-empirical or Electron Gas Methods

The non-empirical or electron gas method can be used to calculate the repulsive interactions between ions at different separations. It has three main advantages over the empirical method. The first advantage is that interaction energies can be determined for ion separations which are significantly different from those in the bulk. The second advantage is that potentials can be determined for crystals where there is little experimental data available. The third advantage of this approach, which is utilised in this thesis, is that interaction energies can be calculated for ions in different valence states consistently.

The electron gas method (123,124,125) is based on density functional theory which assumes (126) that the total energy of the system in the ground state is a unique function of the density distribution of the electrons (ρ). The total energy of the system is written as:

$$E(\rho) = E_{COUL} + E_T(\rho) + E_{EX}(\rho) + E_{CORR}(\rho) \qquad (3.8)$$

where E_{COUL} arises from all the coulombic interactions involving nuclear charges and electron clouds, E_T is the kinetic energy, E_{EX} is the exchange energy due to exchange symmetry of the electrons and E_{CORR} is the correlation energy.

The electron density (ρ_{AB}) of the interacting system, AB is found from the Hartree-Fock electron densities, ρ_A and ρ_B, of the isolated closed shell species A and B. The electron densities are assumed to be additive:

$$\rho_{AB}(r) = \rho_A(r) + \rho_B(r) \qquad (3.9)$$

This approximation is appropriate for closed shell species such as inert gas

atoms or ions in solids. For more covalent interactions of open shell atoms there will be substantial rearrangement of the electron density and, therefore, this assumption is inadequate.

Thus, the interaction energy (E_{INT}) is equal to:

$$E_{INT} = E(\rho_{AB}) - E(\rho_A) - E(\rho_B) \qquad (3.10)$$

The first term in equation 3.8 is the Coulomb interaction between all the charges (electrons and nuclei) and its contribution to the interaction energy is calculated by a method outlined by Kim and Gordon (125). Approximations to the three remaining terms in equation 3.8 must be made so that they may be evaluated from the Hartree-Fock electron density. This is achieved by using functionals which are derived from a uniform electron gas (127,128). Although this is not a good approximation near the nucleus (129), the contributions from these nuclear regions to the total energy of the interacting system are essentially the same as the sum of the corresponding contributions in the separate ions, so that the effects of the nuclear regions will cancel from the interaction energy. The functional forms of the kinetic, E_T, and exchange, E_{EX}, energies are approximated by:

$$E_T(\rho) = c_T \int \rho(r)^{5/3}\, dr \qquad (3.11)$$

$$\text{with } c_T = (3/10)(3\pi^2)^{2/3} \qquad (3.12)$$

and

$$E_{EX} = c_{EX} \int \rho(r)^{4/3}\, dr \qquad (3.13)$$

with $c_{EX} = -3/4(3/\pi)^{1/3}$ (3.14)

Equation 3.13, the Slater-Dirac (130,131) exchange energy, does not depend on the total number of electrons in the system (N) and so does not tend to zero for $N \leq 2$ as it should. This leads to spurious long range minima in the interaction energy (125). This can be corrected (132) by using a correction factor of the form:

where $\gamma(N) = (3 - 8\delta + 6\delta^2 - \delta^4)/3$ (3.15)

and δ is related to the total number of electrons by:

$$N^{-1} = 1/2(8\delta^3 - 9\delta^4 + 2) \quad (3.16)$$

Equation 3.13 becomes:

$$E_{EX} = -k \int \gamma(N_A)\rho_A((\rho_A + \rho_B)^{1/3} - \rho_A{}^{1/3})dr$$

$$-k \int \gamma(N_B)\rho_B((\rho_A + \rho_B)^{1/3} - \rho_B{}^{1/3})dr \quad (3.17)$$

The difference between the Hartree-Fock and the exact non-relativistic energy is the correlation energy. This is best calculated by (133) splitting the energy into two components: a long range (E_{CORRL}) and a short range (E_{CORRS}) contribution. The short range contribution is adequately described by the electron gas model. It is given by:

$$E_{CORRS} = \int \epsilon_{CORR}\, \rho(r)\, dr \quad (3.18)$$

where ϵ_{CORR} is an interpolation between high and low electron density limits and is given in full by Allan, Cooper and Mackrodt (134).

In the calculation of the long range part of the correlation or dispersive energy, the electron gas approximation cannot be used (133). The origin of this interaction can be thought of as arising from coupling between instantaneous electric multipole moments in the participating atoms. The interaction can be calculated in perturbation theory and expressed as a multipole expansion:

$$E_{CORRL} = - \Sigma_{n\geq 3} C_{3n} R^{-2n} \qquad (3.19)$$

This expression involves excitations in both atoms, although it may be divergent for any finite R because of overlap effects. Thus the best estimate of this asymptotically divergent series is obtained by truncating it at the smallest term. A further modification, suggested by Rae (135), is to rewrite the series as:

$$E_{CORRL} = - \Sigma_{n\geq 3} C_{2n} g_n(R) R^{-2n} \qquad (3.20)$$

where

$$g_n(R) = (1 + \exp(-2(2R-R_n+R_{n+1})/2(R_{n+1}-R_n)^{-1} \qquad (3.21)$$

and

$$R_n = (C_{2n}/C_{2n-2})^{1/2} \qquad (3.22)$$

As noted above, Hartree-Fock electron densities are required to calculate the

energy of the system. Before doing this, some account of the Madelung field surrounding the ions in the crystal must be included. This is particularly important for the determination of the electronic structure of the O^{2-} ion: in the free state it is unbound, but in an ionic crystal such as MgO the 2p level is bound by about 10 eV (136). Thus the Hartree-Fock equations are solved in an external spherical potential which is chosen to reproduce the Madelung potential at the relevant ion site. The form of the potential well is (136):

$$V(r) = -V_O \qquad r \leq r_x$$

$$V(r) = -V_O r_x/r \qquad r \geq r_x \qquad (3.23)$$

where V_O is the well depth and r_x is the ionic radius of the anion. For the cations, the "free-ion" electron densities are used because the "free-ion" radial distribution functions do not change appreciably in the solid state.

The non-empirical potentials that were used were calculated by Mackrodt at ICI (137) using the relationships outlined above and are given in Appendices 1, 2 and 3. In Chapter 4 these potentials (Appendix 1) are compared with those derived empirically. In Chapter 5 potentials derived for the binary oxides La_2O_3, Nd_2O_3 and CuO were used to model the surface properties of La_2CuO_4 and Nd_2CuO_4. The suitability of this approach for modelling ternary oxides has been demonstrated by numerous workers (138,139). Allan et al. (140) used these potentials to determine the most favourable structural forms of these oxides and found good agreement with experiment, even though no account of the Jahn-Teller effect is included in the model. Details of these potentials are given in Appendix 2. In chapter 6, the surface defect properties of these ternary oxides are discussed. A further set of potentials were

required for CeO_2, ThO_2, MgO, CaO, SrO and BaO and these are given in Appendix 3. The short range potentials used in these surface calculations were those that correctly predicted the bulk structure, except that a further k' term was added to the cation spring potentials. This was necessary because some relaxed core shell separations were physically unreasonable. Equation 3.4 thus becomes

$$\varphi_i(r_i) = k_i r_i^2 + k'_i r^4 \qquad (3.24)$$

The advantage of this potential form is that the properties calculated using this extra term, such as the structure, high frequency and static dielectric constants remain unchanged but it prevents the large electric fields from separating the core and shell. Hence, the response of the lattice to charged defects is comparable to the original potential.

3.5 Summary

In this chapter, the potential models used in this thesis and the methods by which they were derived have been described. Only pairwise interactions were used due to the previous success of the potentials. In chapter 4, both empirical and non-empirical potentials are used but in subsequent chapters, those obtained by the electron gas method only are employed.

Chapter 4

Alkaline Earth Impurity Segregation In α-Al_2O_3

4.1 Introduction

In this chapter, an investigation of the segregation of calcium at the basal and calcium and magnesium at the $\{10\bar{1}0\}$ prism surfaces of α-Al_2O_3 is described. This is an important question in ceramic processing because small additions of magnesium oxide to α-Al_2O_3 (141) prevent exaggerated grain growth during sintering and, therefore, promote densification. Exaggerated growth occurs when grain boundary mobility is much greater than pore mobility and this reduces the strength and toughness of the sintered ceramic. However, the role played by magnesium is still unclear: it may either segregate to grain boundaries and decrease mobility by a solute-drag mechanism (142) or, alternatively, segregate to pore surfaces and influence surface diffusivity and pore mobility (143). These theories are further complicated by calcium, which has also been observed at grain boundaries (144) and free surfaces (145), but does not prevent exaggerated grain growth (146).

The calculated segregation energies are then used to evaluate the variation of impurity surface coverage with temperature. The inherent assumption in this approach is that the calculated energies, which strictly speaking are potential energies, are valid at high temperatures. Thus the variation of thermodynamic properties with temperature is investigated.

4.2 The Calculation of Segregation Isotherms

The current method that is used for comparing calculated segregation energies

with experiment is described in this section. The experimental techniques used for surface analysis measure the surface impurity concentrations that are assumed to be equilibrated with the bulk as a function of temperature. Heats or enthalpies of segregation are then extracted from conventional plots of the log of the surface concentration against reciprocal temperature. These are often linear and it is commonly assumed that this is indicative of Arrhenius or Langmuir behaviour, wherein the surface atomic ratio of the impurity, x_s, is related to the bulk ratio, x_b, by an expression of the form:

$$x_s \alpha x_b \exp(-\Delta h/kT) \qquad (4.1)$$

in which Δh is a coverage independent heat of segregation, T the temperature and k is Boltzmann's constant. This expression is likely to hold for low coverages, but as the surface defect concentrations increase defect-defect interactions will play a more important role in determining the segregation energies and thus Langmuir behaviour will be the exception rather than the rule. This has been confirmed recently by atomistic simulations on iso- (147) and aliovalent (148) impurity segregation in α-Al_2O_3. Consequently, a statistical mechanical model, as derived by Mackrodt and Tasker (58), is now presented which is similar to equation 4.1, but allows for a variation of Δh with coverage. In this way the calculated segregation energies can be compared with the experimentally observed surface coverages.

Assume that there are only two types of site: a surface and a bulk site. The total free energy (G) of the system is given by:

$$G = n_1^b g_1^b + n_1^s g_1^s + n_2^b g_2^b + n_2^s g_2^s$$

$$- k\ln\Omega \qquad (4.2)$$

where n_i^b and n_i^s are the numbers of bulk and surface ions of type i with individual free energies g_i^b and g_i^s respectively. Assuming a random distribution of ions, the configurational entropy, $k\ln\Omega$, is:

$$k\ln\Omega = k\ln\{(N^b!/n_1^b!n_2^b!)(N^s!/n_1^s!n_2^s!)\} \quad (4.3)$$

where N^b and N^s are the total bulk and surface sites respectively. The conservation equations that constrain the system are:

$$n_1^b + n_1^s = n_1 \quad (4.4)$$

$$n_2^b + n_2^s = n_2 \quad (4.5)$$

$$n_1^b + n_2^b = N^b \quad (4.6)$$

$$n_1^s + n_2^s = N^s \quad (4.7)$$

and by defining the ions of type 1 to represent the impurity, the following equations also apply:

$$n_1 << n_2 \quad (4.8)$$

$$N^s << N^b \quad (4.9)$$

$$n_2^b \sim N^b \quad (4.10)$$

G can now be written as:

$$G = G_1 + G_2 \tag{4.11}$$

with

$$G_1 = n_1^s(g_1^s + g_2^s - g_1^b + g_2^b) + n_1 g_1^b +$$

$$N^s g_2^s + (n_2 - N^s) g_2^b \tag{4.12}$$

and

$$G_2 = -kT\ln\Omega \tag{4.13}$$

The minimum free energy of the system is found by varying the number of impurities at the surface. If it is initially assumed that g_i^s is independent of n_1^s then:

$$dG_1/dn_1^s = g_1^s - g_2^s - g_1^b + g_2^b \tag{4.14}$$

and

$$dG_2/dn_1^s = kT\ln\{(n_1^s/n_2^s)/(n_1^b/n_2^b)\} \tag{4.15}$$

By writing:

$$n_1^s/n_2^s = x_s \tag{4.16}$$

$$n_1^b/n_2^b = x_b \tag{4.17}$$

$$g_1^s - g_2^s = \delta g^s \tag{4.18}$$

$$g_1^b + g_2^b = \delta g^b \tag{4.19}$$

$$\delta g^s - \delta g^b = \Delta g \tag{4.20}$$

the Arrhenius or Langmuir expression, analogous to equation 4.1, is obtained:

$$x_s = x_b \exp(-\Delta g/kT) \tag{4.21}$$

where δg^s, δg^b and Δg correspond to the bulk and surface substitution free energies and segregation free energy respectively. Note at this point that the vibrational entropy is included in the free energy in addition to the configurational entropy.

Impurity-impurity interactions are included by requiring Δg to be function of surface impurity coverage. Equation 4.14 thus becomes:

$$dG_1/dn_1^s = \Delta g + n_1^s(d\Delta g/dn_1^s) \tag{4.22}$$

and the modified expression for x_s is then:

$$x_s = x_b \exp\{-\Delta g + x_s(x_s + 1)(d\Delta g/dx_s)/kT\} \tag{4.23}$$

By writing Δg in terms of Δh the heat of segregation and Δs the vibrational entropy of segregation:

$$\Delta g = \Delta h - T\Delta s. \qquad (4.24)$$

equation 4.23 can be written as:

$$x_s = x_b \exp\{-\Delta s + x_s(x_s + 1)(d\Delta s/dx_s)/k\}.$$
$$\exp\{-\Delta h + x_s(x_s + 1)(d\Delta h/dx_s)/kT\} \qquad (4.25)$$

from which the slope of $\ln(x_s)$ against 1/T is clearly not that of the Arrhenius expression of equation 4.1. At this point it is noted that x_s corresponds to the surface ratio of impurity to host cations and this is the definition used in AES experiments. However, this is an inconvenient definition because monolayer coverage is undefined. This problem is overcome by writing equation 4.23 as:

$$n_1^s/n_2^s = n_1^b/n_2^b \exp\{(\Delta g + n_1^s d\Delta g/dn_1^s)/kT\} \qquad (4.26)$$

and defining a surface and a bulk concentration C_s and C_b respectively such that:

$$C_s = n_1^s/(n^s_1 + n_2^s) \qquad (4.27)$$

$$C_b = n_1^b/(n_1^b + n_2^b) = n_1^b/n_2^b \qquad (4.28)$$

On substituting 4.27 and 4.28 into 4.26 the surface impurity concentration is given by:

$$C_s = C_b[\exp\{(\Delta g + C_s d\Delta g/dC_s)/kT\}].$$
$$[1 + C_b \exp\{(\Delta g + C_s d\Delta g/dC_s)/kT\}]^{-1} \qquad (4.29)$$

and monolayer coverage corresponds to C_s=1. Equation 4.29 compares with the one

proposed by McLean (149), except that here Δg is not independent of surface coverage. As above, the surface coverage can be written in terms of the enthalpy and entropy of segregation:

$$C_s = C_b[\exp(-\Gamma/kT)].[1 + C_b\exp\{(-\Gamma/kT)]^{-1} \qquad (4.30)$$

where

$$\Gamma = (\Delta h + C_s d\Delta h/dC_s) - T(\Delta s + C_s d\Delta s/dC_s) \qquad (4.31)$$

Again this form of isotherm does not necessarily exhibit Langmuir behaviour. Experimental plots of log surface concentration against reciprocal temperature are, however, often linear. This can be interpreted by writing equation 4.30 as:

$$\ln (C_s) = \ln (C_b) + (\Delta s + C_s d\Delta s/dC_s)/k - (\Delta h + C_s d\Delta h/dC_s)/kT \qquad (4.32)$$

$$= \chi - H/kT \qquad (4.33)$$

and solving for H such that:

$$\Delta h(C_s) + C_s d\Delta h(C_s)/dC_s = H \qquad (4.34)$$

The trivial solution is where Δh is independent of C_s. H is also independent of the surface concentration when $\Delta h \propto -C_s^{-1}$.

The important result is that there are two possible definitions of segregation. The first can be viewed as an atomistic description embodied in equation 4.20 and the

second, H, which is extracted from plots of surface coverage versus reciprocal temperature. Neither of these definitions require the segregation enthalpy to be independent of coverage and so do not necessarily exhibit Langmuir behaviour. This approach is applied to magnesium and calcium segregation in α-Al_2O_3 after a discussion on the pure bulk and surface properties.

4.3 Bulk and Surface Structures of α-Al_2O_3

α-Al_2O_3, more commonly known as corundum, has a structure which is based on hexagonally close packed layers of oxygen with aluminium ions filling 2/3 of the available octahedral sites (see figure 4.1). Thus the oxygen ions are coordinated to four aluminiums. This structure has the $R\bar{3}c$ point group which does not possess full hexagonal symmetry because the cation and anion sublattices are distorted along the c-direction. This is a consequence of the partial filling of available cation sites.

The corundum structure leads to a potentially large number of low-index and potentially low energy surfaces. In this work, the relative stabilities of the five lowest index surfaces were considered in order to compare the two potential models that were used. The five surfaces are the basal surface and four other surfaces. At right angles to the basal surface are the surfaces related to the hexagonal prism. The prism face is indexed $\{10\bar{1}0\}$ and the diagonal prism is indexed $\{11\bar{2}0\}$. The primitive unit cell is rhombohedral and faces related to this should have the smallest two dimensional unit cells. The rhombohedral faces considered are the $\{10\bar{1}1\}$ and $\{10\bar{1}2\}$.

Figure 4.2 shows the stacking sequences of the pure surfaces investigated. The basal surface (figure 4.2(a)) is the only surface which terminates in cations. The structure, therefore, consists of planes of anions interleaved by puckered planes of cations. The surface layer of oxygen ions has aluminium ions above it in one-third of

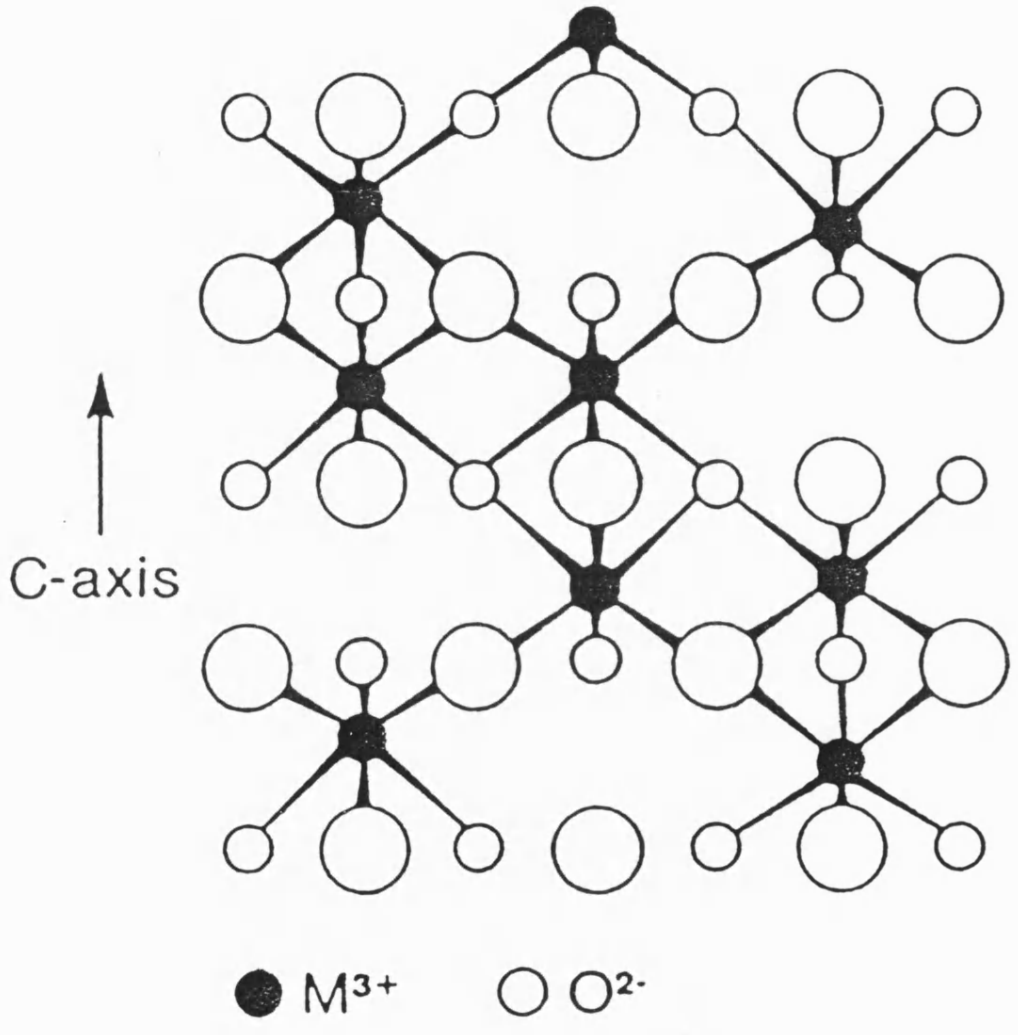

Figure 4.1: Corundum Structure

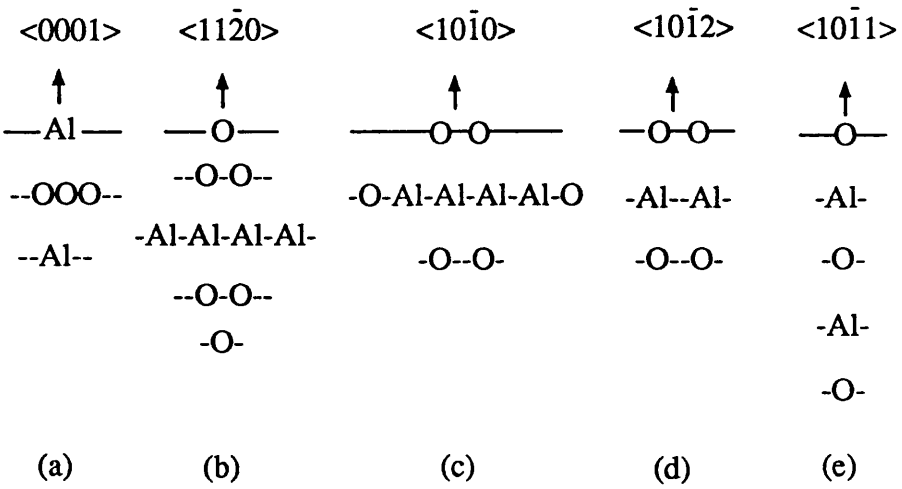

Figure 4.2: The stacking sequences of the five lowest index surfaces of α-Al_2O_3

the available sites whereas the oxygen ions on other planes are coordinated to four aluminiums (47). The two prism planes at right angles to the basal plane are shown in figures 4.2(b) and 4.2(c). The $\{11\bar{2}0\}$ surface is terminated by a plane of anions, which are not quite coplanar. The second prism plane ($\{10\bar{1}0\}$), consists of cations and anions in stoichiometric ratio, although some of the anions deviate slightly from the mean plane. The rhombohedral $\{10\bar{1}2\}$ plane terminates in a layer of anions and is shown in figure 4.2(d). The second rhombohedral face $\{10\bar{1}1\}$, shown in figure 4.2(e), consists of a single column of Al_2O_3 formula units which produces a fully dense surface plane of anions.

4.4 Pure Surface Energies

Two potential models (one empirical and one non-empirical) were used in the calculations in order to find out how sensitive the results were to the potential model. These potentials were derived previously by the methods outlined in Chapter 3.

The non-empirical potential has already been used by Mackrodt (149) to calculate the unrelaxed and relaxed surface energies of the five low index surfaces of α-Al_2O_3. The order of decreasing stability before relaxation was found to be:

$$\{10\bar{1}2\} > \{11\bar{2}0\} > \{10\bar{1}1\} > \{0001\} > \{10\bar{1}0\}$$

and on relaxation was:

$$\{0001\} > \{10\bar{1}0\} \approx \{10\bar{1}2\} > \{11\bar{2}0\} \approx \{10\bar{1}1\}$$

The unrelaxed energies ranged from 6.46 to 3.63 Jm^{-2} and the relaxed energies were much lower - between 2.52 and 2.03 Jm^{-2}.

The order of stability of these surfaces, however, has not been determined using the empirical potentials. The unrelaxed and relaxed energies of the five surfaces are given in table 4.1 and show that, although the unrelaxed order is identical to the non-empirically derived one, the relaxed order of decreasing stabilities is different:

$$\{10\bar{1}2\} > \{0001\} > \{11\bar{2}0\} > \{10\bar{1}0\} > \{10\bar{1}1\}$$

There are three possible reasons for this discrepancy. Firstly, the empirical potentials do not include any cation-cation interactions. However, the surface stabilities did not change when they were recalculated using non-empirical potentials with no cation-cation interactions. Secondly, the core and shell charges for the ions are different in the two models. However, the oxygen polarisabilities (which are much greater than those of the cations and thus have the greatest effect on relaxation) are comparable for the two models. Thirdly, the short range interactions for the empirical potentials are only calculated at the perfect lattice ion positions. For other separations they are assumed to follow an exponential function of the form given by equation 3.7. Therefore, the difference in the calculated ordering in surface stabilities is attributed to this approximation in the empirical model. Since the discrepancy in the order of stabilities is due to small differences in the calculated surface energies, which are not significant when compared to the surface energies, both potentials were used to investigate impurity segregation.

The remainder of this chapter deals with the calculations on magnesium and calcium segregation at the basal and $\{10\bar{1}0\}$ prism surfaces of α-Al_2O_3 because there is experimental data with which to compare (150,151). The relaxed structures of these pure surfaces using the empirical potentials are shown in figures 4.3 and 4.4. At the basal plane only one-third of the available cation sites are filled whereas in the bulk

Table 4.1: Calculated surface energies (Jm^{-2}) of α-Al_2O_3 using the empirical potential

Surface	Unrelaxed Energy	Relaxed Energy
{0001}	5.90	2.30
$\{10\bar{1}0\}$	6.52	2.73
$\{10\bar{1}2\}$	3.60	2.24
$\{11\bar{2}0\}$	4.74	2.50
$\{10\bar{1}1\}$	5.79	2.95

Figure 4.3: Pure basal surface of α-Al_2O_3 before and after relaxation

Before Relaxation	After Relaxation	Percentage Contraction
-Al-		
	-Al-	86%
-O-O-O-	-O-O-O-	
		-15%
-Al-	-Al-	
	-Al-	36%
-Al-		
		-25%
-O-O-O-	-O-O-O-	
		-14%
-Al-	-Al-	

Figure 4.4: Pure prism surface of α-Al_2O_3 before and after relaxation

Before Relaxation	After Relaxation	Percentage Contraction
-O-	-O-	
Al-O-Al	Al, O, Al	-69%
-O-	-O-	
		-0.6%
-O-	-O-	
Al-O-Al	Al, Al, O	-5%
-O-	-O-	
		15%
-O-	-O-	
Al-O-Al	Al-O-Al	-7%
-O-	-O-	

two-thirds of these sites are occupied (47). The decrease in cation occupancy leads to a dramatic contraction of this surface on relaxation. The prism surface, which has a stoichiometric stacking sequence, terminates at an oxygen plane. On relaxation, the surface expands and the cation planes rumple as the repulsion between oxygen ions is relieved. Although the order of stability of the five surfaces is different for the two potential models, they both predict that the basal surface is more stable than the prism surface (the calculated non-empirical energies are 2.03 Jm^{-2} and 2.23 Jm^{-2} for the basal and prism surfaces respectively and compare with the empirical results given in table 4.1). Also the relaxed structures are similar.

As calcium and magnesium are aliovalent impurities the nature of charge compensating defects must be considered. The possible charge compensating defects for the acceptor M_{Al}' (M=Ca,Mg) in alumina are $V_O^{\cdot\cdot}$, $Mg_i^{\cdot\cdot}$ and $Al_i^{\cdot\cdot\cdot}$ (note that the Kroeger-Vink (152,153) notation is used throughout this thesis to describe the defect types. This is summarised in Appendix 4). James (42) has shown that the solution energies of magnesium in the bulk with these charge compensating defects only differ by 0.6 eV and, therefore, the defect structure will be by no means simple (154). However, when defect association is considered, the most stable aggregates seem to form with oxygen vacancies (154) and this has been confirmed by precipitation studies of MgO in α-Al_2O_3 (143). Therefore, the charge compensating defects are considered to primarily be oxygen vacancies. Segregation energies are then defined as the difference in substituting the impurity with charge compensating oxygen vacancies in the bulk and at the surface. This is discussed in the following sections.

4.5 Bulk Solution and Binding Energies

The bulk substitution, solution and binding energies of calcium with oxygen vacancies, calculated using the empirical and non-empirical potentials, are given in

Table 4.2: Substitution and isolated solution energies of Ca_{Al}' and $V_O^{\cdot\cdot}$ in α-Al_2O_3 using the empirical and non-empirical potentials (energies in eV)

	Empirical	Non-Empirical
Ca_{Al}'	36.4	37.0
$V_O^{\cdot\cdot}$	24.6	21.6
Solution Energy*	5.0	4.7

* per calcium

Table 4.3: Binding and solution energies of $(Ca_{Al}'\text{-}V_O^{\cdot\cdot}\text{-}Ca_{Al}')^x$ using the empirical and non-empirical potentials (energies in eV)

	Empirical	Non-Empirical
Binding Energy*	1.8	1.1
Solution Energy*	3.2	3.6

* per calcium

tables 4.2 and 4.3. The agreement between the energies calculated by the different potentials is favourable and the defect cluster is strongly bound. Magnesium solution in the bulk of α-Al_2O_3 was re-examined using the potential derived by Catlow and Lewis (120) and it was found that the solution and binding energies concur with those previously calculated by James (42). The calculated solution energies of calcium are much higher than those of magnesium because of the greater mismatch in ion size between calcium and aluminium (the ionic radii of Al^{3+}, Mg^{2+} and Ca^{2+} are 0.45, 0.68, 1.03 Å respectively (18)). In both cases the high binding energy of the clusters reduces the solution energies considerably.

4.6 Surface Binding Energies

The binding energy of the magnesium cluster at the basal plane has already been determined by Mackrodt and Tasker (148) and is greater than in the bulk because of favourable image charge interactions (see section 2.6). The same result was also found for the magnesium cluster at the prism plane which has a binding energy of 1.90 eV (per Mg) and compares with the bulk value of 1.20 eV (per Mg). The corresponding binding energies for the calcium cluster at the basal plane are 1.94 and 2.42 eV (per Ca) for the empirical and non-empirical potentials respectively, whereas those at the prism plane are 1.10 and 0.83 eV (per Ca) are also high. It should be noted, however, that the large ion size mismatch of calcium with aluminium at the prism plane serves to lower the binding energy despite the favourable image interactions. This is because the surface binding energy is also influenced by the difference in relaxation about the isolated and bound impurity. In the case of the prism surface, the increase in the binding energy due to the favourable image interactions is predicted to be more than compensated for by the decrease in relaxation of the bound cluster. It also results in a surface binding energy that is lower

than in the bulk. Thus, the difference in surface and bulk binding energies is controlled by a delicate balance between steric strain due the difference in ion size and surface relaxation which includes both electrostatic and short range interactions. A similar argument has been used by Mackrodt (147) to account for the unfavourable segregation of Y^{3+} to the basal surface of α-Al_2O_3.

In view of the high cluster binding energies, the impurities are treated as segregating as the neutral cluster $(M_{Al}'\text{-}V_O^{\cdot\cdot}\text{-}M_{Al}')^x$, (M=Ca,Mg). By adopting this approach, the interaction of the dipole, that is associated with the cluster with the space charge that may form at the surface, need only be considered. Yan et al. (156), however, have shown that for low bulk defect concentrations and high temperatures this is small and the extent to which it changes the surface charge is negligible. Hence, this interaction is also neglected.

4.7 Calcium Segregation to the Basal Plane

Three possible orientations of the calcium cluster at the basal surface were considered. These lead to either a configuration parallel to the surface where calcium is incorporated in the first cation layer, or a configuration at approximately 45 degrees to the surface where calcium ions are incorporated in the first and second or first and third cation planes. These cluster orientations are indexed (1,1), (1,2) and (1,3) respectively and are shown in figure 4.5. The variation of their segregation energies with coverage is shown in figure 4.6 for the empirical potential. The results indicate that at thermodynamic equilibrium the defect cluster will segregate and give the orientation parallel to the surface at all coverages considered and that it does not exhibit Langmuir behaviour. As the defect concentration is increased from zero to one quarter coverage, the segregation energy becomes less exothermic by 0.25 eV. Around 33% coverage there is evidence for the formation of a stable phase of

Figure 4.5: Surface configurations of the (Ca_{Al}'-V_O-Ca_{Al}') at the basal surface of α-Al_2O_3

	Pure surface		Defective surface		
plane 1	- Al -		- Ca_{Al}' -	- Ca_{Al}' -	- Ca_{Al}' - Ca_{Al}' -
	- O -		- V_O·· -	- V_O·· -	- V_O·· -
plane 2	- Al -		- Ca_{Al}' -	- Al -	- Al -
plane 3	- Al -	<0001>	- Al -	- Ca_{Al}' -	- Al -
	- O -		- O -	- O -	- O -
plane 4	- Al -		- Al -	- Al -	- Al -
			(1,2)	(1,3)	(1,1)

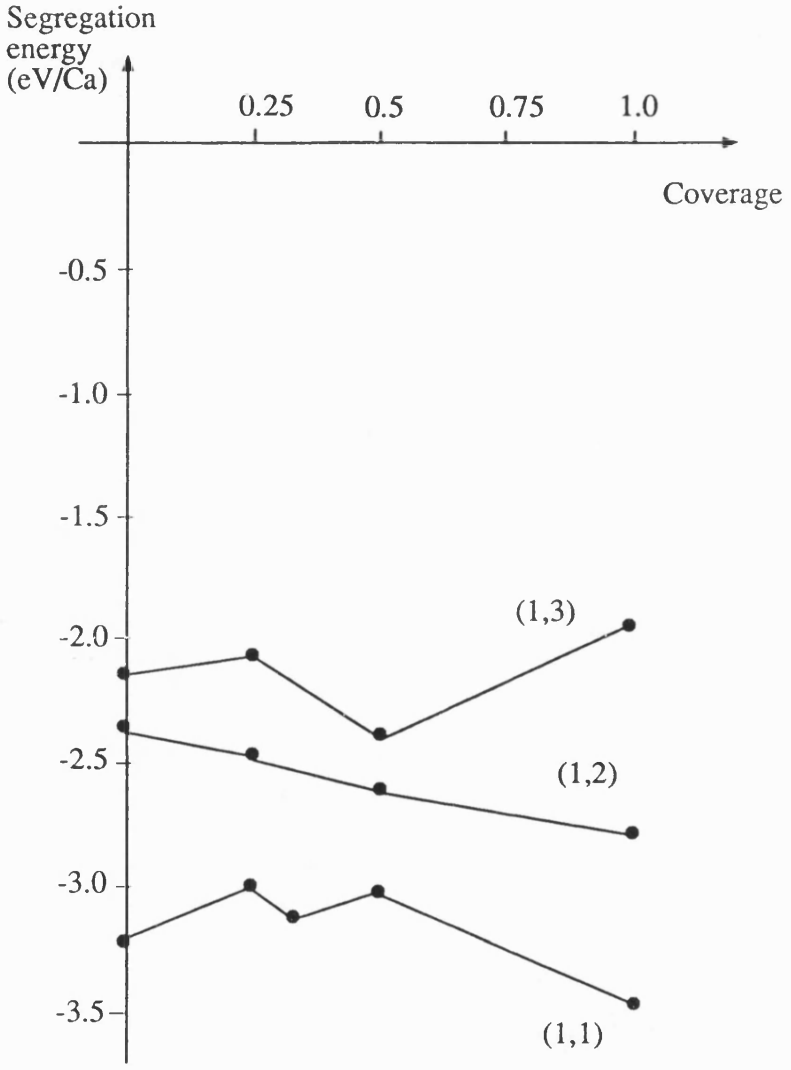

Figure 4.6: Calculated segregation energy of calcium at the basal surface as a function of coverage

composition $CaAl_2O_4$. There is also a minimum at 100% coverage corresponding to a two dimensional phase of CaO. From the phase diagram (157) between CaO and Al_2O_3, compounds of formula $CaAl_{12}O_{19}$, $CaAl_4O_7$, and $Ca_3Al_2O_6$, as well as $CaAl_2O_4$ are stable. Apart from $CaAl_2O_4$, surfaces with these compositions require calculations that exceed the available computer resources and therefore direct comparison is currently not possible.

The segregation isotherm of the (1,1) configuration, calculated using the non-empirical potential, is compared to that of the empirical potential in figure 4.7. Although the quantitative agreement in the segregation energies is poor, qualitatively the behaviour is comparable. The difference in the segregation energy at a given coverage is 1.2 eV (per Ca) less for the non-empirical potential of which 0.2 eV is due to the difference in bulk substitution energies. Segregation is strongly favoured at all coverages. The difference in the segregation energies can be attributed to the greater relaxation of the pure surface using the non-empirical potential (the difference in relaxed and unrelaxed pure surface energies is 3.92 Jm^{-2} which compares with 3.60 Jm^{-2} for the empirical potential). Incorporation of impurity ions with a large mismatch in ion size at the basal surface is predicted to have a greater destabilising influence on surface stability using non-empirical potentials. To check if this mismatch due to the lack of cation-cation interactions in the empirical potential the non-empirical values were recalculated without these interactions. The results, however, were the same and therefore it was concluded that, as for the pure surface calculations (in section 4.4), the difference is due to the different methods by which the short range interactions were determined.

These results are in agreement with the calculations of Davies et al. (158) who found that magnesium segregates to give the (1,1) orientation parallel to the basal plane of Cr_2O_3, although in this case Langmuir behaviour was exhibited at all coverages considered. Mackrodt and Tasker (148) showed that magnesium also

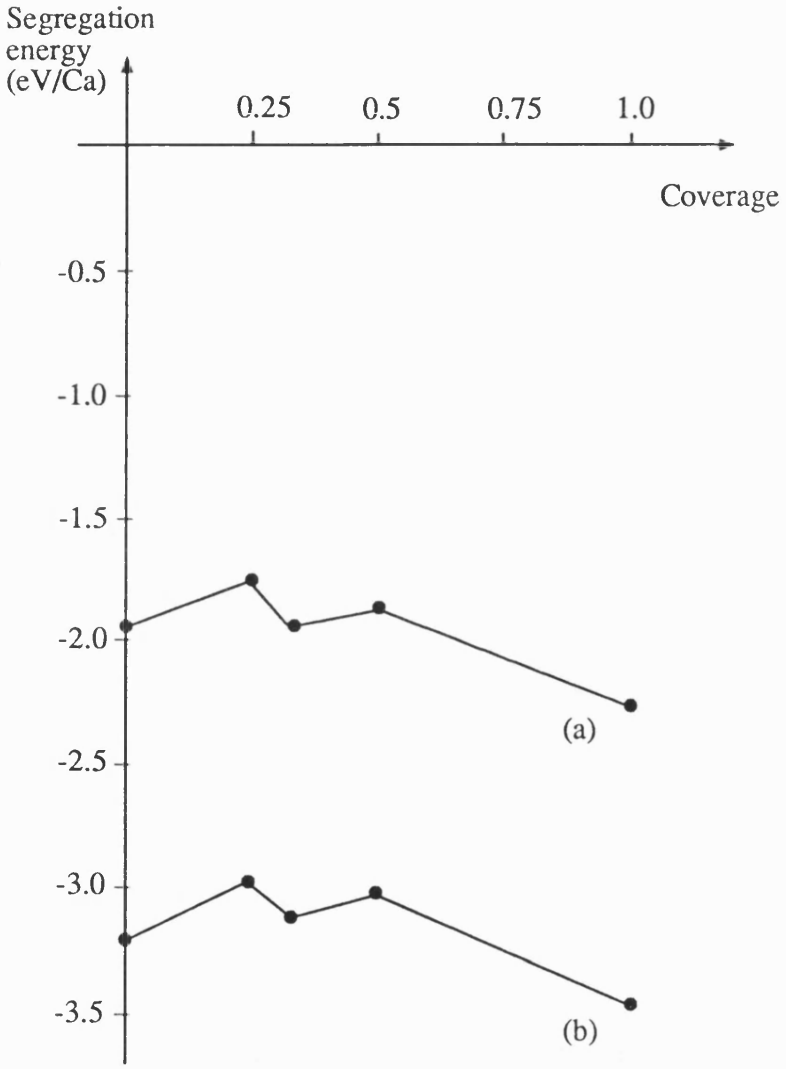

Figure 4.7: Calculated segregation energy of calcium to the basal surface as a function of coverage using
(a) the non-empirical potential
(b) the empirical potential

segregates to the basal surface of α-Al_2O_3 but the (1,4) cluster orientation is preferred. They compared their results with the experiments of Baik et al. (36) who determined a segregation enthalpy of -1.51 eV from a plot of log (surface coverage) against reciprocal temperature which is in good agreement with the theoretical result of -1.64 eV. Mackrodt and Tasker also attributed the surface reconstruction observed experimentally by LEED to be due to the formation of a two dimensional ordered spinel phase.

The experimental evidence for calcium segregation to this surface is unclear. Baik et al. (36) investigated magnesium segregation to the {0001} surface of sapphire and found that the surface magnesium distribution was uneven. In areas where magnesium was absent, calcium was present in high concentrations. They suggested that this indicated some sort of repulsion between the two cations and that calcium enrichment was due to small surface precipitates. In contrast, Baik and White (150) found no evidence for calcium segregation to the basal plane of a single crystal doped with approximately 40 ppm of calcium. The absence of calcium segregation was attributed to kinetic factors (150,159). Thus, the apparent mismatch between theory and experiment would seem to arise from kinetic factors because thermodynamic equilibrium was not attained in the experiments.

Within the confines of the models used in this thesis, the kinetics of diffusion can be investigated by calculating the activation energy of the migration of Ca^{2+} ions between two adjacent aluminium vacancies. The two vacancies were chosen to be perpendicular, parallel and at 45 degrees to the <0001> direction in the bulk. The activation energies, calculated using the empirical potential, are given in table 4.4 and show that migration is isotropic. Indirect support for these results comes from two sources. Firstly, Ando (160) has determined an experimental activation energy for Mg^{2+} ions in α-Al_2O_3 as 2.4 ± 0.3 eV at low impurity concentrations. This activation energy is lower than that reported here for Ca^{2+} but this is to be expected because the

Table 4.4: Calcium activation energies (eV)

Migration Pathway	Activation Energy
Parallel to c-axis*	3.1
Perpendicular to c-axis	3.4
At 45 degrees to c-axis	3.3

* the c-axis is perpendicular to the basal plane

lattice strain arising from Ca^{2+} is much greater than that for Mg^{2+} in α-Al_2O_3 (161). Magnesium would, therefore, successfully compete for surface cation sites which would account for the 'repulsion' observed by Baik et al. Secondly, Stubican and Osenbach (162) showed that ^{51}Cr lattice diffusion in α-Al_2O_3 is isotropic which is in accord with the results presented in table 4.4. Thus, anisotropic bulk diffusion cannot account for the lack of calcium segregation at the basal surface.

The migration behaviour of ions in the sub-surface region will not necessarily be the same as in the bulk. Therefore, point defect formation energies were also calculated using the empirical potential for V_{Al}''', Mg_{Al}' and Ca_{Al}' as a function of depth in the sub-surface region of the basal plane. The results, given in figure 4.8, show that the cation vacancy energy varies with distance from the surface and approaches the bulk value around the 7th cation plane (approximately 6 Å) below the surface. This is expected in view of the large relaxations seen in figure 4.3 which lead to enhanced stability of vacancy sites on the 4th and 5th cation planes. Also shown in figure 4.8 are Mg_{Al}' and Ca_{Al}' energies with depth which show a maximum around the 3rd and 4th cation planes. The difference in the energy between the 4th and 5th planes are 0.50 eV for Mg_{Al}' and 1.40 eV for Ca_{Al}'. Substitution of calcium at the 2nd cation plane is unstable and the calcium ion migrates directly to the surface. Thus, enrichment of the surface by magnesium and the sub-surface by calcium might be expected as the energy barriers are markedly different. It remains to be seen, however, whether such a subtle difference can be detected by experiment.

4.8 Calcium and Magnesium Segregation to the Prism Plane

Both magnesium and calcium segregation to the prism plane of α-Al_2O_3 were investigated. Only one cluster orientation was chosen with all the impurities lying in the first cation plane. The excessive computer cpu time taken to relax this surface

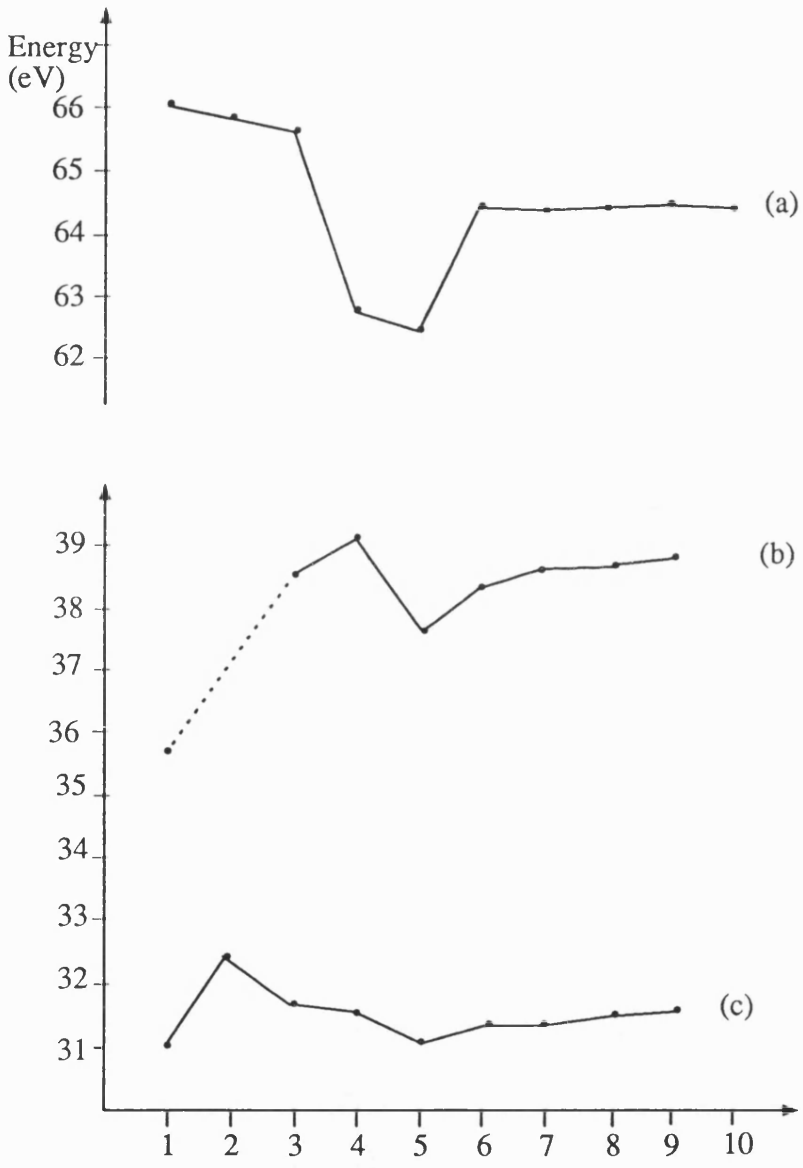

Figure 4.8: Variation of (a) aluminium vacancy (b) calcium substitution and (c) magnesium substitution energy from the basal surface

precluded further investigation of defect cluster orientations. In addition, relaxation of the defect free surface produced a rumpled cation plane in which a number of different possible cluster orientations were possible, the most favourable of which involved nearest neighbour ion sites.

The calculated segregation energies, using empirical potentials, as a function of magnesium defect cluster concentration are given in figure 4.9 and compared to those of calcium. The segregation energy for the magnesium cluster becomes more exothermic by approximately 0.3 eV between zero and one quarter coverage. At coverages greater than 25% the segregation energy rises by 0.3 eV but is still negative. Above 75% surface coverage there is some evidence for the formation of a two dimensional phase of MgO. Calcium segregation at this surface shows similar behaviour, but is much more exothermic - as might be predicted from the larger mismatch in ion size for Ca^{2+} and Al^{3+}, and hence larger cluster size. No evidence for the formation of a second phase of composition CaO is observed which is probably because the distances between the cation sites at this surface are smaller than at the basal plane. The relaxed structure of this surface is thus much more tightly packed and less able to accommodate the larger CaO phase. Stable phases are, however, seen for surface coverages of approximately 25%, but as before the exact minimum cannot be located because of the small number of points that could be calculated. Comparison with non-empirical potentials for calcium show much better quantitative agreement at this surface as seen in figure 4.10.

4.9 Segregation Isotherms

An important aim of this work is to establish the reliability (or otherwise) of these techniques. This can be done by comparing the calculated surface coverage with that determined by experiment. The above calculations give the variation of the

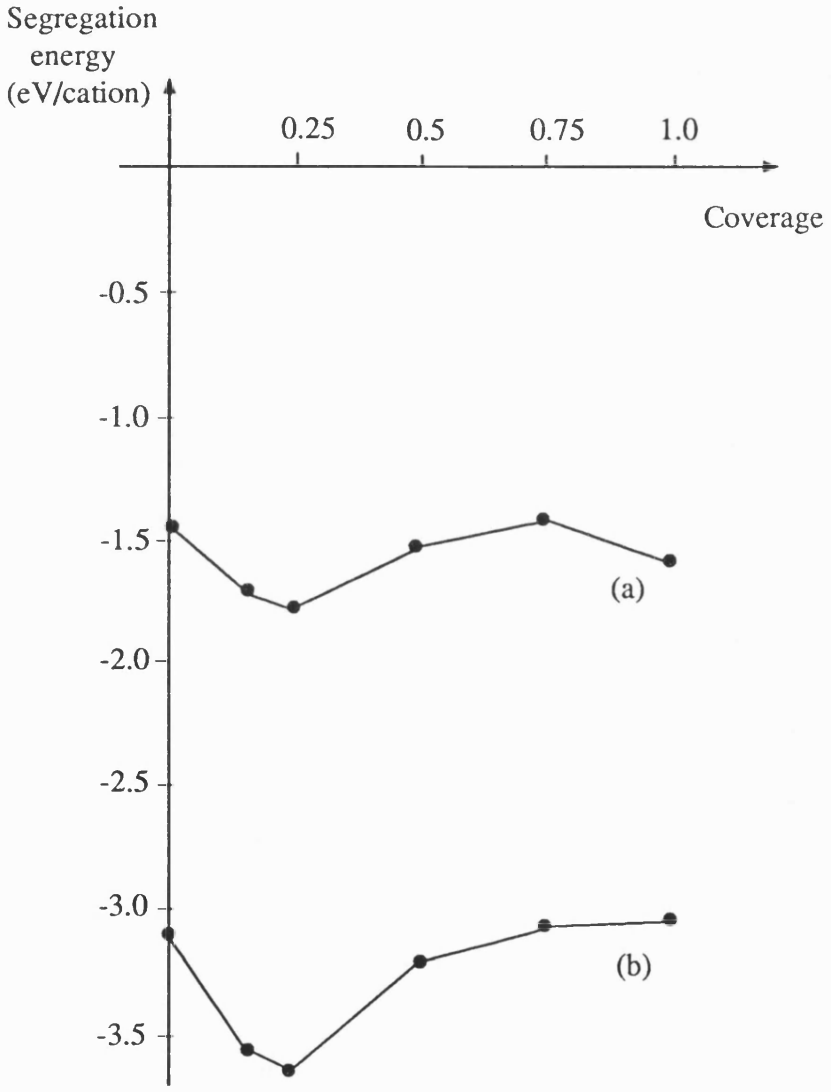

Figure 4.9: Calculated segregation energy of (a) magnesium and (b) calcium to the prism surface as a function of coverage

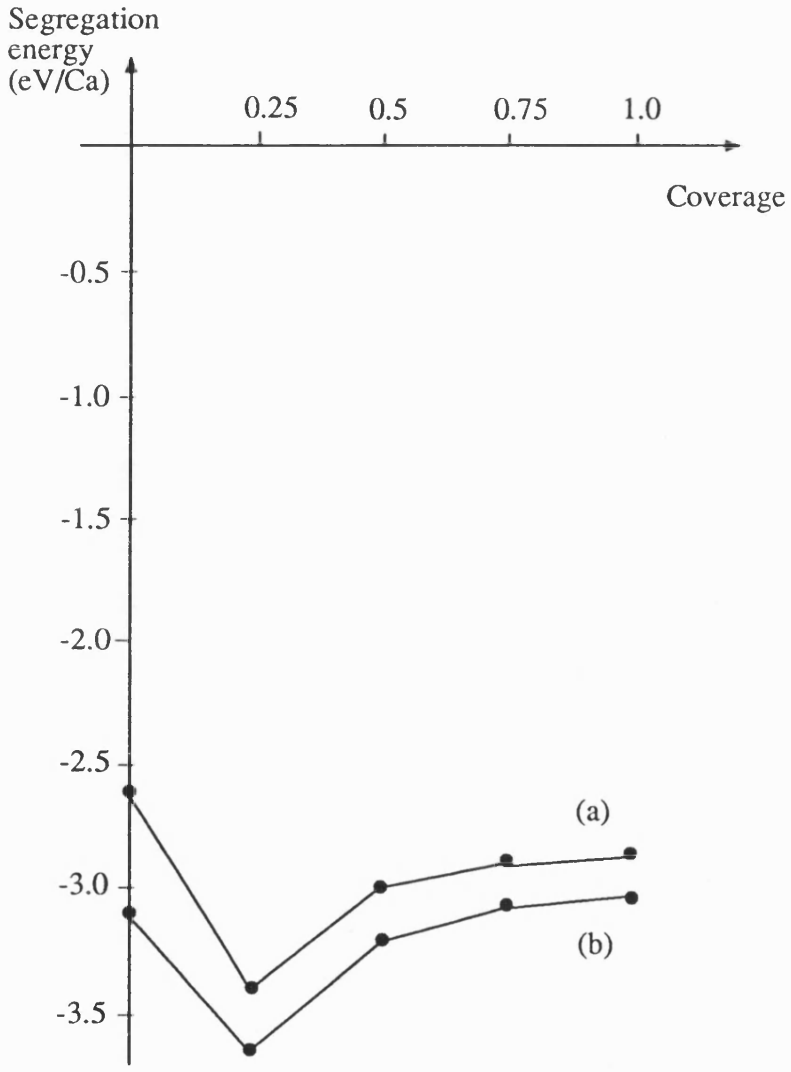

Figure 4.10: Calculated segregation energy of calcium at the prism surface as a function of coverage using
(a) the non-empirical potential
(b) the empirical potential

segregation potential energy at 0 K with coverage. To calculate surface defect concentrations at elevated temperatures the following equation is used:

$$C_s = \frac{1}{1 + (C_b A)^{-1} \exp\left[\left(\Delta h + C_s \frac{d\Delta h}{dC_s} / kT\right)\right]} \qquad (4.35)$$

where A, the pre-exponential factor, is related to the entropy of segregation via:

$$A = \exp\{\Delta s/k\} \qquad (4.36)$$

Note that the other variables have the meanings given in section 4.2. Thus, the enthalpy, Δh, and the entropy, Δs, of segregation are required.

Here, Δh is identified with the potential energies calculated above and the justification for this is as follows. The relationship between the formation enthalpy at constant pressure h^P, and the formation internal energy at constant volume u^v is (163):

$$h^P = u^v - T\beta_P\Omega(du^v/d\Omega)_T \qquad (4.37)$$

where β_P is the volume expansivity of the bulk material and Ω is the defect formation volume. Assuming (163) the change in the internal energy, Δu^v due to the increase in volume is proportional to corresponding increase in temperature then:

$$\Delta u^v = (du^v/d\Omega)[\Omega(T) - \Omega(0)] \approx T\beta_P\Omega(du^v/d\Omega) \qquad (4.38)$$

Thus the change in the internal energy due to the increase in volume compensates for the difference between h^P and u^v. A similar argument (164) can be applied to

formation enthalpies at the surface, although in this case the internal energy is calculated at constant area. As the difference in the internal energy of the defective and pure lattice is equal to the sum of the difference in the zero point energy (which is negligible) and the difference in the potential energy the identification of Δh with the potential energy would seem to be entirely satisfactory.

From equation 4.35, the change in vibrational entropy of segregation is also required. If it is assumed that this term is small and does not vary appreciably with either surface coverage or temperature, then Δs can be estimated from experiment. This is now done for magnesium and calcium segregation at the prism surface.

The plots of surface coverage against temperature for calcium and magnesium at the prism plane are given in figures 4.11 and 4.12. The pre-exponential factor, A for magnesium segregation was taken as 1.6×10^{-2}, which corresponds to a segregation vibrational entropy of 3.55×10^{-4} eVK^{-1}. The theoretical plot compares favourably with experiment (151), but as the plot is not linear, it is difficult to determine a value of H given by equation 4.34 which is independent of temperature. It is more appropriate to take the atomistic definition (equation 4.20) of the segregation enthalpy which can be found from figure 4.9.

For calcium segregation, the vibrational entropy was taken to be 1.24×10^{-3} eVK^{-1} and was extrapolated from the results of Mukhopadhyay et al. (151). The results are compared with those of Mukhopadhyay et al. and Baik and White (150) in figure 4.12. The qualitative agreement is again good and the variation of the logarithm of surface coverage with temperature is approximately linear. In this case the value of H is determined to be about -1.2 eV (per Ca). Note that this is markedly different from the atomistic definition of segregation which does vary with coverage (see section 4.2).

In the above account of segregation, the effects of temperature have been

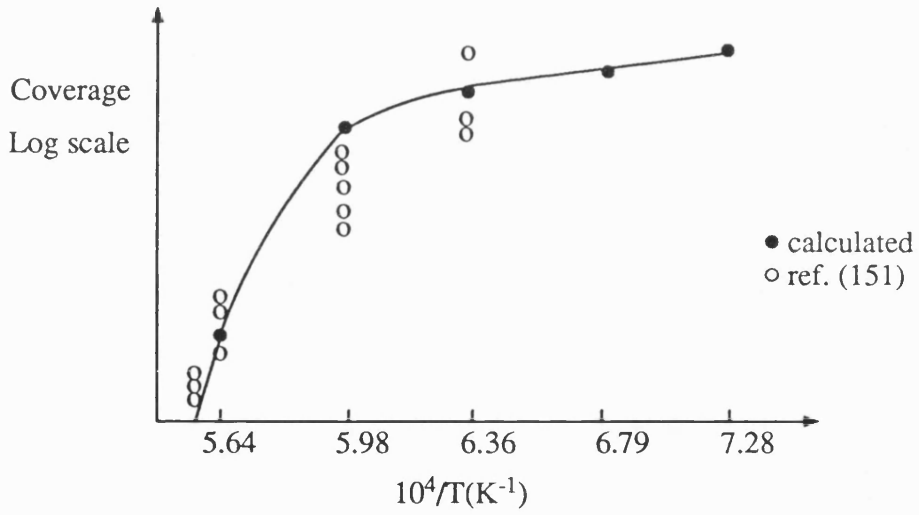

Figure 4.11: Comparison of the calculated and experimental (151) coverages with temperature of magnesium at the prism surface

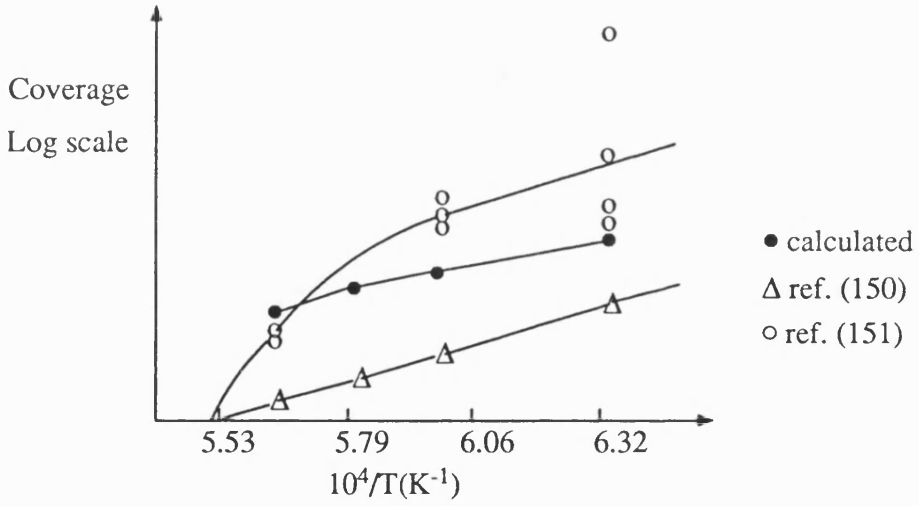

Figure 4.12: Comparison of the calculated and experimental (150,151) coverages with temperature of calcium at the prism surface

incorporated by making various approximations. Comparison with experiment shows that these are indeed reasonable, albeit for the systems investigated. It would, however, be useful to relax these approximations and calculate the effects of temperature by including the vibrational properties of the lattice explicitly. Segregation isotherms could then be predicted without fitting to the experimental results. Accordingly, in the next section, results from a preliminary study on the thermodynamic properties of the pure and defective basal surface of α-Al_2O_3 at elevated temperatures are presented. From these results the segregation free energy of calcium at the basal surface of α-Al_2O_3 is calculated.

4.10 Segregation Free Energy of Calcium at the Basal Plane

In the remainder of this chapter the calculation of the segregation free energy of calcium at the basal surface, using lattice dynamics (see section 2.7), is described. The simulations were performed with the empirical potential and the key results compared with those calculated using the non-empirical potential. The reliability of the calculations was also investigated by recalculating the thermodynamic properties at 100 and 1000 K using more reciprocal lattice points. The sampling points that were used are given in chapter 2.

Four calculations are required to determine the segregation free energy for a given lattice parameter or temperature. They are:

a. The free energy of the pure surface;

b. The free energy of the defective surface;

c. The free energy of the pure bulk;

d. The free energy of the defective bulk.

The segregation free energy is obtained from the difference in substituting the defect at the surface and in the bulk.

Both the harmonic and quasi-harmonic approximation were used to calculate the segregation free energy. In the harmonic approximation the thermodynamic properties are found for the 0 K minimum energy structure and, therefore, lattice expansion is neglected. In contrast, in the quasi-harmonic approximation the thermodynamic properties are calculated for the equilibrated structure at the given temperature. The equilibrated structure is found by minimising the kinetic pressure with respect to the volume of the lattice.

4.10.1 Lattice Expansion of α-Al_2O_3

The volume and linear expansion coefficients of α-Al_2O_3 were calculated using the quasi-harmonic approximation. The volume expansion coefficient (α_V) for a change in volume ($V_{T''}$-$V_{T'}$) from temperatures T' to T'' is given by:

$$V_{T''} = V_{T'} [\, 1 + \alpha_V \Delta T \,]$$

where

$$\Delta T = T'' - T' \text{ and } T'' > T'$$

An analogous equation gives the change in lattice parameter with temperature.

The supercell that was used to calculate the change in lattice parameter with temperature contained sixteen formula units of Al_2O_3 (80 ions). A supercell was employed so that the final basis of coordinates and lattice vectors could be used in the surface calculations. The other advantage of using large unit cells is that the number of sampling points in reciprocal space is less than that required for a primitive unit cell. This is because of the folding back of the phonon dispersion curve towards the

Brillouin zone centre (165). A linear expansion coefficient was also calculated from the cube root of the volume. As α-Al_2O_3 expands anisotropically, the latter should only be compared with polycrystalline experimental data.

Over the temperature range considered, 100 to 1000 K, the volume and linear expansion coefficients, calculated using one reciprocal lattice point, are 1.04×10^{-5} K^{-1} and 3.47×10^{-6} K^{-1} for the empirical potential and 1.18×10^{-5} K^{-1} and 3.91×10^{-6} K^{-1} for the non-empirical potentials. The agreement between the two potential models is good. The linear expansion coefficients were also calculated for the empirical model over the temperature ranges 100-500 K and 500-1000 K. They are 2.39×10^{-6} K^{-1} and 4.33×10^{-6} K^{-1}. These compare with experimental linear expansion coefficients of 2.7×10^{-6} K^{-1}, 6.8×10^{-6} K^{-1}, 8.3×10^{-6} K^{-1} and 8.33×10^{-6} K^{-1} for the temperature ranges 123 to 293, 293 to 533, 533 to 1253 and 293 to 1253 K respectively (166).

The volume coefficient of expansion at 100 and 1000 K was recalculated for both potentials using 8 reciprocal lattice points. The coefficents over the temperature range 100 to 1000 K were 3.46×10^{-6} K^{-1} and 3.93×10^{-6} K^{-1} for the empirical and non-empirical potentials. A further calculation with 27 points was precluded because of the excessive computer memory required. However, the predicted expansions using 1 and 8 reciprocal lattice points were in good agreement and, therefore, it was concluded that the calculated thermodynamic properties had converged. There are two further reasons as to why the experimentally and theoretically determined expansion coefficients do not agree. The first is that the potential models are inaccurate. The agreement between the two potentials and their success in modelling crystal properties (see for example reference (167)) would seem to suggest that this is not a major source of error. The other, and more likely, reason is due to deficiencies in the quasi-harmonic approximation. These may arise because the lattice energy is only expanded to second order in the lattice displacements (section 2.3) and higher order

terms are neglected. This is reasonable for lattice vibrations which do not sample large volumes of reciprocal lattice space. At high temperatures ionic displacements due to vibrations are much larger and anharmonic terms, which tend to decrease the vibrational frequencies of the phonons will become important. Thus at a given temperature more phonon modes will be occupied than are predicted by the quasi-harmonic approximation and so the vibrational contribution to the free energy of the crystal is greater (168). The predicted expansion coefficients will then be less than those observed experimentally and this is what is found here.

4.10.2 Basal Surface Free Energy

The surface calculations were performed on two dimensional slabs which were separated by three lattice units. The slabs themselves consisted of 80 ions with 24 planes stacked in the <0001> direction. The top and bottom of the slabs thus represented free basal surfaces. The separation and number of planes in the stack was chosen so that the surface energy had converged. The independence of the two surfaces was also ensured by checking that the two longest wavelength acoustic phonons or Rayleigh modes were approximately degenerate (56).

The change in the surface free energy with temperature, calculated using one point in reciprocal space for the empirical and non-empirical potentials, is given in table 4.5. Both results for the lattice parameter at 0 K (harmonic approximation) and those for the lattice parameter determined by the quasi-harmonic approximation are included in this table. The main difference between results from the two potentials is that the calculated free energies differ by approximately 0.3 Jm^{-2} and this is consistent with the difference between the potential energy calculations. For the empirical potentials, the surface free energy decreases approximately linearly with temperature and is lower for the quasi-harmonic approximation. The surface free energy was

Table 4.5(a): Calculated basal surface free energies (Jm^{-2}) of α-Al_2O_3

	Empirical		Non-empirical	
Temperature (K)*	Harmonic	Quasi-Harmonic	Harmonic	Quasi-Harmonic
100	2.37	2.36	2.01	1.99
500	2.34	2.32		
1000	2.30	2.27	1.99	1.94
1500	2.26	2.24		
2000	2.23	2.20		

Table 4.5(b): Calculated basal surface free energies (Jm^{-2}) of α-Al_2O_3

	Empirical		Non-empirical	
Temperature (K)	Harmonic	Quasi-Harmonic	Harmonic	Quasi-Harmonic
100*	2.37	2.36	2.01	1.99
100**	2.37	2.35	2.01	1.98
1000*	2.30	2.27	1.99	1.94
1000**	2.29	2.26	1.98	1.93

* 1 k-point used for both surface and bulk

** 8 k-points used for the bulk and 4 k-points for the surface

recalculated using more sampling points in reciprocal space at 100 and 1000 K and these results are compared with those calculated with one reciprocal lattice point in table 4.5. It can be seen that the calculations are indeed consistent and it is concluded that the surface thermodynamic properties have converged. Note that only 4 points were used for the surface calculation in comparison with 8 for the bulk. This is because slabs have a lower periodicity than the bulk and hence only points in the first two-dimensional rather than the three-dimensional Brillouin zone need to be sampled (169).

The surface entropies for the empirical and non-empirical models, determined from the change in the free energy (harmonic) with temperature are 6×10^{-5} and 3×10^{-5} $Jm^{-2}K^{-1}$ respectively. These compare favourably with calculated values for two NiO grain boundaries of 6.3×10^{-5} and 15×10^{-5} $Jm^{-2}K^{-1}$ (61). An experimentally determined surface energy of a polycrystalline sample of alumina at 2123 K is 0.9 Jm^{-2} (153). If it is assumed that a polycrystalline sample is composed of equal areas of each of the five low index surfaces investigated above, then at absolute zero its surface energy will be 2.55 or 2.31 Jm^{-2} for the empirical and non-empirical potentials respectively. The surface energy at 2123 K can then be estimated by noting that the decrease in the basal surface free energy determined by the quasi-harmonic approximation is either 9×10^{-5} or 6×10^{-5} $Jm^{-2}K^{-1}$. Thus the predicted surface energies at 2123 K are 2.36 and 2.18 Jm^{-2}. These are much higher than the experimental values and this is to be expected if anharmonic terms contribute significantly to the lattice energy.

The surface structure of corundum has been studied by LEED (170) and the observed (1x1) pattern corresponds to the structure used in the zero Kelvin determination of the surface energy. When this surface was heated more complex structures related to supercells formed. Similar behaviour has been observed for the {0001} surface of α-Fe_2O_3 (171). The larger cells relate to either changes in surface

stoichiometry or may indicate that the (1x1) cell is metastable at higher temperatures. Mackrodt and Tasker (148) have attributed such a transformation on heating to the segregation of magnesium at this surface. Indirect support for this is obtained from the calculations reported here on the pure surface because no imaginary vibrational frequencies were found over the temperature range investigated. Imaginary modes correspond to the development of soft phonons in the vibrational spectrum and these have been invoked by Trullinger and Cunningham (172) to explain surface reconstruction. However, it should be noted that only one reciprocal lattice point is used to represent the phonon frequencies over the temperature range of 100 to 2000 K. Phonon softening may still occur at other k-points. If impurities do cause the change in the LEED pattern then this could also account for the low experimentally determined surface energy. As defects segregate to the surface, then the surface energy decreases (173). Note that the surface energies that were used to predict the surface energy of the polycrystalline material at elevated temperatures did not include any impurities. Also, the possibility of oxygen evaporation at the surface was not investigated which has been observed by French and Somorjai (33).

4.10.3 Surface Substitution Free Energies

For the calculation of the defective surface, monolayer coverage was assumed. This was partly because the potential energy calculations indicated that a stable phase was formed around this composition. The primary reason, however, was that lower surface coverages required bigger unit cells which were computationally prohibitive. The orientation of the defect cluster considered was the (1,1) configuration in accord with the calculations outlined in section 4.7 and was substituted into one of the surfaces of the slabs.

The surface substitution free energy is calculated from the difference between

the defective and pure surface energy. The variation of the substitution free energy with temperature for both potentials using the harmonic and quasi-harmonic approximation is given in table 4.6. As with the surface free energies these do not vary appreciably with temperature, although they are slightly lower for the quasi-harmonic approximation. The dependence of the free energy on the number of k-points was checked for the empirical potential and the results are given in table 4.6. As before, there is little difference between those calculated for 1 and 4 k-points. The entropy of surface substitution is determined from the slope of the free energy versus temperature of the harmonic approximation to be 2.15 x 10^{-4} eVK^{-1} for the empirical and 2.07 x 10^{-4} eVK^{-1} for the non-empirical potential. When compared with that for 50% calcium substitution at the {100} surface of MgO which was found to be 5.17 x 10^{-6} eVK^{-1} (164) this result is high. Thus, the strain induced at the basal surface of α-Al_2O_3 when it is doped with the calcium-oxygen vacancy cluster is much greater than that when magnesium is substituted for by calcium at the {001} surface of MgO. This is to be expected because of the larger size of the cluster. However, the substitution entropy is still small when compared to the potential energy of substitution, lending support to the argument used in section 4.9 where it was assumed that the contribution of this term to the segregation free energy was small.

4.10.4 Bulk Substitution Free Energies

When calculating bulk substitution free energies the free energy of substituting the defect cluster at infinite dilution is required. Harding (174) has developed such an approach, based on the large crystallite method, for the calculation of the entropy of substitution of point defects. This can be combined with potential energies of substitution to give the Helmholtz free energy of the 0 K structure. However, the thermodynamic properties are required at the lattice volume appropriate

Table 4.6(a): Substitution free energies of $(Ca_{Al}'\text{-}V_O^{\cdot\cdot}\text{-}Ca_{Al}')^{\times}$ at the basal surface of $\alpha\text{-}Al_2O_3$ using 1 reciprocal lattice point (energies in eV)

	Empirical		Non-empirical	
Temperature (K)	Harmonic	Quasi-Harmonic	Harmonic	Quasi-Harmonic
100	86.14	86.13	87.73	87.71
500	86.04	86.02		
1000	85.94	85.92	87.54	87.49
1500	85.91	85.87		
2000	85.91	85.37		

Table 4.6(b): A comparison of the substituion free energies of $(Ca_{Al}'\text{-}V_O^{\cdot\cdot}\text{-}Ca_{Al}')^{\times}$ at the basal surface using 1 and 4 reciprocal lattice points (energies in eV)

	Empirical		Non-empirical	
Temperature (K)	Harmonic	Quasi-Harmonic	Harmonic	Quasi-Harmonic
100*	86.14	86.13	87.73	87.71
100**	86.14	86.13	87.73	87.71
1000*	85.94	85.92	87.54	87.49
1000**	85.93	85.91	87.53	87.47

* 1 k-point

** 4 k-points

for the given temperature. Although these can be calculated from the large crystallite method by suitable thermodynamic identities (175), the supercell approach was used in this thesis. This has previously been used to calculate a range of bulk defect thermodynamic properties (see for example Allan et al. (176) and references therein). Only finite defect concentrations can be considered in the supercell approach and, therefore, to reduce possible defect-defect interactions a supercell which contained the same number of ions as the surface calculations (80 ions) was considered, but with suitably modified unit cell lengths. This choice not only ensured that the defect-defect interactions were minimised but also allowed for a check on the convergence of the results. The formula of the unit cell incorporating the defect was $Ca_2Al_{30}O_{47}$.

The change in the bulk substitution free energy with temperature using the empirical potentials is given in table 4.7. Between 100 and 1000 K the free energy of substitution decreases for the harmonic approximation. This corresponds to a positive entropy of substitution (see table 4.7) and compares with the positive value for substitution of calcium in the bulk of MgO calculated by Masri et al. (164). At higher temperatures, however, the substitution free energy increases and this corresponds to a negative substitution entropy (see table 4.7). The free energy of substitution using the quasi-harmonic approximation decreases with an increase in temperature. The decrease in the free energy is dominated by the decrease in the potential energy with increasing volume. The calculated entropies for both the harmonic and quasi-harmonic approximation are given in table 4.7 and decrease with increasing temperature. The free energy and entropy at 100 K and 1000 K, calculated using 8 points in reciprocal space are compared with those using one reciprocal point in table 4.8. The substitution entropies at 100 K calculated with 1 and 8 reciprocal lattice points differ by 6.6×10^{-5} eVK^{-1} (or 27%). The difference in the substitution free energies is negligible because the entropy contribution is small at this temperature. At 1000 K the entropies and free energies are identical and it was concluded that the

Table 4.7: Calculated substitution free energies and entropies of of $(Ca_{Al}'\text{-}V_O^{\cdot\cdot}\text{-}Ca_{Al}')^x$ in the bulk of $\alpha\text{-}Al_2O_3$

	Free energy (eV)		Entropy (10^{-4}eVK^{-1})	
Temperature (K)	Harmonic	Quasi-Harmonic	Harmonic	Quasi-Harmonic
100	93.42	93.23	1.80	1.80
500	93.33	93.05	1.25	1.11
1000	93.32	92.81	-0.53	-0.84
1500	93.37	92.64	-1.58	-0.75
2000	93.47	92.48	-2.33	-3.04

Table 4.8: Calculated solution free energies and entropies of $(Ca_{Al}'\text{-}V_O^{\cdot\cdot}\text{-}Ca_{Al}')^x$ in the bulk of $\alpha\text{-}Al_2O_3$ using the empirical potential (energies in eV)

	Free energy (eV)		Entropy (10^{-4}eVK^{-1})	
Temperature (K)	Harmonic	Quasi-Harmonic	Harmonic	Quasi-Harmonic
100*	93.42	93.23	1.80	1.80
100**	93.41	93.23	2.48	2.48
1000*	93.32	92.81	-0.53	-0.84
1000**	93.32	92.82	-0.53	-0.84

* 1 k-point

** 8 k-points

thermodynamic properties had converged.

The calculated bulk substitution free energies and entropies, using the non-empirical potential, at 100 and 1000 K are given in table 4.9. Within the harmonic approximation, the free energy of substitution using 1 reciprocal lattice point is greater at 1000 K (by 0.15 eV) than that at 100 K. This is because the entropy at 1000 K is negative (see table 4.9). In contrast, the free energy is lower (by 0.30 eV) than that at 100 K using the quasi-harmonic result. This is because the vibrational contribution to the free energy is small when compared to the potential energy. The convergence of these calculations is demonstrated by the agreement of the results for 1 and 8 reciprocal lattice points. Also, the results for the two potential models are comparable.

At the beginning of this section, it was noted that only finite concentrations can be considered within the supercell approach. The influence of impurity-impurity interactions was investigated by increasing the size of the unit cell so that the unit cell formula was $Ca_2Al_{62}O_{95}$ (159 ions). The calculated substitution free energy and entropy, using the quasi-harmonic approximation and 1 reciprocal lattice point, is 92.88 eV and -1.14×10^{-4} eVK^{-1} respectively and compare with the values calculated for the smaller impure unit cell (79 ions) of 92.92 eV and -0.65×10^{-4} eVK^{-1}. A further increase in either the unit cell size or the number of reciprocal lattice points is not possible at present because of restrictive computer resources. The results between the two unit cells are in good agreement and it was concluded that the impurity-impurity interactions are negligible.

4.10.5 Segregation Free Energy

The change in the segregation free energy of calcium to the basal surface of α-Al_2O_3, calculated using empirical potentials, is given in figure 4.13. The

Table 4.9: Calculated solution free energies and entropies of $(Ca_{Al}'\text{-}V_O^{\cdot\cdot}\text{-}Ca_{Al}')^x$ in the bulk of $\alpha\text{-}Al_2O_3$ using the non-empirical potential (energies in eV)

	Free energy (eV)		Entropy (10^{-4}eVK^{-1})	
Temperature (K)	Harmonic	Quasi-Harmonic	Harmonic	Quasi-Harmonic
100*	92.22	92.05	0.72	0.71
100**	92.22	92.05	0.75	0.73
1000*	92.38	91.75	-3.64	-4.06
1000**	92.38	91.75	-3.64	-4.04

* 1 k-point

** 8 k-points

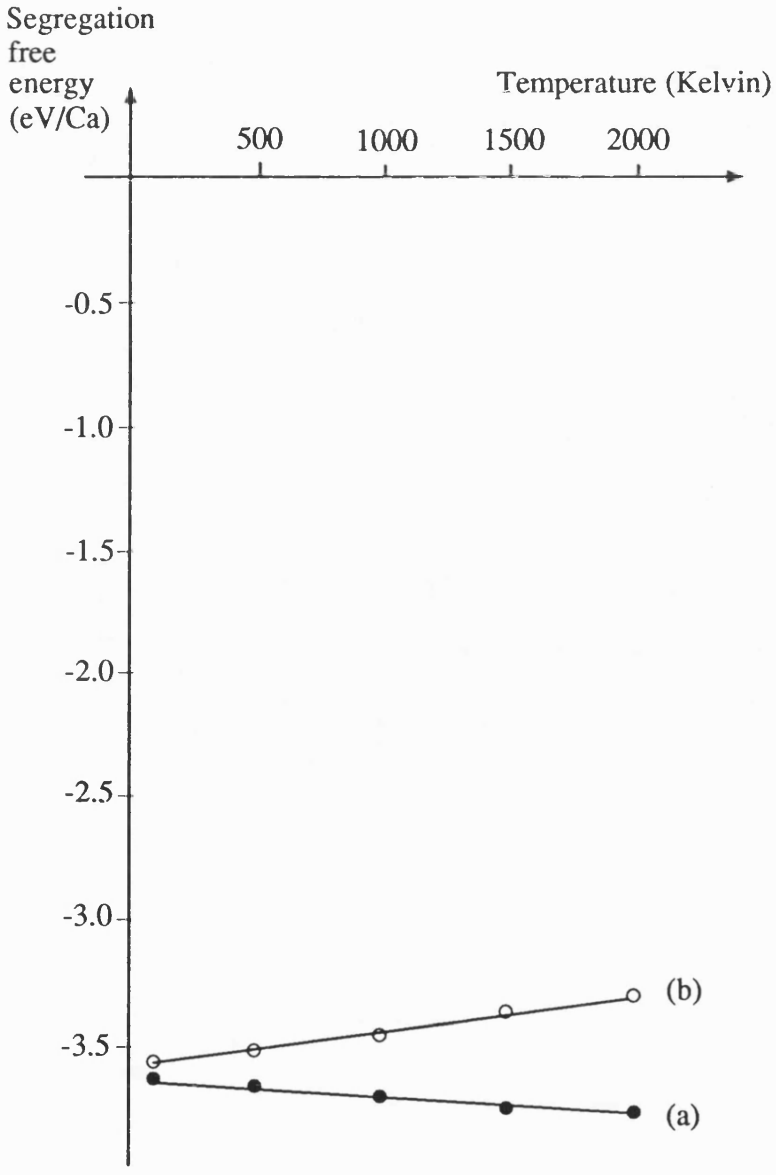

Figure 4.13: Calculated segregation free energy of (Ca_{Al}'-V_O-Ca_{Al}') against temperature using the empirical potential. (a) harmonic approximation and (b) quasi-harmonic approximation ((a) and (b) are calculated for 100% surface coverage)

segregation free energy calculated by the harmonic approximation becomes more negative with increasing temperature. This corresponds to a positive entropy of segregation, although the calculated values in table 4.10 show considerable scatter. Masri et al. (164) calculated a negative segregation entropy for Ca at the {001} surface of MgO of -2.07 x 10^{-5} eVK^{-1} at 1000 K and this difference was mainly due to the loss in bulk entropy.

The free energies of segregation, calculated using the quasi-harmonic approximation and the empirical potential, are also given in figure 4.13. The free energy of segregation decreases with temperature. This is because as the lattice expands the potential energy component of the segregation free energy becomes less exothermic. The entropy change is still positive for temperatures above 100 K but this is masked by the effect of the segregation potential energy. The segregation entropies are compared with those using the harmonic approximation in table 4.10.

As in the previous sections, the convergence of the calculations was tested by repeating the calculations with 4 (surface calculations) and 8 (bulk calculations) points in reciprocal space. These are given in table 4.10 and show the same trend as the results using one reciprocal lattice point.

The segregation free energy and the segregation entropy were also calculated from the calculations on the larger bulk slab (the unit cell of this slab contained 159 ions - $Ca_2Al_{62}O_{95}$). The segregation free energy and entropy at 1000K are -6.96 $eV(cluster)^{-1}$ and 2.33 x 10^{-4} $eVK^{-1}(cluster)^{-1}$ and compare with -6.89 $eV(cluster)^{-1}$ and 2.03 x 10^{-4} $eVK^{-1}(cluster)^{-1}$ for the $Ca_2Al_{30}O_{47}$ slab. The segregation entropy is also positive and compares favourably with the calculations on the smaller bulk slab (80 ions).

The results for the non-empirical potential for the quasi-harmonic and the harmonic approximation are given in table 4.11. They show the same trends as observed for the empirical potential: the potential segregation energy dominates the

Table 4.10: Calculated segregation entropies of $(Ca_{Al}'\text{-}V_O^{\cdot\cdot}\text{-}_{Al}')^x$ at the basal surface of $\alpha\text{-}Al_2O_3$ using the empirical potentials

	Entropy ($10^{-4}eVK^{-1}$)*		Entropy ($10^{-4}eVK^{-1}$)**	
Temperature (K)	Harmonic	Quasi-Harmonic	Harmonic	Quasi-Harmonic
100	-0.33	-0.33	-0.89	-0.88
500	1.22	1.36		
1000	0.68	2.03	1.84	2.13
1500	5.34	0.51		
2000	1.89	2.55		

Table 4.11: Calculated segregation free energies and entropies of $(Ca_{Al}'\text{-}V_O^{\cdot\cdot}\text{-}Ca_{Al}')^x$ at the basal surface of $\alpha\text{-}Al_2O_3$ using the non-empirical potentials (values quoted are per calcium)

	Free energy (eV)		Entropy ($10^{-4}eVK^{-1}$)	
Temperature (K)	Harmonic	Quasi-Harmonic	Harmonic	Quasi-Harmonic
100*	-2.24	-2.17	1.29	1.32
100**	-2.25	-2.18	1.31	1.15
1000*	-2.41	-2.13	4.53	4.88
1000**	-2.43	-2.13	4.75	4.89

* calculated using 1 k-point for surface and bulk calculation

** calculated using 4 and 8 k-points for the surface and bulk calculation respectively

free energy of segregation and that at 1000 K the segregation entropy is positive.

The result of a positive entropy is the reverse of what might be expected (177) because at the surface the relaxation of strain should be greater than in the bulk and therefore the shift in the vibrational properties should be less. Indeed, Masri et al. (164) have shown that the entropy of segregation for calcium at the {001} surface of MgO is negative. The enthalpy of segregation is also negative and this implies that the strain at the surface is lower than in the bulk. Mackrodt (147) found that the segregation enthalpy of yttrium, which has a comparable ion size to that of calcium (the ionic radii of Ca^{2+} and Y^{3+} are 1.14 and 1.04 respectively (155)), is approximately zero and therefore the strain at the surface is similar to that in the bulk. In contrast, the enthalpy of segregation of an isolated Ca^{2+} ion at the basal surface is negative (-2.57 eV and -1.00 eV for the empirical and non-empirical potentials respectively) and this implies that for aliovalent impurities the relief of strain is not the only factor influencing segregation (infact the cation site potential (178) and image charge interactions are also important (see section 2.6)). Aliovalent segregation is also complicated by the nature of the charge compensating defects and, therefore, the segregation entropy of the cluster to the basal surface need not be negative.

The segregation free energy and entropy have been calculated at constant lattice parameter. To be of use to experiment these must be converted to constant pressure quantities (179). The entropy at constant pressure is obtained from:

$$s_p = -(\partial g_p/\partial T)_p$$

and since $g_p \approx f_v$ (180), the entropy is given by the slope of the quasi-harmonic segregation plot. This is negative and is to be expected because the decrease in the potential energy as the lattice expands dominates the change in free energy. The

calculated values are -2.6 x 10^{-6} eVK^{-1} and -4.4 x 10^{-5} $eVK^{-1}$for the empirical and non-empirical potential respectively.

4.11 Summary

In this chapter, calculations on the segregation of magnesium and calcium to the prism and calcium to the basal surfaces of α-Al_2O_3 were discussed. The results for the prism surface show good agreement with available experimental data although various approximations were made. These were firstly that there are only two sites, one bulk and one surface site. Secondly, that impurity clusters need only be considered and that they segregate at essentially planar, nondefective surfaces to form ordered structures. At low coverages both these assumptions may be unrepresentative of real systems, because disordered segregation at steps, ledges and other surface irregularities (181) might well predominate. The last assumption was that the potential energy of segregation at 0 K is the major contributor to the free energy at elevated temperatures.

The segregation behaviour of calcium to the basal surface is qualitatively similar for both potentials, although the quantitative comparison is poor. When compared to available experimental data for calcium segregation at this surface, the agreement is at best inconclusive and at worst in variance to the results presented here. This difference, however, can probably be attributed to the lack of thermodynamic equilibration in the experiments and not an error in the simulations.

Atomistic simulation was extended to explicitly include lattice expansion and hence the effects of temperature in non-cubic oxides using lattice dynamics. Two potentials were used to check the reliability of the results. An important point that has emerged from these calculations is that anharmonic contributions to the free energy are important for high temperature studies on α-Al_2O_3 i.e. the mismatch between

theory and experiment can probably be accounted for because the expansion of the lattice energy is truncated to second order. Also, the results show that the major contributor to the surface and bulk impurity substitution energies is the potential energy. Thus, the assumption that the entropy contribution to these energies is small is reasonable. This is particularly important because this assumption has been implicit in all previous simulations of surface segregation in corundum structured oxides, including those at the prism surface. Indeed, it is used in the following two chapters where the pure and defect surface properties of La_2CuO_4 and Nd_2CuO_4 are discussed.

Chapter 5

The Pure Surfaces of T-La_2CuO_4 and T'-Nd_2CuO_4

5.1 Introduction

Calculations on the structures and stabilities of the surfaces of tetragonal Nd_2CuO_4 and La_2CuO_4 using the MIDAS (82) code developed by Tasker are discussed in this chapter. The potentials that were used were derived by semi-empirical methods and are described in chapter 3. Calculations on surface defect properties are discussed in chapter 6.

Stoichiometric La_2CuO_4 and Nd_2CuO_4 are antiferromagnetic semi-conductors (182). When they are doped they can be rendered p-type (11) and n-type (28,29) superconductors respectively. The superconducting current is carried by the 2-dimensional CuO_2 planes (183) in these materials. Their layer structure leads to a high degree of anisotropy in their electrical properties (184) perpendicular and parallel to the CuO_2 planes e.g. in the undoped materials the resistivity is much higher perpendicular to the CuO_2 planes than parallel to them. Interfaces which are parallel to the conduction path will thus provide a barrier to inter-granular CuO_2 plane connectivity and hence conductivity. In contrast, interfaces which cut the CuO_2 planes are required for inter-granular conductivity in polycrystalline materials. Therefore the structure and composition of these surfaces will play a decisive role in determining intergranular weak links and surface conductivity (185).

The {001} and {100} surfaces in both materials are considered first. These are of particular importance because they are parallel and perpendicular to the CuO_2 planes. Then higher index surfaces are considered because boundary critical currents are controlled by the orientation of the CuO_2 planes (186) and small crystallite

morphologies may not be dominated by the closest packed, and hence lowest index, surfaces (187).

5.2 The Crystal Structures of La_2CuO_4 and Nd_2CuO_4

5.2.1 La_2CuO_4

In the rare earth series RE_2CuO_4 (RE=La, Pr, Nd, Sm, Eu, Gd) copper is only octahedrally coordinated (188) to oxygen in lanthanum cuprate. Above 530 K (189) it has the K_2NiF_4 or T-structure with I4/mmm symmetry, shown in figure 5.1. This is a layered perovskite structure where $(CuO_2)^{2-}$ sheets alternate with two rock salt $(LaO)^+$ layers. Copper is octahedrally coordinated to six oxygens and lanthanum is nine-coordinate. The CuO bonds are approximately 25% longer along the c-axis which is due, in part, to Jahn-Teller effects associated with the d^9 electronic configuration of copper II. However, this distortion must also be a consequence of the layer structure because the NiO bonds in La_2NiO_4, where there is no Jahn-Teller effect, are also longer in the c-direction by approximately 11% (190). Below 530 K the CuO_6 octahedra in La_2CuO_4 tilt about the c-axis and this leads to a structure with orthorhombic symmetry, Cmca (191). The driving force for this distortion is due to the relief of unfavourable anti-bonding π^*-interactions in the CuO_2 planes (192). Allan and Mackrodt (193) have demonstrated that the structural and defect properties of the tetragonal and orthorhombic polymorphs are comparable. Thus, in the work described in this thesis, only calculations on the tetragonal structure were performed and compared with an analogous study of Nd_2CuO_4. This is structurally similar to La_2CuO_4 and is now described.

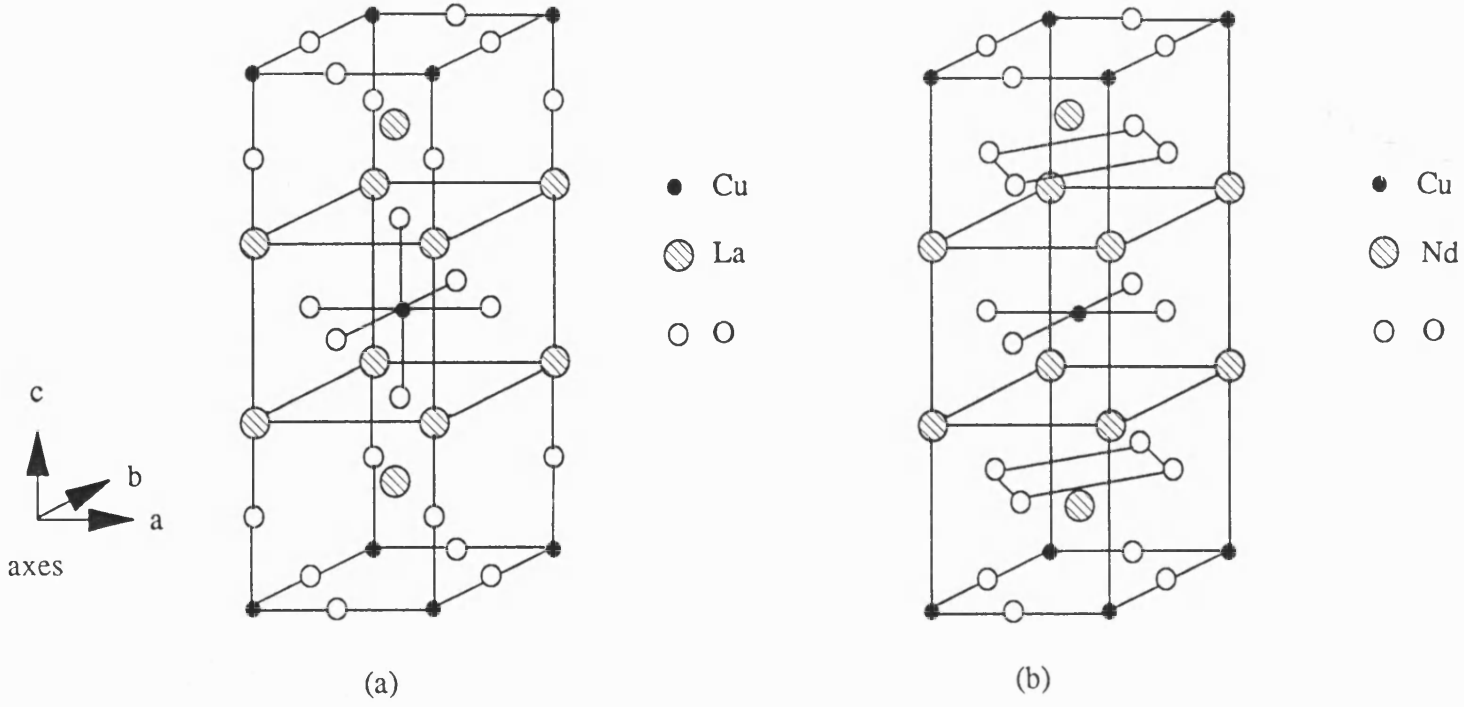

Figure 5.1: Comparison of the crystal structures of (a) La_2CuO_4 and (b) Nd_2CuO_4

5.2.2 Nd_2CuO_4

Originally the rare earth cuprates of Pr, Nd, Sm, Eu and Gd were also thought to possess the K_2NiF_4 structure (194). However, in 1975, Mueller-Buschbaum and Wollschlaeger (195) examined the structure of Nd_2CuO_4 using X-ray crystallography and found that copper is not octahedrally coordinated, but is in a square planar configuration with four oxygens. The $(CuO_2)^{2-}$ sheets are separated by fluorite structured $(Nd_2O_2)^{2-}$ layers and neodymium, which is smaller than lanthanum, is eight-coordinate. This structure has since become known as the Nd_2CuO_4 or T'-structure which also possesses tetragonal (I4/mmm) symmetry. This structure is compared to the T-structure in figure 5.1. In contrast to La_2CuO_4, no phase change from tetragonal to orthorhombic symmetry is observed. This is because the in-plane CuO bond lengths are much greater in the Nd_2CuO_4 structures (for Nd_2CuO_4 1.98 Å as compared to 1.89 Å in La_2CuO_4). Consequently, the unfavourable π^*-antibonding interactions are much smaller and the structure is determined by ionic considerations (192).

In the next section the surface methodology is described. This is required in order to classify the surfaces that are considered in the following sections.

5.3 Surface Methodology

The stable surfaces of ionic crystals will be those at which the Madelung sums converge with increasing crystal size. This occurs when the crystal is electrically neutral and also when there is no net dipole moment perpendicular to the surface (196,197). This can be seen by considering the expressions given in Chapter 2 (section 2.5) that are used to calculate the Madelung sums. They give the electrostatic potential due to a layer of charges q at a perpendicular distance z. A sum over each

sublattice on each plane gives the total electrostatic potential. For distances z greater than a few interionic separations the contribution from a planar sublattice reduces to the form:

$$V(z) = (2\pi/A)qz \qquad (5.1)$$

where A is the area of the unit cell in the plane. This expression is identical to the potential due to an infinite charged plane of charge density:

$$\rho = q/A \qquad (5.2)$$

The field due to the charged plane, E is then given by:

$$E = 2\pi(q/A) \qquad (5.3)$$

Since equations 5.1 and 5.3 do not diminish with increasing z the potential will be infinite at infinite distances from an individual plane. However, for a crystal which is constructed as a neutral block the infinities cancel and the potential becomes constant at large distances. In fact, it becomes zero in all cases except where there is a dipole moment perpendicular to the surface (196,197).

These points are illustrated in figures 5.2(a)-(c) by considering three different stacking sequences: type 1; type 2 and type 3 after Tasker (196). In figure 5.2(a), which represents type 1 surfaces, each plane has an overall charge of zero since it consists of both anions and cations in stoichiometric ratio. The potential (5.1) cancels on each plane because the contributions of the sublattices are equal and opposite and thus addition of extra planes on the surface of the crystal make no contribution to the energy in the bulk crystal. Consequently, the lattice sums required for the Madelung

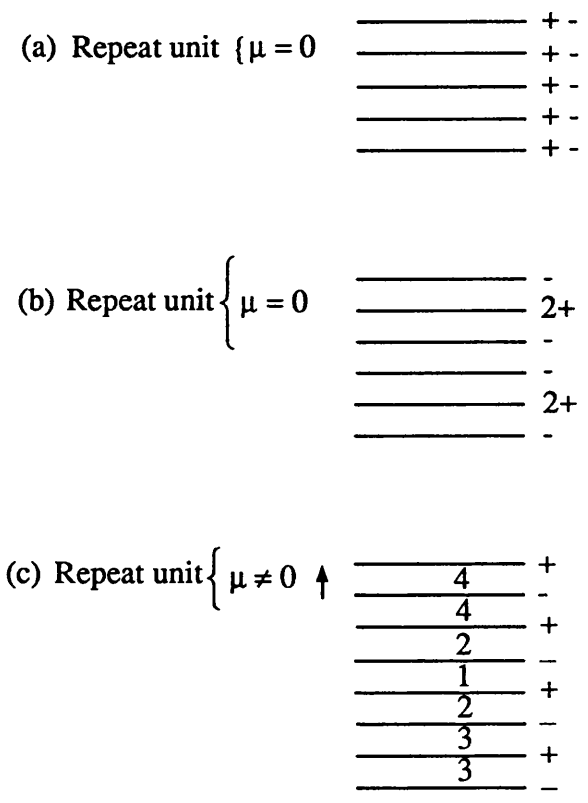

Figure 5.2: The three different stacking sequences of charged planes: (a) type 1; (b) type 2; (c) type 3

energy of any ion site to converge need include only a few planes either side of that site. An example of such a stacking sequence is the {001} surface of MgO.

Figure 5.2(b) shows a symmetric stacking sequence of charged planes which is referred to as a type 2 surface. The repeat unit consists of three planes in symmetrical configuration and hence there is no dipole moment perpendicular to the surface. Each plane contributes a term to the potential sum, but the sum over the three plane repeat unit is zero because of self-cancellation. Addition of extra neutral repeats at the surface of the crystal does not affect the ions in the bulk and again the Madelung sums for the potential at any ion site are rapidly convergent. An example of such a surface is the {111} of CaF_2.

The last surface that is considered is represented schematically in figure 5.2(c) and is denoted a type 3 surface. It consists of alternately charged planes and this stacking sequence produces a dipole moment perpendicular to the surface. Addition of an extra neutral repeat unit of two planes on the surface of the crystal will affect the energy of ions an infinite distance below the surface. Consequently the Madelung sum cannot be truncated and must include contributions from every plane out to the surface. This summation diverges with increasing crystal size and thus the surface energy is infinite.

The electric field at an ion site will also not cancel when the crystal terminates at a type 3 surface, but reaches a constant value at infinite distances into the crystal. This can be seen by considering an ion on plane 1 of figure 5.2(c). The field from the planes labelled 2 cancels by symmetry, as does that due to the dipole layers 3 and 4. Assuming that the contribution to the electric field from planes in the bulk of the crystal do likewise, the field due to the surface plane is left.

The instability in the stacking sequence at a type 3 surface due to a perpendicular dipole moment can be removed by surface reconstruction or the adsorption of foreign atoms (198). Kummer and Yao (199) have demonstrated that the

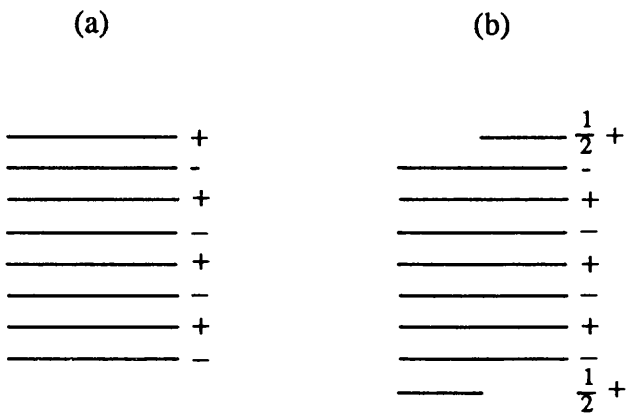

Figure 5.3: (a) Unstable type 3 dipolar surface
(b) Instability removed by surface reconstruction.
Note that the stacking sequence in b is type 2.

energy of a finite crystal will be lowered if charge is transferred from the upper to the lower face (figure 5.3) i.e. the surface is reconstructed and the stacking sequence becomes type 2. Using the electrostatic argument given above, the electric field at the centre planes is zero and the surface energy will thus be finite for any block size. Thus, the polar type 3 surfaces cannot be simple bulk terminations and will reconstruct. Examples of type 3 surfaces that have been observed experimentally are impurity stabilised NiO {111} (200) and $SrTiO_3$ {111} (201).

The lowest index surfaces are now classified as type 1, 2 or 3. After discussing their relative stabilities, the higher index surfaces of both materials are described.

5.4 The {100} and {001} Surfaces of La_2CuO_4 and Nd_2CuO_4

As mentioned above, the {100} and {001} surfaces are perpendicular and parallel to the CuO_2 planes in La_2CuO_4 and Nd_2CuO_4. The resistivity of these materials is highly anisotropic (184) and it is much lower in the ab plane (see figure 5.1) because of the perovskite layer structure. Therefore {001} surfaces, which are parallel to the ab plane, will have a detrimental effect on the connectivity of the CuO_2 planes and consequently inter-granular conduction in these materials.

The {001} surface of La_2CuO_4 is a type 2 surface and terminates in a rumpled layer of LaO (figure 5.4). In contrast, the {001} surface of Nd_2CuO_4 is a polar type 3 surface and must, therefore, be stabilised by reconstruction. The stacking sequence of Nd_2CuO_4 is shown in figure 5.5(a) along with the two reconstructions which lead to a surface terminating in oxygen (figure 5.5(b)) and a surface terminating in copper-oxygen (figure 5.5(c)). The {100} surfaces are both type 1 surfaces with neutral planes of La_2CuO_4 or Nd_2CuO_4.

In the next two sections, calculations of the stabilities of the low index

Figure 5.4: The Stacking Sequence
at the {001} surface of La_2CuO_4

La - O - La - O

O - Cu - O

La - O - La - O

Figure 5.5a: The Stacking Sequence
at the {001} surface of Nd_2CuO_4

O - O - O - O

Nd - Nd

O - Cu - O - O - Cu - O

Nd - Nd

Figure 5.5b: Reconstructed
{001} Nd_2CuO_4 oxygen surface

O - O

Nd - Nd

O - Cu - O - O - Cu - O

Nd - Nd

O - O

Figure 5.5c: Reconstructed
{001} Nd_2CuO_4 copper
oxygen surface

O - Cu - O

Nd - Nd

O - O - O - O

Nd - Nd

O - Cu - O

surfaces of each material are discussed.

5.4.1 La_2CuO_4

The calculated energies for the unrelaxed and relaxed surfaces are given in table 5.1. In the absence of relaxation, the {001} surface terminating in a rumpled lanthanum-oxygen layer will dominate the equilibrium crystal morphology in preference to surfaces perpendicular to the CuO_2 planes. However, extensive relaxation of the {100} surface, unlike the {001} surface, leads to approximately equi-energetic surfaces, which has important implications for the equilibrium crystal morphology and consequently inter-granular connectivity of the CuO_2 planes in this material. The crystal morphology is discussed further in section 5.6.

The extent of the relaxations at the {100} surface is shown in figures 5.6. The principal features are atomic displacements of up to 0.4 Å perpendicular to the surface and 0.2 Å within the surface planes and also displacements of up to 0.06 Å six layers (approximately 10 Å) into the bulk. Thus, the extent of the {100} surface relaxation into the bulk is comparable to the coherence length in the superconducting ab plane.

The {001} surfaces terminating in a copper oxygen plane must reconstruct or adsorb charge because they are inherently dipolar type 3 surfaces. After reconstruction by halving the density of oxygen and copper at the surface (i.e. removing the dipole perpendicular to the surface) the unrelaxed and relaxed energies can be calculated and these are compared with the {001} lanthanum-oxygen termination in Table 5.1. The non-dipolar lanthanum-oxygen surface is more stable than that of a dipolar copper-oxygen by 0.4 Jm^{-2}. This result contradicts the conclusions of Brookes et al. (202) who used LEED and AES to investigate the structure of this surface. They found that on annealing La_2CuO_4 single crystals, the

Table 5.1: Unrelaxed and relaxed surface energies of the {100} and {001} surfaces of La_2CuO_4 and surfaces of La_2CuO_4 and Nd_2CuO_4 (all energies in Jm^{-2})

	Unrelaxed	Relaxed
La_2CuO_4		
{100}	4.5	1.3
{001}OLa	1.7	1.2
{001}OCu	11.2	1.7
Nd_2CuO_4		
{100}	2.7	1.7
{001}O	6.5	3.6
{001}OCu	5.6	1.3

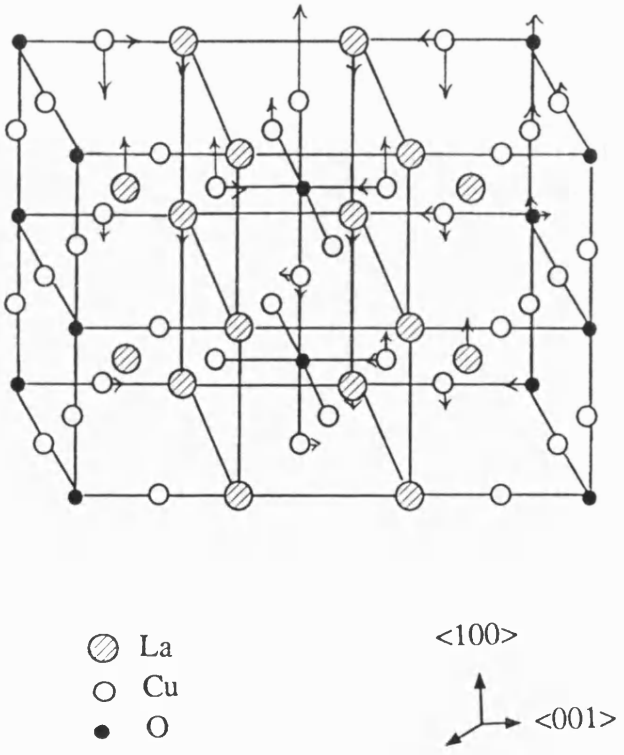

Figure 5.6: Sketch of the principal relaxations at the {100} surface of La_2CuO_4

diffraction pattern changed from (1x1) to (1x8) with a corresponding increase in the Auger Cu/La ratio. This they attributed to the preferential formation of CuO_2 rather than LaO planes with ordered oxygen vacancies at the {001} surface. A transformation of this type, however, may also correspond to the formation of surface steps or be related to defect segregation: this can only be confirmed by further experimental investigation.

5.4.2 Nd_2CuO_4

The structure of T'-Nd_2CuO_4 is similar to that of T-La_2CuO_4 except that copper is coordinated to four planar oxygens and separated by three fluorite structured layers of neodymium and oxygen. (see Figure 5.1). In common with La_2CuO_4, the {100} of Nd_2CuO_4 is a type 1 surface. However, the {001} stacking sequence is dipolar but can be reconstructed so that the surface terminates at an oxygen or copper-oxygen surface (figure 5.5). The calculated unrelaxed and relaxed energies of these surfaces are compared with those of La_2CuO_4 in table 5.1. The unrelaxed {100} surface of Nd_2CuO_4 is more stable than both {001} surfaces. On relaxation this order changes and the {001} surface terminating in a copper-oxygen plane is more stable than the {100} by 0.4 Jm^{-2}. Thus the equilibrium crystal morphology will be dominated by {001} copper-oxygen surfaces. This result is unexpected because polar type 3 surfaces are usually assumed to be less stable than corresponding type 1 and type 2 surfaces and are often ignored. Type 3 surfaces have been observed experimentally in both binary (200) and ternary oxides (201), however, and there appears to be a connection between their stability and the band gap of the material in question. Also, recent theoretical work on the surfaces of spinels by Davies (203) supports the finding that reconstructed dipolar surfaces can have low energies.

A schematic representation of the relaxations at these low index surfaces of

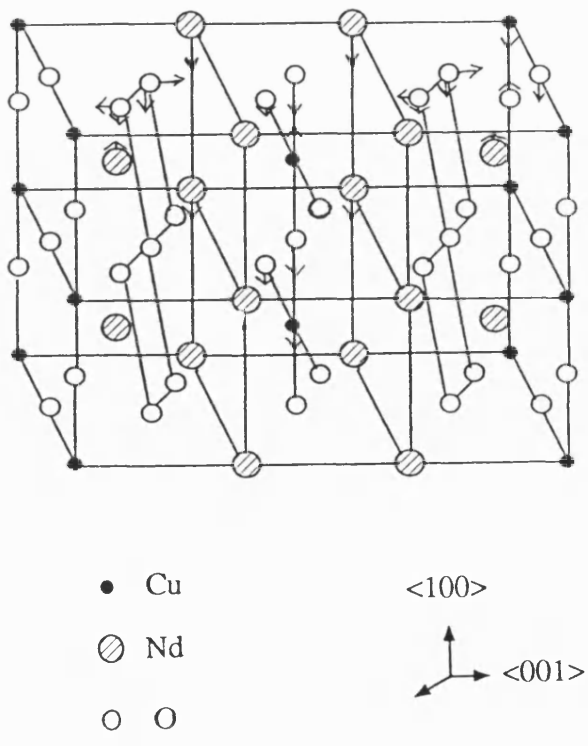

Figure 5.7: Sketch of the principal relaxations at the {100} surface of Nd_2CuO_4

Nd_2CuO_4 is given in figures 5.7 and 5.8. All the atoms at the surface of the {100} relax inwards (figure 5.7), but by different amounts. The relaxations of neodymium and in-plane oxygens ions are greatest perpendicular to the surface and are 0.12 Å. Ionic relaxation within the surface plane is less than 0.08 Å. Relaxation is also observed below the surface, but by plane 3 (about 4Å below the surface) is less than 0.05 Å. At the {001} surface terminating at half an oxygen plane the relaxations are larger (figure 5.8(a)). The surface oxygen ions move 0.22 Å perpendicular to the surface while the first CuO_2 plane below the surface (about 3 Å) rumples appreciably i.e. the copper ions move out by 0.22 Å whereas half the oxygen ions move out by 0.43 Å and the other half relax towards the bulk by 0.19 Å. Relaxation parallel to the surface is much smaller and less than 0.01 Å. In the second CuO_2 plane below the surface (about 9 Å) the ions relax by less than 0.01 Å. At the {001} surface of Nd_2CuO_4 terminating in half a CuO_2 plane (figure 5.8(b)) the copper ions move out of the surface by 0.39 Å while the oxygens move in by different amounts (0.36 Å and 0.07 Å). Lateral copper movement is also large (0.4 Å). In the second CuO_2 plane below the surface the copper ions move by less than 0.01 Å while the maximum displacement of oxygen ions is 0.04 Å perpendicular to the surface.

Comparing the two cuprates, which have different structures, the relative stabilities of the unrelaxed surface energies are different. On relaxation, the most energetically favourable surfaces of La_2CuO_4 and Nd_2CuO_4 are the {001} planes which have similar stabilities. However they terminate at different surface planes and this is due to differences in surface structure of the two cuprates and the large relaxation (4.3 Jm^{-2}) of the {001} copper-oxygen surface of Nd_2CuO_4. The {100} surfaces terminate in a stoichiometric repeat unit but the arrangement of the atoms in the plane is different in the two structures. Relaxation is much less dramatic in the T'-structure at the {100} surface, which is perpendicular to the CuO_2 planes and will

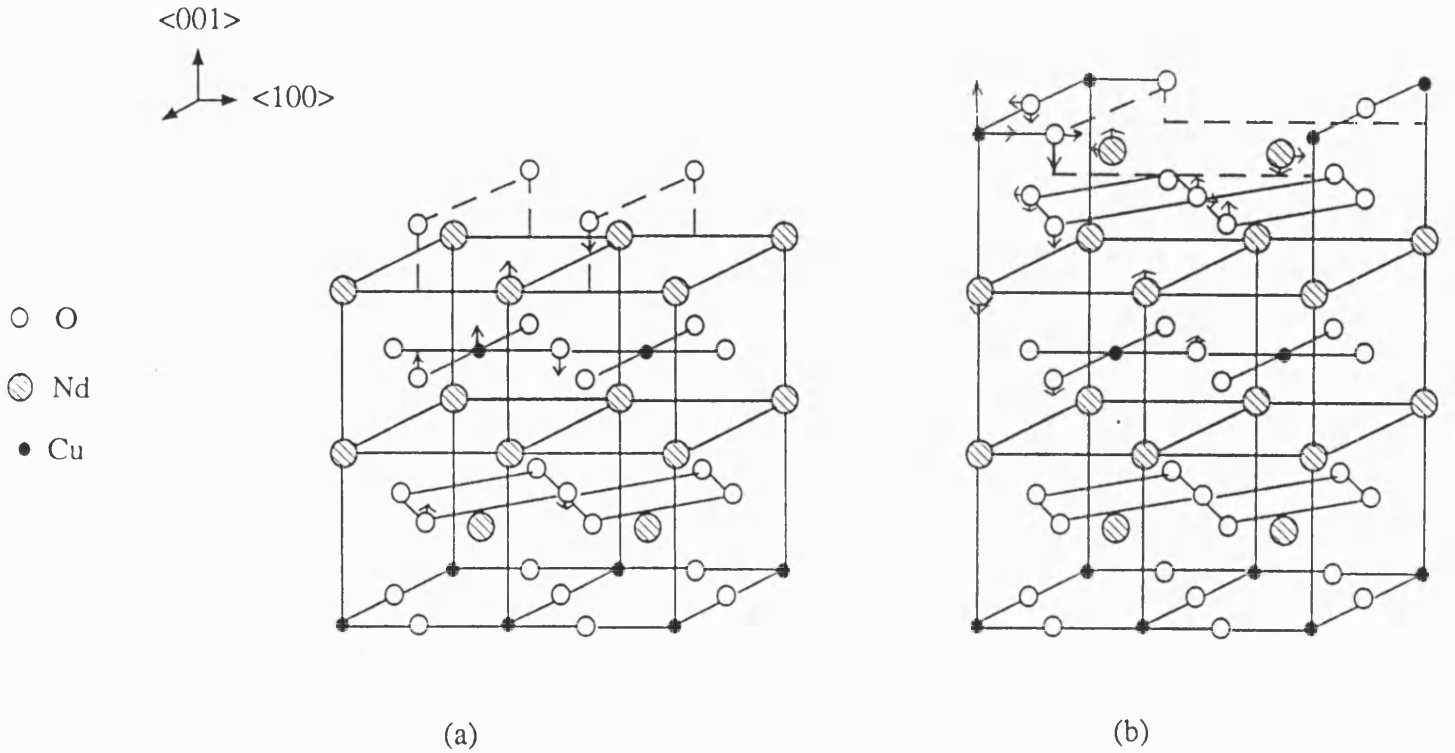

Figure 5.8: Sketches of the principal relaxations at the {001} surfaces of Nd_2CuO_4

(a) the O termination (b) the CuO_2 termination

thus be less detrimental to intergranular conductivity.

Experimentally, $Nd_{2-x}Ce_xCuO_4$ (204), isostructural Gd_2CuO_4 (205) and La_2CuO_4 (206) form plate-like single crystals with their short dimension parallel to the c-axis. The agreement with the work described here, however, which is particularly good for the T'-structure, may be fortuitous because no account of the kinetics of crystal growth is included in the calculations. Kinetics influence crystal morphologies as exemplified by Karalewski et al. (207), who have shown that by varying the starting flux composition and the growth conditions either cubic or plate-like crystals of a Y-Ba-Cu-O phase are obtained experimentally. In addition, two other factors need to be considered. Firstly, segregation will also influence the relative stabilities of surfaces (173) and impurities are often incorporated in these crystals unintentionally e.g. Pb (208) from the PbO flux growth method. Further discussion on defect segregation is given in chapter 6. The second factor that has not been addressed is that there may be other stable surfaces which contribute to the equilibrium crystal habit and a discussion of these is now given.

5.5 Higher Index Surfaces of La_2CuO_4 and Nd_2CuO_4

Previous calculations on high index surfaces in ceramics have been confined to those with the rocksalt structure. Tsang and Falicov (91) showed that relaxation at the {1,0,12} surface of NaCl is much greater than the relaxation of the corresponding surface of solid argon. This they attributed to the polarisability of the ionic material. However, no comparison was made with other stepped surfaces. Tasker and Duffy (209) made a thorough study of the relative stabilities of periodic monatomic steps on the {001} and {101} surfaces of MgO and NiO. They found that there were repulsive interactions between steps but these were of short range. Thus at low step densities

the step energy has a linear dependence on Θ, the angle of inclination of the surface to the {100}. However, for large Θ the step interaction energies are complicated.

The structures of the higher order surfaces of La_2CuO_4 and Nd_2CuO_4 that have been investigated are more complicated than the stepped surfaces of the rocksalt ceramics. They can however be classified as {n10} and {10m) surfaces and are now described.

5.5.1 {n10} Surfaces

The {n10} series of the T- and T'-structures form steps between the {100} and {010} surfaces which are symmetry related planes. They may be subdivided into odd and even values of n. For n=even they are type 1 surfaces with monatomic steps composed of oxygen and La_2CuO_2 or Nd_2Cu on terraces of n atoms of {100}. This series is thus comparable to the {10n} rocksalt structured surfaces discussed in the previous section. For n=odd they are intrinsically unstable type 3 surfaces and will reconstruct or adsorb foreign atoms - this is also the same for $SrTiO_3$. The number of atoms in a terrace is odd for n=odd and even for n=even. It was only possible to compute relaxed energies for the {110} and {210} surfaces because for higher order surfaces the required size of region II necessary for convergence of the result became computationally prohibitive. The structures of the two surfaces of both materials investigated are given in appendix 5 (figures A5.1 and A5.2).

5.5.2 {10m} Surfaces

The {10m} surfaces can also be divided into two series with m=odd and m=even. For each m=even surface there is only one termination which gives a

non-polar type 2 surface. The Miller indices of the 'even' surfaces which were investigated are the {102}, {104} and {106} and their structures are given in appendix 5 (figures A5.3, A5.4, A5.5, A5.6). These surfaces are not as simple as the {n10} (n=even) surfaces for two reasons. Firstly, the planes in the stacking sequence are not stoichiometric repeat units of La_2CuO_4 or Nd_2CuO_4 and secondly, the number of atoms in a terrace and in a step is not constant for a given cleaved surface. The major consequence of these differences is that there are several possible arrangements of atoms at any given surface (with a particular Miller index) for which surface energies can be calculated. The configuration with the lowest energy represents the thermodynamically stable surface and consequently that which is important for the equilibrium crystal morphology. The configurations with higher energies are metastable and their formation will be controlled by the kinetics of crystal growth. To find the thermodynamically stable configuration of a given surface (with a particular Miller index) the unrelaxed energies of the different possible atomic arrangements were calculated and the one with the lowest energy was taken as the starting configuration for the relaxation. Although unrelaxed energies between surfaces with *different* Miller indices cannot be relied on to give the relaxed order, this proved to be a reliable approximation for different configurations at the same Miller indexed surface. (Note that the most stable configuration of each surface is given in figures A5.3 to A5.6).

The m=odd surfaces in the {10m} series of these materials are not dipolar in contrast to the odd {n10} series. These surfaces do, however, have two possible terminations for which the stoichiometric repeat unit is non-polar. The Miller indices of the surfaces, with corresponding terminations are:

1. {101} CuO and O for both materials
2. {103} CuO and La or CuO and Nd

3. {105} CuO and O or CuO and Nd

Their structures are given in Appendix 5 (figures A5.8 to A5.13) and, as before, these represent surfaces for which the unrelaxed energies are lowest. These surfaces are type 2 rather than type 1 surfaces because only one of the planes, the CuO plane, is uncharged. Surfaces where there are two possible non-polar terminations have also been observed in $SrTiO_3$ (210) which possesses the perovskite structure. Their surfaces can be divided into an odd and even {n10} series. For n=odd the repeat unit of the stack is dipolar, whereas when n=even there are two possible terminations: SrO and TiO_2, and these are type 1 surfaces.

5.5.3 Results

5.5.3.1 La_2CuO_4

The unrelaxed (U_u) and relaxed (U_r) energies of the {101}, {103} and {105} terminations are given in table 5.2. The energies U_u and U_r are calculated from the equation:

$$U = 1/2\{(\text{block calculation}) - (\text{surface calculation})\}/\text{Area} \qquad (5.4)$$

By themselves these energies do not correspond to the energy required to cleave the crystal because they only account for the formation of one of the surfaces e.g. for the {101} surface they give the energy required to create either a CuO or an O surface. However, the average of the two energies of a surface with a particular Miller index will give the energy required to cleave the crystal exposing both surfaces. Note that this definition (equation 5.4) does not include step energies and step interaction

Table 5.2: Unrelaxed and relaxed energies (Jm^{-2}) of the {10m} m=odd surfaces of La_2CuO_4

Terminating Plane	Unrelaxed Energy	Relaxed Energy	Average* Energy
{101}O	5.8	1.9	1.75
{101}OCu	5.8	1.6	
{103}La	6.4	1.6	1.55
{103}OCu	6.4	1.5	
{105}O	12.4	2.2	2.2
{105}OCu	12.4	2.2	

*Energy required to cleave crystal exposing both terminations

energies between different terminations and thus it is presupposed that the step surface density is small.

Prior to relaxation, the energies of different terminations of a surface with a given Miller index are equal. The unrelaxed order of stabilities between the different surfaces is:

{101} > {103} > {105}

Thus with increasing m, the unrelaxed energies for cleaving the crystal increase. On minimisation the extent of relaxation is different at different surfaces. For example, the reduction in the energy required to cleave the crystal at the {103} surface is 4.85 Jm^{-2} or 76% whereas that at the {101} is reduced by 4.05 Jm^{-2} or 70%. The differences in the degree of relaxation leads to a change in the relative order of stability to:

{103} > {101} > {105}

At each surface the different terminations relax by different amounts. The OCu termination is favoured over O at the relaxed {101} surface. At the {103} surface relaxation is more pronounced at the OCu rather than the La termination. At the {105} surface, both the OCu and the O terminations relax by the same amount. Differences in the relaxation at the {001} surfaces of this material were also seen in section 5.4.1 (although the surfaces were reconstructed and their unrelaxed energies were also different). Mackrodt (211) also found that the relaxation of TiO_2 and SrO {001} surfaces in $SrTiO_3$ led to different degrees of relaxation; the TiO_2 surface being more stable by 0.2 Jm^{-2}.

The unrelaxed and relaxed energies at the m=even {10m} surfaces are given

Table 5.3: Unrelaxed and relaxed energies (Jm^{-2})
of the {10n} n=even surfaces of La_2CuO_4

Terminating Plane	Unrelaxed Energy	Relaxed Energy
{102}	4.7	1.3
{104}	5.8	1.5
{106}	8.9	1.7
{102}*	10.7	2.0
{104}*	9.5	2.0
{106}*	7.2	unstable

* surfaces with steps three ions high
(see Appendix 5 A5.14 and A5.15)

Table 5.4: Unrelaxed and relaxed energies (Jm^{-2})
of the {100}, {110} and {210} surfaces of La_2CuO_4

Miller index	Unrelaxed Energy	Relaxed Energy
{100}	4.5	1.3
{110}	3.3	1.6
{210}	5.1	1.6

in table 5.3. In each case a number of different surface geometries were investigated and those with the lowest relaxed energy are given. For comparison, the calculated energies of reconstructed surfaces that are three ions high and terraces m atoms long are also included in the table. The structures of these additional surfaces are given in Appendix 5 (figures A5.14 and A5.15). The ordering of these surfaces before relaxation is:

{102} > {104} > {106}

As with the odd series, the stability decreases with increasing m. On relaxation the order does not change, although the degree of relaxation is different in each case. The stability cannot decrease indefinitely with increasing n because the surface will start to resemble the {001} surface. The unrelaxed energies are lower than the unrelaxed energies of the surfaces containing steps that have been reconstructed. For the relaxed reconstructed surfaces, only the {102} and {104} surfaces are stable but are of higher energy than the cleaved surfaces. It is concluded that steps are preferentially less than three ions high.

The order of stabilities before relaxation of the {10m} for both m=odd and m=even are:

{001} > {100} > {102} > {101} = {104} > {103} > {106} > {105}

and after relaxation are:

{001} > {100} = {102} > {104} > {103} > {106} > {101} > {105}

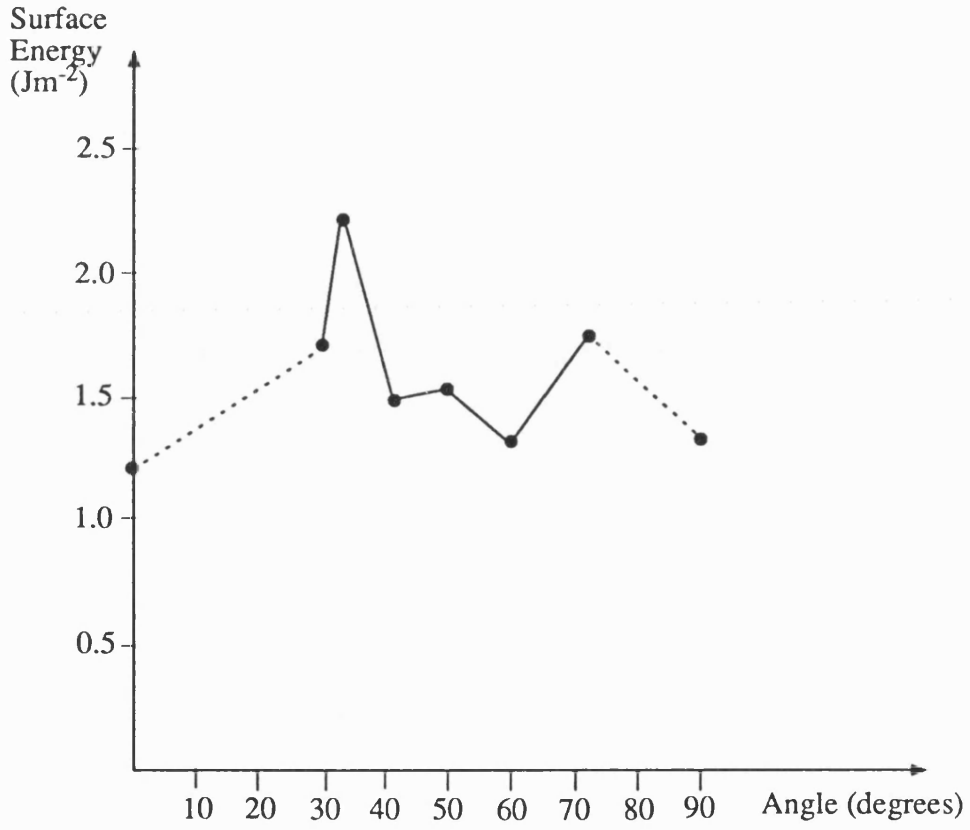

Figure 5.9: Plot of the surface energy of the {10m} (m=0,1,2,3,4,5,6) planes against misorientation angle with the {001} surface of La_2CuO_4

The surface energies are plotted against the misorientation angle Θ with the basal {001} surface in figure 5.9. In contrast to this series, in rocksalt structured oxides there is no relationship between Θ and surface energy. This reflects the more complex surface structures in these ternary oxide surfaces. At much smaller misorientation angles (much larger terrace sizes) a relationship comparable to the rocksalt series might arise. However, it is not possible to investigate this further because the required calculations are both too computer memory and computer time intensive.

The unrelaxed and relaxed energies of the {110} and {210} surfaces have also been calculated. These are given in table 5.4 and compared to the {100} surface. These surfaces represent the first two members of the {n10} surfaces. When n=1 the surface is dipolar and was stabilised by halving the density of oxygen in the surface plane. The unrelaxed energies of these two surfaces are much greater than the relaxed ones. The {110} and {210} relaxed energies are the same but greater than the {100}.

5.5.3.2 Nd_2CuO_4

In this section the structures and relative stabilities of these surfaces of Nd_2CuO_4 are discussed. They also fall into the same series types. Thus when comparing the two structures only the {001} surfaces have different types (type 2 in La_2CuO_4 and type 3 Nd_2CuO_4). The unrelaxed and relaxed energies of these surfaces are given in tables 5.5 to 5.7. The unrelaxed order of the {10m} where m=odd surfaces is (from table 5.5):

{105} > {101} > {103}

On relaxation, the {101} O and OCu surfaces relax by the same amount. In contrast, relaxation at the different terminations of the {103} and {105} are not the same. At

Table 5.5: Unrelaxed and relaxed energies (Jm^{-2}) of the the {10m} m=odd surfaces of Nd_2CuO_4

Terminating Plane	Unrelaxed Energy	Relaxed Energy	Average* Energy
{101}O	6.7	1.3	1.35
{101}OCu	6.7	1.4	
{103}Nd	8.9	2.6	2.0
{103}OCu	8.9	1.4	
{105}Nd	4.3	1.6	1.35
{105}OCu	4.3	1.1	

*Energy required to cleave crystal exposing both surfaces

the {103} the difference is 1.2 Jm^{-2} and 0.5 Jm^{-2} at the {105}. However for stoichiometric crystals, the area of each termination must be the same, as discussed in section 5.5.3.1. The order of stabilities (based on the energy to cleave the crystal) after relaxation is:

{105} = {101} > {103}

and hence the extent of relaxation at the {101} (5.35 Jm^{-2} (79%)) is greater than at the {105} (2.1 Jm^{-2} or 49%).

The second set of surfaces that are considered are the {10m} series with m=even. As with La_2CuO_4 only one termination leads to a non-dipolar stacking sequence perpendicular to the surface. The unrelaxed and relaxed energies of these are given in table 5.6. The unrelaxed order is:

{106} > {102} > {104}

and on relaxation becomes

{106} = {102} > {104}

Thus again, the different surfaces relax by different amounts. Combining the two {10m} series and the {100} and {001} surfaces the unrelaxed order is:

{100} > {105} > {106} > {001}OCu > {102} > {101} > {104} > {103}

and the relaxed order is:

Table 5.6: Unrelaxed and relaxed energies (Jm^{-2})
of the {10m} m=even surfaces of Nd_2CuO_4

Terminating Plane	Unrelaxed Energy	Relaxed Energy
{102}	6.0	1.7
{104}	8.5	2.3
{106}	5.3	1.7

Table 5.7: Unrelaxed and relaxed energies (Jm^{-2})
of the {100}, {110} and {210} surfaces of Nd_2CuO_4

Miller Index	Unrelaxed Energy	Relaxed Energy
{100}	2.7	1.7
{110}	6.3	2.9
{210}	9.8	2.3

{001}OCu ≈ {101} = {105} > {100} > {102} = {106} > {103} > {104}

The relaxed energies are also plotted in figure 5.10 against misorientation angle Θ with the basal {001} surface. The lack of a trend in this figure demonstrates that in non-cubic structures, as with La_2CuO_4 the relationship between orientation angle and surface energy is much more complicated than for cubic NiO and MgO.

The unrelaxed and relaxed energies of the {110} and {210} are given in table 5.7 and compared to those of the {100}. The {110} surface is a type 3 surface and can be stabilised by halving the density of oxygen ions in the surface plane. In contrast the {210} surface is a type 2 surface. The order of stability before relaxation is:

{100} > {110} > {210}

and after relaxation is:

{100} > {210} > {110}

Thus the {110} surface of Nd_2CuO_4, which has a higher density of steps, is least stable after relaxation, in contrast to La_2CuO_4.

5.5.3.3 Comparison of the Two Materials

Four important points, which are general features of surface relaxation, emerge from these results. Firstly, energies of relaxed surfaces are much lower than those of unrelaxed surfaces. Secondly, relaxation energies vary from plane to plane. Thirdly, the relative stabilities of surfaces are different before and after relaxation. Finally, lattice relaxation reduces the energy differences between the various surfaces.

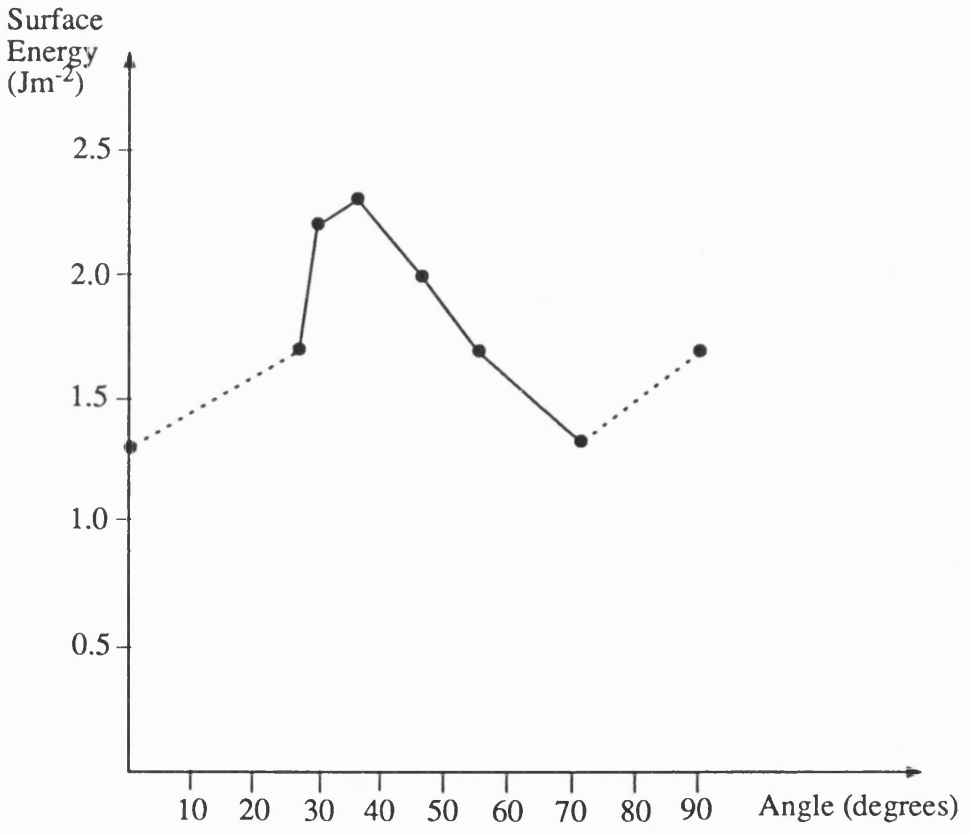

Figure 5.10: Plot of the surface energy of the {10m} (m=0,1,2,3,4,5,6) planes against misorientation angle with the {001} surface of Nd_2CuO_4

There are a number of differences between the surfaces of La_2CuO_4 and Nd_2CuO_4. In contrast to the {001} surfaces where the types of stacking sequence are different the other surfaces with a given Miller index have the same type. However, the intrinsic structures are different. Thus the unrelaxed and relaxed surface energies are different as is the order of surface stabilities. This implies that the structures will also have different equilibrium morphologies, which are now discussed.

5.6 Equilibrium Morphologies of La_2CuO_4 and Nd_2CuO_4

Gibbs (212) first proposed that the equilibrium morphology of a crystal will be that for which the total surface energy is a minimum for a given volume i.e.

$$\gamma_{crys} = \Sigma (\gamma_i A_i) = \text{minimum at constant volume} \qquad (5.5)$$

where γ_i and A_i are the surface energy and area of the i^{th} crystallographic face respectively. In 1901 Wulff (213) suggested further that the shape defined by equation 5.5 would be such that h_i, the face normal vector from a point within the crystal would be proportional to γ_i or:

$$h_i = \lambda \gamma_i \qquad (5.6)$$

where λ is a constant that depends on the absolute size of the crystal. This theorem is strictly only applicable to crystals grown infinitely slowly i.e. at equilibrium, which of course is not practical. Therefore, the theorem is said to be true for crystals in which rearrangement of the crystal is possible at all stages during growth due to the short distances over which matter has to travel.

Using this theorem, the crystal morphologies of La_2CuO_4 and Nd_2CuO_4 before and after relaxation are shown in figures 5.11 and 5.12 assuming that the {001} and {100} surfaces are important. Before relaxation, the equilibrium morphology of La_2CuO_4 is dominated by the {001} surface parallel to the CuO_2 planes. In contrast the area of the {001} in Nd_2CuO_4 is much smaller than that of the {100} surface. On relaxation the equilibrium morphologies do not correspond to the unrelaxed ones. This is because of the much greater relaxation of the {100} surface compared to the {001} surface of La_2CuO_4 and the {001} surface compared to the {100} surface of Nd_2CuO_4. This demonstrates that surface relaxation must be included in order to calculate the equilibrium morphology of ternary oxides. A similar conclusion was reached by Mackrodt et al. (214) in their calculation of the equilibrium morphologies of the binary oxides α-Al_2O_3 and α-Fe_2O_3.

In figures 5.13 and 5.14 the equilibrium morphologies before and after relaxation of each cuprate have been recalculated allowing for the formation of higher index {10n} (n=1 to 6) and {m10} (m=1,2) surfaces. These figures show that the {100} and {001} surfaces will not be the only surfaces which determine the equilibrium crystal habit. Crystals that are grown in laboratories usually form platelets (204,205,206) and do not adopt the equilibrium morphologies predicted in figures 5.13 and 5.14. This suggests that the experimental crystal morphologies are dominated by kinetic factors.

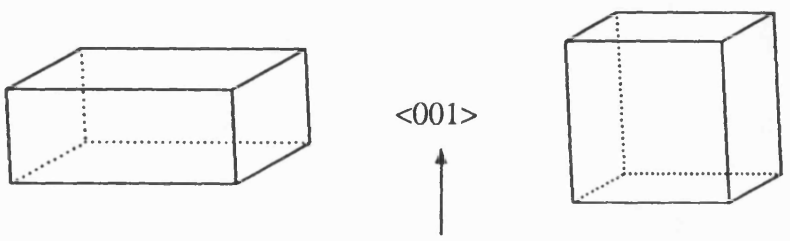

Figure 5.11: The calculated unrelaxed and relaxed equilibrium morphologies of La_2CuO_4 (a) unrelaxed (b) relaxed

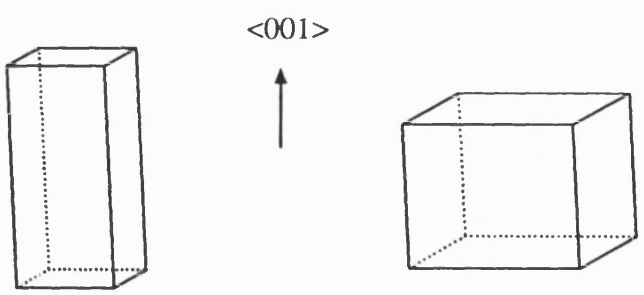

Figure 5.12: The calculated unrelaxed and relaxed equilibrium morphologies of Nd_2CuO_4 (a) unrelaxed (b) relaxed

(morphologies generated using 'morph' package - see ref. 203)

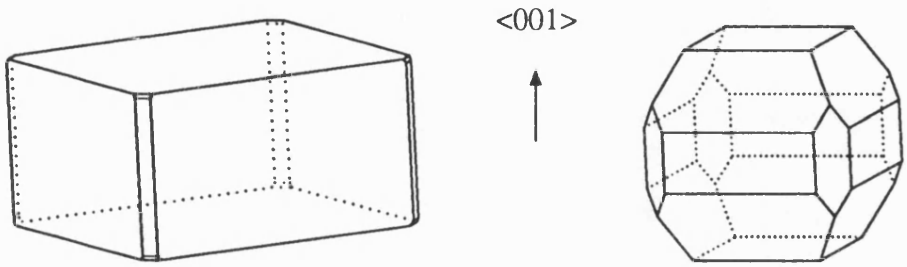

(a) (b)

Figure 5.13: The calculated unrelaxed and relaxed equilibrium morphologies of La_2CuO_4 (including the higher index surfaces) (a) unrelaxed (b) relaxed

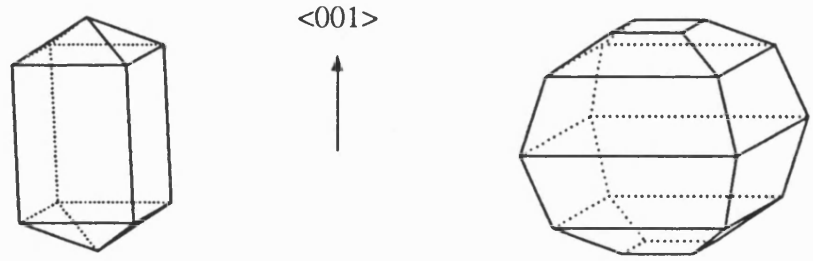

(a) (b)

Figure 5.14: The calculated unrelaxed and relaxed equilibrium morphologies of Nd_2CuO_4 (including the higher index surfaces) (a) unrelaxed (b) relaxed

5.7 Summary

In this Chapter, the {10m} (m=zero or integer), {n10} (n=integer) and the {001} surfaces of La_2CuO_4 and Nd_2CuO_4 are classified into three types. Type 1 surfaces are composed of a stack of neutral planes and the {100} surfaces of both materials belong to this class. The planes which make up type 2 surfaces are not neutral but the stacking sequence is such that it is not dipolar perpendicular to the surface. The {10m} ($m\neq0$) and {n10} (n=even) surfaces make up this type. Type 3 surfaces are the same as type 2 surfaces except that the stacking sequence is dipolar. The {001} surface of Nd_2CuO_4 and the {n10} (n=odd) surfaces are of this type. Thus only the {001} surfaces of the two materials fall into different categories.

The orders of stability of the surfaces before and after relaxation are different because the surfaces relax by different amounts. Similar behaviour has been observed in the corundum structured oxides (214). Also, the relaxation behaviour and surface structures are complicated and - for the surfaces investigated - do not follow the trends observed for the rock-salt oxides (209).

The {001} surface of Nd_2CuO_4, which is inherently dipolar, has a low surface energy (1.3 Jm^{-2}). This is not surprising because the surface has been reconstructed to remove the dipole moment perpendicular to the surface. The stabilities of three other dipolar surfaces (the {001}OCu of La_2CuO_4 and the {110}O surfaces of La_2CuO_4 and Nd_2CuO_4) were also calculated by halving the density of ions in the surface plane. These surfaces were not as stable as the {001} surface of Nd_2CuO_4. The results show that reconstructed surfaces along dipolar directions in ternary oxides can have low energies.

The equilibrium morphologies of the two materials are different. This is partly because the surfaces have different structures and also because they exibit different relaxation behaviour. The predicted morphologies are not similar to the

experimentally grown crystals. This may be due to the assumption that thermodynamic equilibrium is maintained throughout crystal growth which is unlikely to be applicable for such large crystals. Furthermore, crystals grown in laboratories are often intentionally (204) or unintentionally (206) doped, whereas these calculations are for pure crystals.

The large relaxations observed at surfaces that are not parallel to the ab plane will disrupt the CuO_2 planes and consequently have a deleterious effect on intergranular conductivity. Surface conduction at the {001} surfaces will be disrupted by rumpling of the CuO_2 planes, but this will be much lower in La_2CuO_4. Surface composition and non-stoichiometry will also influence conductivity and they are discussed in the next Chapter.

Chapter 6

Surface Defect Properties of La_2CuO_4 and Nd_2CuO_4

6.1 Introduction

In this chapter, calculations on point defect formation energies at the {001} and {100} surfaces of La_2CuO_4 and Nd_2CuO_4 using the CHAOS (85) code developed by Duffy and Tasker are discussed. The same potentials as those in Chapter 5 were used and the theoretical methods are described in Chapter 2.

Stoichiometric La_2CuO_4 and Nd_2CuO_4 are antiferromagnetic semiconductors (182). When La_2CuO_4 is doped with appropriate monovalent cations (215), divalent cations (216) and/or excess oxygen is incorporated into the lattice (217), the Néel temperature (T_N) of the antiferromagnetic state decreases and at $T_N = 0$ K La_2CuO_4 becomes a spin glass. A further increase in the impurity concentration results in this cuprate becoming a superconductor at low temperatures. Nd_2CuO_4 shows a similar change in magnetic and electronic properties (182) when it is doped with appropriate tetravalent cations and fluorine and prepared under reducing conditions (28,29,39,31). This behaviour is believed to be related to oxidation or reduction of the copper oxide planes in the two materials respectively (218).

Defect concentrations at surfaces and grain boundaries also play an important role in determining the properties of these materials. For example, the preparation of good tunnelling interfaces composed of metal-interface-superconductor sandwiches (MIS) is hampered by dead layers which arise from changes in surface stoichiometry (219). In common with other ceramic materials (220,221), defect and impurity concentrations are likely to differ from the bulk. Consequently, the stoichiometry and composition of the {100} and {001} surfaces of tetragonal La_2CuO_4 and Nd_2CuO_4

are investigated in this chapter. In the next section, bulk and surface point defect calculations are compared. Then the fundamental surface lattice disorder in the stoichiometric compounds is considered. Next, electronic defects, non-stoichiometry and impurities are discussed. The final section of this chapter deals with the calculation of surface defect concentrations.

6.2 Comparison of Surface and Bulk Point Defect Calculations

The relaxed configuration of the surface generated by MIDAS is used as a starting point for the point defect calculations. Madelung energies calculated from the surface code on the surface plane are different from those in the interior of the crystal. This is illustrated in table 6.1 which gives the Madelung energies at copper sites near the {001} surface of La_2CuO_4. Over the first 3 planes (about 13 Å in depth) the Madelung energies at copper sites are different, but by the 4th plane (about 20 Å in depth) they have settled down to a constant value. However, the constant Madelung energies do not equal those determined by a bulk simulation code e.g. CASCADE (81) because different boundary conditions are used in each calculation. The relaxation of the surface, which is not included in the bulk calculation, induces (222) an electrostatic potential into the bulk of the crystal which is independent of depth (223). The shift in the Madelung field can be quantified by the expression 'qV', where q is the full ionic charge of the ion involved and V, the shift in potential. The shift in V depends on the magnitude of the displacement of the ions at each surface and hence is unique for each surface. In the following sections defect formation energies have been adjusted so that the constant Madelung energy equals that of the bulk calculation. In this way the formation energies can be compared with corresponding bulk values as well as those for other surfaces.

Although the boundary conditions that are used in the surface and bulk

Table 4.1: Calculated Madelung energies of copper Ions at the {001} surface of La_2CuO_4 compared to the bulk cation Madelung energy

Plane	Madelung Energy
1	52.07
2	53.01
3	52.96
4	52.95
5	52.95
6	52.95
7	52.95
8	52.95
9	52.95
10	52.95
bulk	57.53

calculations are different, the way in which the total energy of the defective system is minimised is the same. As described in chapter 2, the crystal is split into two regions: an inner region (region I) immediately surrounding the defect where the ions are appreciably distorted, and an outer region (region II) where the ions are only slightly perturbed. Ideally the size of region I should be chosen so that the relaxed point defect energy has converged, but as region I is increased the calculation reaches the limit of the available computer resources. In this work, 60 ions were used for the calculations of surface point defect energies. When the results were compared with corresponding calculations using 100 ions the agreement was favourable (i.e. the calculated energies were within 0.1 eV of eachother). Also, the time taken for these calculations was reasonable (e.g. a typical calculation of 20 iterations took 2 hours to run on a SUN 4 workstation).

6.3 Fundamental Lattice Disorder

Ions in crystals are arranged in ordered arrays. Imperfections in stoichiometric crystals (fundamental lattice disorder) are due to missing ions (vacancies) at perfect lattice sites and/or extra ions (interstitials) incorporated at positions in the lattice which do not correspond to perfect lattice sites. In La_2CuO_4 and Nd_2CuO_4, the defects responsible for fundamental lattice disorder are lanthanum, neodymium, copper and oxygen vacancies and interstitials. Calculated surface cation vacancy formation energies are presented and compared with those in the bulk. Calculations on oxygen vacancies and interstitials are then described. These energies are required for the discussion on surface non-stoichiometry (section 6.5) and surface impurity solution (section 6.6). Note that cation interstitial formation energies are high (224) and are not discussed.

6.3.1 Cation Vacancy Formation Energies

Cation vacancy formation energies at the {100} and {001} surfaces of La_2CuO_4 and the {100} surface of Nd_2CuO_4 are given in table 6.2 and compared with the corresponding bulk energies. The formation energies of copper vacancies are lower at the {100} surfaces. In contrast, at the {001} surface of La_2CuO_4 the formation energy of a copper vacancy is 0.8 eV higher than in the bulk. These results can be understood from the difference between the Madelung energies of surface cations and those in the interior of the crystal. These are given in table 6.3. At the {100} surfaces the surface copper Madelung energy is lower than that in the bulk, favouring negatively charged defects. In contrast, the Madelung energy of these sites at the {001} surface of La_2CuO_4 is higher and therefore negatively charged defects are destabilised.

The defect energy is not just determined by the Madelung energies of sites in the unrelaxed crystal, but also by the relaxation about the defect and the image charge resulting from a dielectric discontinuity (the latter being zero for isovalent defects). This is illustrated by comparing the relaxed formation energies of rare-earth vacancies with the corresponding Madelung energies given in tables 6.2 and 6.3. Lanthanum vacancies are more stable at the {100} surface of La_2CuO_4 than in the bulk, which in turn are more stable than at the {001} surface. Also, the formation energies of neodymium vacancies at the {100} surface of Nd_2CuO_4 are less favourable than in the bulk. While the stability of neodymium vacancies at the {100} surface of Nd_2CuO_4 can be understood using the argument of Madelung site energies, the relative stabilities of lanthanum vacancies cannot. This is because the effects of surface relaxation are neglected.

Calculations on cation vacancies at the {001} surface of Nd_2CuO_4 did not lead to stable relaxed configurations. From the Madelung site energies it is tentatively

Table 6.2: Cation formation energies at the {100} and {001} surfaces of La_2CuO_4, the {100} surface of Nd_2CuO_4, and in the bulk (energies in eV)

	La_2CuO_4			Nd_2CuO_4	
	{100}	{001}	bulk*	{100}	bulk
V_{RE}'''	43.3	45.6	44.5	49.9	49.7
V_{Cu}''	30.7	32.3	31.5	27.2	27.5

* reference 224

Note: RE = La, Nd

Table 6.3: Cation site Madelung energies at the {100} and {001} surfaces and in the bulk of La_2CuO_4 and Nd_2CuO_4 (energies in eV)

	La_2CuO_4			Nd_2CuO_4		
Site	{100}	{001}	bulk	{100}	{001}	bulk
Cu	54.35	58.50	57.52	49.94	52.77	50.70
La/Nd	84.75	83.44	84.08	91.19	90.66	90.96

assumed that copper vacancies at this surface are indeed less stable than in the bulk. The stability of rare earth vacancies is less obvious because the difference between the bulk and surface Madelung energy is much smaller. A further calculation using 100 ions in region I of CHAOS also failed and, therefore, the stability of neodymium vacancies at this surface cannot be predicted.

Previous workers (225,226,227) have shown that the formation energies of defects in the sub-surface region of binary oxides may also differ from those in the bulk. However, a complete survey of fundamental lattice disorder would require an excessive number of calculations. Therefore, a study of the change in cation vacancy formation energies with distance from the surface was not conducted.

The relative stabilities of oxygen vacancies and interstitials at the {001} and {100} surfaces of La_2CuO_4 and Nd_2CuO_4 are now discussed. These defects are important because, in the stoichiometric state, anion Frenkel disorder predominates (228) i.e. the majority defects are isolated oxygen vacancies and interstitials. Also, evidence for the existence of extraneous surface oxygen species and/or surface degredation (229,230) has been found.

6.3.2 Oxygen Vacancy Formation Energies

Oxygen vacancies created in the bulk can either be in (equatorial) or out (axial) of the CuO_2 planes. In the bulk of La_2CuO_4 the equatorial oxygen vacancy is more stable than the axial oxygen vacancy (224,231), whereas the reverse is found in Nd_2CuO_4 (232). This means that at low concentrations of oxygen disorder, vacancies will disrupt the CuO_2 planes in the bulk of La_2CuO_4 but not in Nd_2CuO_4.

Depth profiles of the variation in oxygen vacancy energy with distance from the {100} surfaces of La_2CuO_4 and Nd_2CuO_4 are given in figures 6.1 and 6.2. Three different oxygen sites in each stacking plane parallel to the surface can be identified.

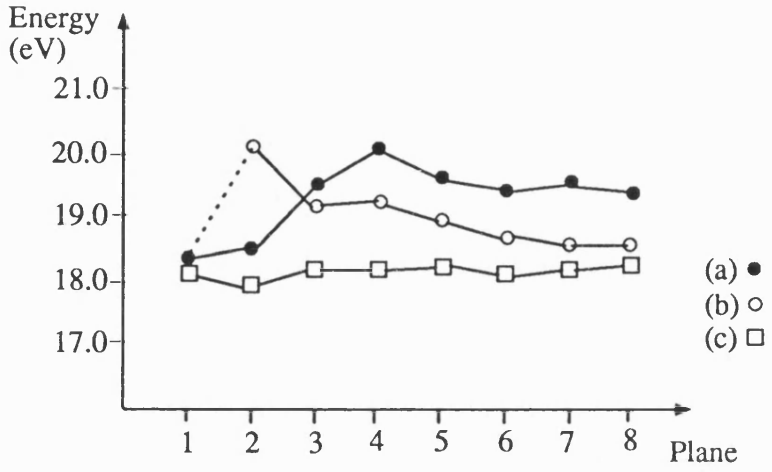

Figure 6.1: Variation of axial (a) and equatorial (b,c) oxygen vacancy formation energies with distance from the {100} surface of La_2CuO_4

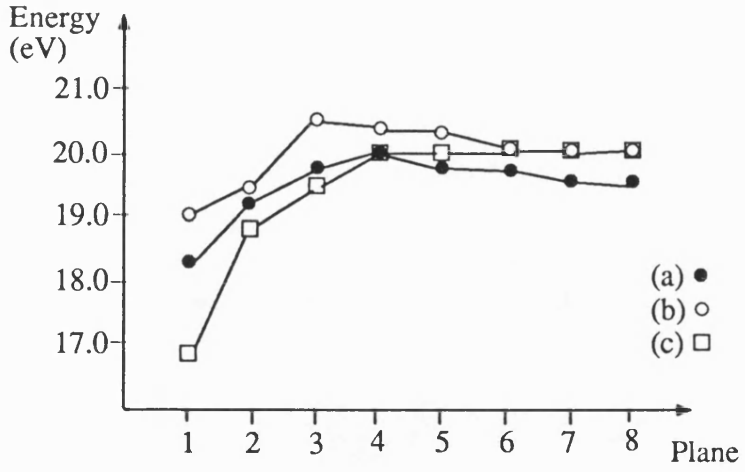

Figure 6.2: Variation of axial (a) and equatorial (b,c) oxygen vacancy formation energies with distance from the {100} surface of Nd_2CuO_4

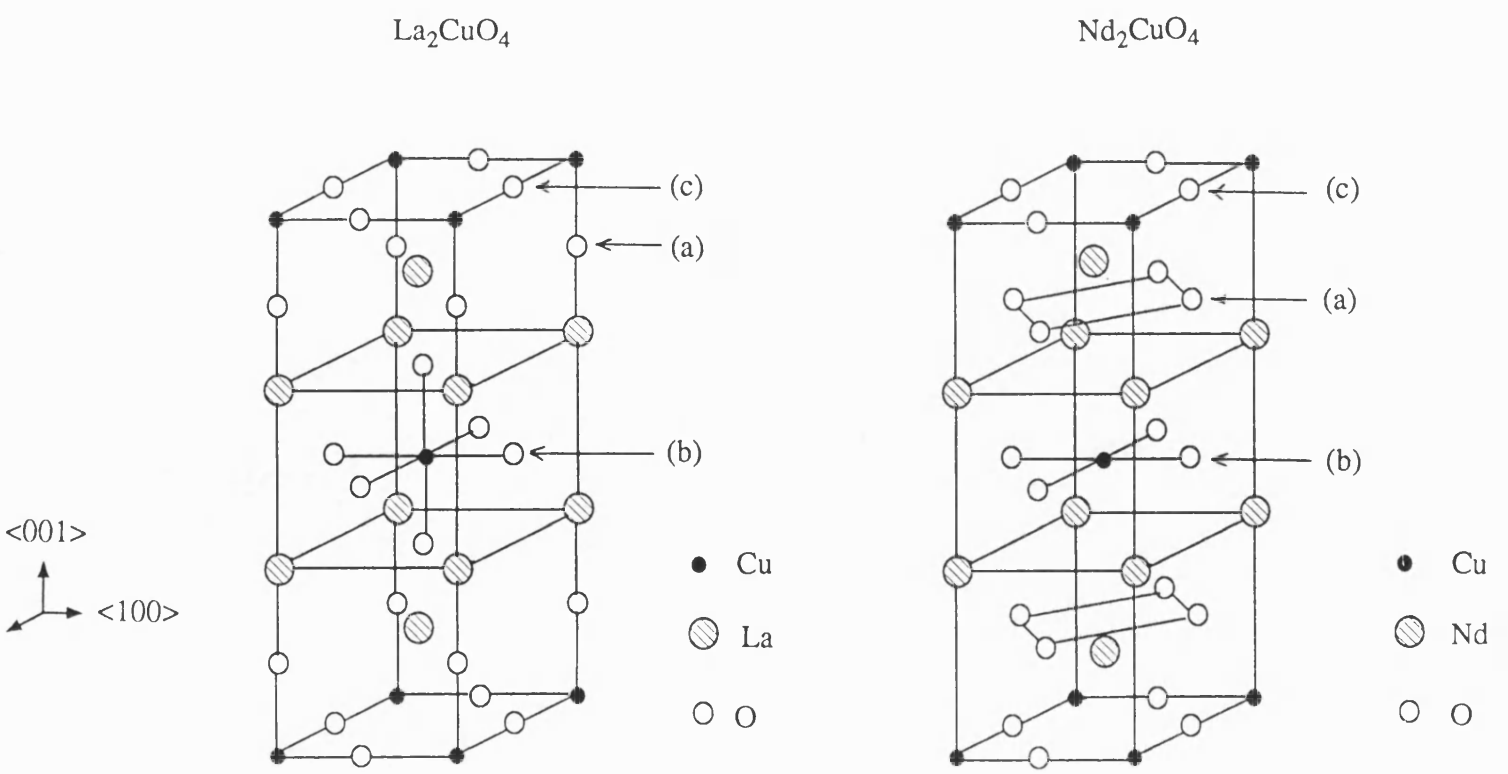

Figure 6.3: The axial (a) and the two equatorial (b,c) oxygen sites at the {100} surfaces of La_2CuO_4 and Nd_2CuO_4

Two of these are equatorial oxygens and the other axial (type a). Those which are equatorial are either in a plane surrounded by four rare earth atoms (type b), or by two copper atoms (type c). The different oxygen sites are shown in figure 6.3.

At the {100} surface of La_2CuO_4, the energies for the axial vacancies (type a) are much lower at the surface than in the bulk and pass through a sub-surface maximum at plane 4 (about 11 Å below the surface). The oxygen vacancies in the CuO_2 plane terminating in a type c site have the lowest formation energy and this energy does not change appreciably with depth from the surface. In contrast, the oxygen vacancies terminating in a type b site are much higher in energy and the surface oxygen vacancy migrates to the axial surface site. The type b oxygen vacancy in the plane below the surface is about 2 eV higher in energy than the corresponding type c oxygen vacancy. As the distance from the surface increases the oxygen vacancy formation energy in the CuO_2 plane terminating in a type b plane decreases and approaches those of the type c plane. In the bulk these two CuO_2 planes are identical. However, even at about 25 Å below the surface there is still a difference of 0.25 eV between oxygen vacancy stabilities within them. From these results it is deduced that near the {100} surface of La_2CuO_4 oxygen vacancies will be confined to CuO_2 planes terminating at c sites. However, at the terminating plane, some vacancies will form at the a sites. Using the law of mass action, the ratio of vacant a/c sites can be estimated from:

$$a/c = 2 \exp \{(V_c - V_a)/kT\} \qquad (6.1)$$

where V_c is the formation energy of a vacancy on site c. At 1000 K this a/c ratio is about 6/10 at the surface.

In Nd_2CuO_4, the most stable oxygen vacancy sites at the {100} surface and in the bulk are different (figure 6.2). The bulk formation energies are 17.97 eV and

17.69 eV for the equatorial and axial sites respectively. At the surface, type c sites are 1.51 eV more stable than axial type a sites. The difference in surface and bulk oxygen vacancy stabilities is greatest in the surface plane. Type b oxygen vacancy formation energies pass through a maximum at plane 3 (about 8 Å below the surface) and at plane 6 (about 20 Å below the surface) they become identical to type c oxygen vacancies, so that bulk behaviour is reached. In the second and third planes the concentration ratio of oxygen vacancies in the a and c sites is about 1/10 and at plane 4 the relative stability of vacancies in equatorial and axial positions changes over. Thus over the first four planes (about 12 Å) the population of oxygen vacancies will be much greater in the CuO_2 planes than in the bulk. The depth over which the surface defect populations are different from the bulk is much less than the {100} surface of La_2CuO_4 and this is attributed to the difference in relaxation at these two surfaces (see Chapter 5).

The structures of the {001} surfaces in these two materials are markedly different and have been discussed in Chapter 5. At the {001} surface of La_2CuO_4, there are two different oxygen sites and these are equatorial and axial. The variation in oxygen vacancy formation energies is given in figure 6.4. The difference between equatorial and axial sites seen for the bulk is apparent for all but the surface axial oxygen. From figure 6.4, only the surface plane is significantly different from the bulk, probably because this surface does not relax appreciably from a simple bulk termination.

The most stable {001} surface of Nd_2CuO_4 terminates in a CuO_2 plane. The density of ions in this surface plane is half that in the bulk because the surface has been reconstructed to remove the perpendicular dipole (Chapter 5). By inspection of the relaxed positions of the oxygen ions at this surface, it is possible to identify two different sites in the first oxygen plane and four different sites in subsequent planes. Thus for a full investigation of oxygen vacancy stabilities over, for example, the first

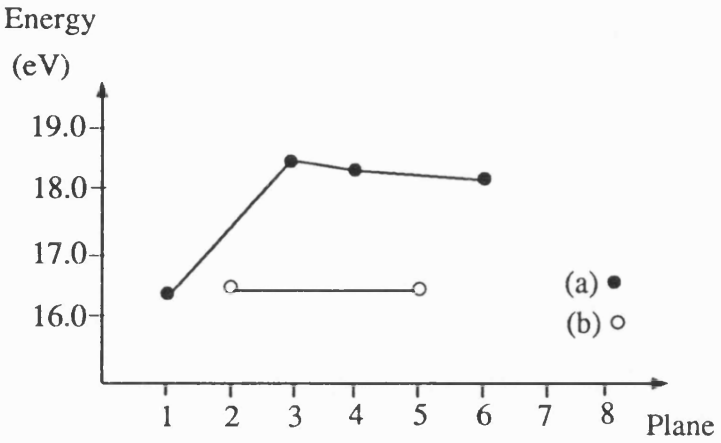

Figure 6.4: Variation of axial (a) and equatorial (b) oxygen vacancy formation energies with distance from the {001} surface of La_2CuO_4

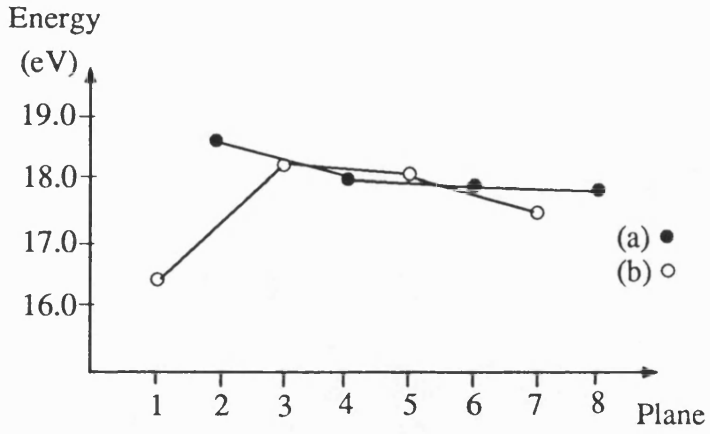

Figure 6.5: Variation of axial (a) and equatorial (b) oxygen vacancy formation energies with distance from the {001} surface of Nd_2CuO_4

5 planes (about 11 Å), 18 calculations would be required. The number of calculations required, however, may be reduced because there are essentially two types of oxygen, those that are equatorial and those that are axial to the CuO_2 planes. Thus to investigate the change in vacancy formation energy with depth, sites were chosen which only differed in their perpendicular distance from the surface. The variation of oxygen vacancy formation energy with depth from the {001} surface of Nd_2CuO_4 is shown in figure 6.5. The equatorial oxygen vacancy with the lowest formation energy is at the surface. The surface axial oxygen vacancy is highest in energy and at the axial sites below the surface the vacancy energy does not vary appreciably. Bulk behaviour, which is achieved in part when axial vacancies are more stable than equatorial ones, is not reached even at about 16 Å below the surface. This surface is different from the other three because it has been reconstructed. Surface relaxation leads to a large shift (5.93 V) in the Madelung potential with respect to the calculated bulk value. Previous work on point defect energies near planar defects oriented along polar directions of a crystal has been confined to the $\{3\bar{1}1\}/[001]$ NiO grain boundary (233). The calculated shift in the Madelung potential was 0.95 V and this is significantly lower than that reported here. Defect formation energies did not converge until the eighth plane (about 12 Å) below the boundary. In view of the greater complexity of the structure and consequent relaxation of the {001} surface, it is reasonable to expect that the effect of the surface will extend over a greater depth than the grain boundary in NiO.

The variation of oxygen vacancy formation energies with depth is different for each of the surfaces. At the {100} surfaces, oxygen vacancies will be concentrated in the CuO_2 planes and consequently disrupt intergranular conductivity. At the {001} surface of La_2CuO_4, the vacancy formation energies are only significantly different from their bulk values at surface axial oxygen sites. Therefore, conductivity at this

surface will be similar to that in the bulk. In contrast, the conductivity parallel to the {001} surface of Nd_2CuO_4 will differ from that in the bulk over a distance of at least 16 Å because the relative stabilities of oxygen vacancies have not converged to their bulk values.

6.3.3 Oxygen Interstitial Formation Energies

Experimental work (234) indicates that doubly charged oxygen interstitials are more stable in the bulk than singly charged ones. This has been confirmed by Mackrodt and Allan (228). Catlow et al. (235) investigated the relative stabilities of singly charged and doubly charged oxygen molecules and interstitials in the bulk of La_2CuO_4. They also found that excess oxygen will be doubly charged and incorporated at bulk interstitial sites. In this section, results are presented on the formation energies of both singly and doubly charged interstitials over the first four sites at each of the four surfaces. The relative stabilities of these defects can be calculated once the hole formation energies are known and these are given in the next section.

The interstitials were introduced at sites that are occupied in the 'non-CuO_2' plane of the other cuprate (figure 6.6). At the {001} surfaces of these cuprates the outermost interstitial was introduced above the terminating plane, whereas at the {100} surfaces the interstitial site was in this plane.

The energies of doubly and singly charged oxygen interstitials at the {100} surface of La_2CuO_4 are given in tables 6.4 and 6.5. Also included in this table are the distances moved by the interstitials on relaxation. Both the singly and doubly charged interstitial in the uppermost plane of this surface move appreciably out of the surface by 2.6 Å and 1.6 Å respectively. The doubly charged oxygen interstitial in the second plane moves by 1.4 Å which is much greater than that of the singly charged interstitial

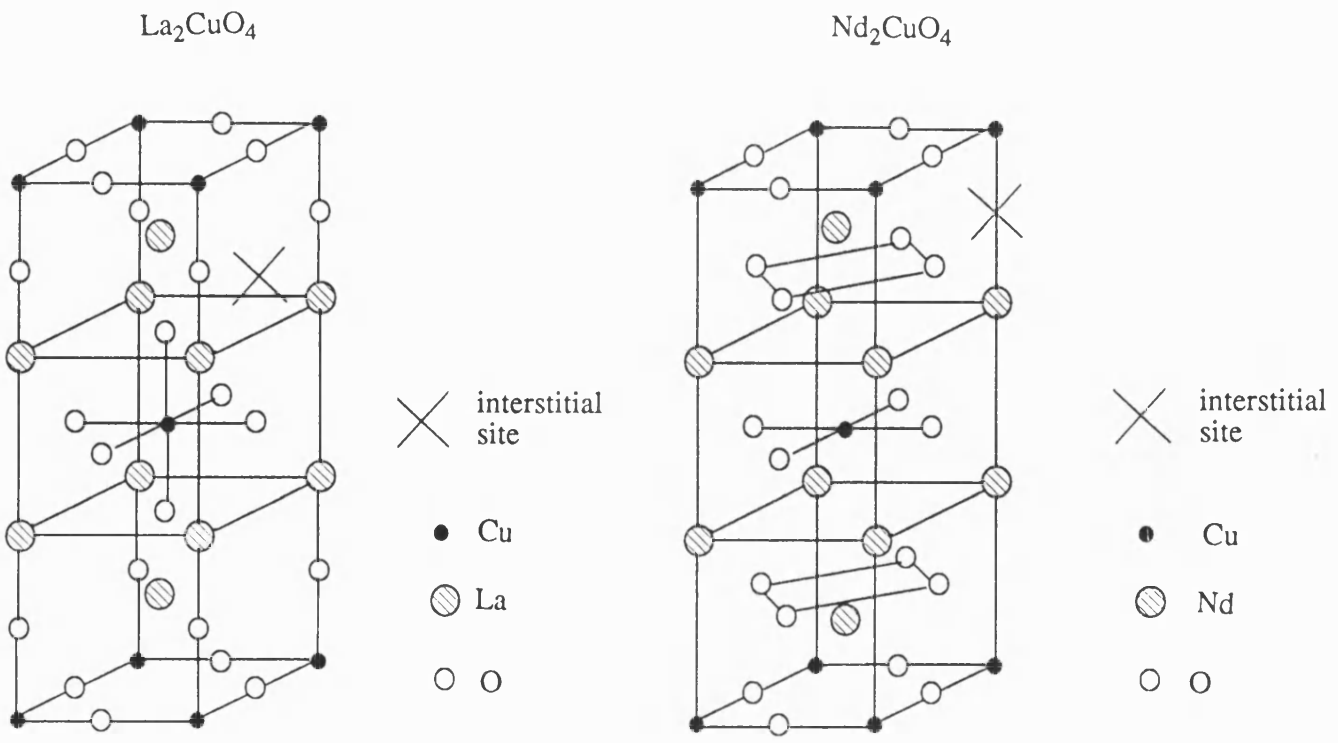

Figure 6.6: Oxygen interstitial sites in La_2CuO_4 and Nd_2CuO_4

Table 6.4: Energies and relaxed coordinates of divalent oxygen interstitials at the {100} surface of La_2CuO_4

Plane	Interstitial Energy(eV)	Relaxed Coordinates* (Å)
1	-15.00	-1.27 0.00 0.95
2	-14.58	-1.37 0.11 0.34
3	-13.33	-0.31 0.00 0.34
4	-12.91	0.08 0.00 0.31
bulk	-13.00	-

Table 6.5: Energies and relaxed coordinates of monovalent oxygen interstitials at the {100} surface of La_2CuO_4

Plane	Interstitial Energy(eV)	Relaxed Coordinates* (Å)
1	-2.86	-1.68 0.00 1.02
2	0.04	0.23 0.00 0.19
3	-0.84	0.34 0.00 0.27
4	-0.33	0.08 0.00 0.27
bulk	-0.59	-

* with respect to unrelaxed coordinates of 0.0 0.0 0.0

Note: the x direction is perpendicular to the surface and and increases with increasing distance into the bulk

(0.3 Å). The interstitials in the third and fourth planes below the surface move by less than 0.5Å. As the doubly charged interstitial is moved further into the bulk, the formation energy increases. Thus, at the surface both singly and doubly charged oxygen interstitials are more stable than in the bulk.

The energies of singly and doubly charged oxygen interstitials at the {100} surface of Nd_2CuO_4 are given in table 6.6 and 6.7 along with the corresponding relaxed coordinates. As with the {100} surface of La_2CuO_4 the calculated energies of the singly and doubly charged interstitial at the surface are lower than in the sub-surface region and in the bulk. However, the relaxation of these surface interstitials is much less and therefore the increased stability over sub-surface substitution is reduced compared to La_2CuO_4.

The energies of singly and doubly charged oxygen interstitials at the {001} surface of La_2CuO_4 are given in table 6.8. The greatest relaxation is experienced by those oxygen interstitials that are introduced above the surface LaO plane. However, on relaxation these oxygens move by less than 0.2 Å into the bulk. Relaxed coordinates for interstitials below the surface are almost identical to the unrelaxed coordinates. As these are equivalent to the equilibrium bulk interstitial sites, sub-surface oxygen is in the same environment as in the bulk. Note that similar behaviour is observed for oxygen vacancies.

The energies of singly and doubly charged oxygen interstitials at the {001} surface of Nd_2CuO_4 are given in tables 6.9 and 6.10. The doubly charged oxygen interstitial is unstable above the surface. Just below the surface, the stability of the oxygen interstitial is much greater than that in the bulk and the enhanced stability is due to the large relaxation from this position. At the third and fourth interstitial sites the doubly charged interstitials do not relax appreciably although their stabilities are lower than in the bulk. The energy of the singly charged oxygen interstitial is lower at the surface than in the bulk and the ion relaxes towards the surface. This is

Table 6.6: Energies and relaxed coordinates of divalent oxygen interstitials at the {100} surface of Nd_2CuO_4

Plane	Interstitial Energy(eV)	Relaxed Coordinates* (Å)
1	-15.42	-0.05 0.04 0.20
2	-13.99	-0.12 -0.04 -0.43
3	-14.32	-0.16 0.04 0.28
4	-14.09	-0.08 0.00 0.28
bulk	-14.35	-

Table 6.7: Energies and relaxed coordinates of monovalent oxygen interstitials at the {100} surface of Nd_2CuO_4

Plane	Interstitial Energy(eV)	Relaxed Coordinates* (Å)
1	-2.39	-0.79 0.00 0.28
2	-1.52	0.00 0.04 0.39
3	-2.03	-0.16 0.04 0.24
4	-1.82	-0.08 0.04 0.39
bulk	-1.92	-

* with respect to unrelaxed coordinates of 0.0 0.0 0.0

Note: the x direction is perpendicular to the surface and and increases with increasing distance into the bulk

Table 6.8: Energies of divalent and monovalent oxygen interstitials at the {100} surface of La_2CuO_4

Plane	Divalent Oxygen Energy(eV)	Monovalent Oxygen Energy(eV)
1	-12.10	-1.43
2	-12.93	-0.69
3	-12.81	-0.49
4	-12.93	-0.53
bulk	-13.00	-0.56

Table 6.9: Energies and relaxed coordinates of divalent oxygen interstitials at the {001} surface of Nd_2CuO_4

Plane	Interstitial Energy(eV)	Relaxed Coordinates* (Å)
1	-	
2	-16.50	-1.50 0.04 -1.34
3	-13.65	0.02 0.00 0.04
4	-13.48	0.13 0.02 0.04
bulk	-14.35	

Table 6.10: Energies and relaxed coordinates of monovalent oxygen interstitials at the {001} surface of Nd_2CuO_4

Plane	Interstitial Energy(eV)	Relaxed Coordinates* (Å)
1	-3.29	0.68 1.22 1.03
2	-5.20	-1.79 -0.03 -1.63
3	-2.21	0.07 0.02 -0.03
4	-1.68	0.33 0.04 -0.04
bulk	-1.92	

* with respect to unrelaxed coordinates of 0.0 0.0 0.0

Note: the x direction is perpendicular to the surface and and increases with increasing distance into the bulk

probably due to the repulsion of the image charge and might explain why no stable minimum was found for the doubly charged interstitial at this position.

To summarise the section on fundamental lattice disorder, it is predicted that the properties of the {001} surface of La_2CuO_4 are very similar to the bulk. In contrast, the other three surfaces show significantly different behaviour to that in the bulk over a depth of at least 10 Å. Defect behaviour is different at each surface and also to that observed at surfaces of binary oxides (225). Thus the anisotropy of electrical properties at different tunnel junctions, for example, will not only be controlled by the orientation of the crystal (236) but also by the different defect concentrations arising from different defect formation energies.

6.4 Surface Electronic Defects

The calculations on electronic defects were performed by modelling the electron as a Cu^{1+} substitutional and the holes as either a Cu^{3+} or O^{1-} substitutional. For each of the substitutional ions two calculations were performed, one to model it either as a small and the other as a large polaron. These correspond to the electronic defect being localised at one site or being localised over nearest neighbour lattice sites respectively. The first calculation is performed by allowing both cores and shells to relax, whereas the second allows only shell relaxation (167).

The formation energy of the small polaron is estimated by adding or subtracting the appropriate ionisation energy from the energy calculated by the simulation program. For the formation of the defect electron this will be the second ionisation potential of copper, whereas for the defect hole this will either be the second electron affinity of oxygen or the third ionisation potential of copper.

In calculating the formation energies of the large polarons, the method

proposed by Mackrodt (167) is used. In this approach, half the value of the appropriate band width is subtracted from the lattice energy term and the ionisation energy. For both ternary oxides the appropriate band widths are taken from Allan and Mackrodt (224) who estimated these values from the electronic structure calculations on La_2CuO_4 of Mattheiss (237), Yu et al. (238) and Bullett and Dawson (239). It is assumed that they can be applied to the surface. These parameters are given in table 6.11.

The results for the {100} and {001} surfaces of La_2CuO_4 are compared to those calculated by Allan and Mackrodt (224) for the bulk in table 6.12. At the {001} surface the large and small polaron copper holes are estimated to have the same energy. Small polaron holes on oxygen are less favoured than large polaron holes by 0.6 and 0.1 eV for the uppermost axial and equatorial oxygen sites respectively. Small polaron electrons are calculated to be more stable than large polaron electrons by 1.1 eV. These calculations also indicate that holes rather than electrons are favoured at copper sites at this surface. Similar results were obtained by Allan and Mackrodt (224). Copper and axial oxygen holes and copper electrons are more favourable at the {001} surface than in the bulk although holes on equatorial oxygens are less favoured.

The electronic defect formation energies for the {100} surface of La_2CuO_4 show marked differences from the bulk and the {001} surface (table 6.12). The large polaron energy of copper holes is estimated to be 0.9 eV less stable than that for the small polaron but the differences between large and small polaron energies at oxygen sites are much less than in the bulk. Axial surface oxygen small polaron holes are of comparable stability to those on copper. In contrast to the bulk and the {001} surface, the formation of small polaron electrons on copper sites are more favourable than holes.

The differences between the two surfaces is attributed to differences in their structures and relaxation behaviour. Relaxation at the {001} surface leads to a

Table 6.11: Energies required to calculate defect energies

Parameter	Energy (eV)
Copper ionisation potentials	
Cu(II)	20.29
Cu(III)	36.83
Oxygen ionisation potentials	
O^{2-} (I)	-9.2
O^{2-} (II)	0.2
Valence band contribution to large polaron energies	
Cu	1.4
O (axial)	1.7
O (equatorial)	2.5
Conduction band contribution to large polaron energies	
Cu	1.0

Table 6.12: Calculated electron/hole energies (eV) at the {100} and at the {001} surfaces and in the bulk of La_2CuO_4

Type		bulk*	{001}	{100}
Valence band holes				
Cu	(l)	1.5	1.2	3.7
	(s)	1.7	1.2	2.8
O (axial)	(l)	3.0	2.2	2.8
	(s)	3.8	2.8	3.0
O (equatorial)	(l)	3.3	3.6	3.4 (type b)
	(s)	3.9	3.7	3.5
O (equatorial)	(l)			2.9 (type c)
	(s)			3.1
Conduction band electrons				
Cu	(l)	2.8	3.4	0.1
	(s)	2.8	2.3	0.2

* from reference 224

Table 6.13: Calculated electron/hole energies (eV) at the {100} and at the {001} surfaces and in the bulk of Nd_2CuO_4

Type		bulk	{001}	{100}
Valence band holes				
Cu	(l)	>4.3*	5.7	5.6
	(s)	4.3*	1.7	3.4
O (axial)	(l)	3.1	4.0	0.8
	(s)	4.0	4.2	3.3
O (equatorial)	(l)	3.1*	4.0	3.3 (type b)
	(s)	4.2*	3.0	3.7
O (equatorial)	(l)			3.1 (type c)
	(s)			3.1
Conduction band electrons				
Cu	(l)	>-0.9*	-0.2	-1.3
	(s)	-0.9*	-2.3	-2.0

* from reference 140

(l) large polaron
(s) small polaron

decrease in the surface energy of 0.5 Jm^{-2}. This relaxation lowers the Madelung site energy between surface and bulk copper sites by 0.98 eV. The relaxation at the {100} surface is much greater and the difference in the surface energy of a simple bulk termination and the relaxed surface is 3.2 Jm^{-2}. This relaxation increases the surface copper site Madelung energy with respect to the bulk by 3.18 eV. Thus from purely electrostatic arguments the oxidation of copper sites at the {001} surface should be more facile than at the {100} surface. However, as noted in section 6.2, relaxation around the defect also contributes to a lowering of the defect formation energies and therefore the most favourable sites cannot necessarily be distinguished by inspecting the Madelung energies of the pure relaxed surface.

The corresponding formation energies at the {100} and {001} surfaces of Nd_2CuO_4 are given in table 6.13 and compared with the results of Allan et al. (140). At the {001} surface, small polaron copper holes are more stable than large polaron holes. The most stable oxygen holes are predicted to occupy surface equatorial positions and be small polarons. However, these are less stable than small polaron copper holes. It is also predicted that electrons at copper sites are small polarons and are more favourable than copper holes. Comparing the results with those of Allan et al. (140), holes at this surface are more stable at copper sites, whereas in the bulk they are more stable at oxygen sites. Both holes and electrons are more stable at this surface than in the bulk.

The electronic defect formation energies at the {100} surface are similar to those in the bulk (34). Small polaron holes are more stable at copper sites and large polaron holes at axial oxygen sites; the latter being more stable. In common with the {001} surface, small polaron electrons are more stable than holes. Both holes and electrons are more stable at the {100} surface than in the bulk.

At the {001} and {100} surfaces of Nd_2CuO_4, the stabilities of holes and electrons cannot be ascribed solely to the differences in the surface and bulk

Madelung energies. At the {100} surface, the Madelung site energy is lower than in the bulk by 0.76 eV (table 6.3), favouring negatively charged defects. While electrons are more stable at surface copper sites, holes are also more stable at these sites. The latter observation is the reverse of what would be predicted from the Madelung site energies. At the {001} surface, holes and electrons are also more stable than in the bulk. The copper site Madelung energy is higher at this surface (by -2.07 eV) and only holes would be expected to be more stable. The differences in the behaviour predicted from the Madelung site energies, and the calculated results is attributed to the relaxation about the defect.

Once the surface electronic defect formation energies have been calculated, surface non-stoichiometry can be investigated. The results are described in the next section.

6.5 Defect Stabilities in La_2CuO_4 and Nd_2CuO_4

The defects which charge compensate aliovalent impurities in these materials are known (240,241) to control their superconducting properties. Consequently the relative stabilities of either positively or negatively charged defects have been calculated by determining the energies of the following reactions:

$$V_O^{\cdot\cdot} + 1/2O_2(g) = O^x_O + 2h^{\cdot} \qquad (6.2)$$

$$O_i'' = 1/2O_2(g) + 2e' \qquad (6.3)$$

$$O_i' = 1/2O_2(g) + e' \qquad (6.4)$$

$$2V_M''' + V_{Cu}'' + 4O^x_O = 2O_2(g) + 8e' \qquad (6.5)$$

which have associated energies E1, E2, E3 and E4. These are given in table 6.14 for the {100} and {001} surfaces and the bulk of La_2CuO_4 or Nd_2CuO_4. Although the exact concentrations will be influenced by the oxygen partial pressure, the energies for each reaction at different surfaces and in the bulk are directly comparable.

Holes are predicted to be more stable than oxygen vacancies in the bulk of La_2CuO_4 and at the {001} surfaces of La_2CuO_4 and Nd_2CuO_4. In contrast, the reverse is true for the {100} surfaces of both materials. In the bulk of Nd_2CuO_4 the concentration of holes and oxygen vacancies will be comparable. In view of the importance of holes in La_2CuO_4, E1 was determined over the first five planes (about 8 Å) of the {100} surface and it was found that even at this depth the energy was higher than the bulk value (0.4 eV at the 5th plane). Thus there will be a greater number of oxygen vacancies with respect to holes in the CuO_2 planes in the surface region. Such a near surface structural inhomogeneity could be 'frozen in' during sample preparation and have a detrimental effect on conductivity.

E2, in table 6.14, corresponds to the reduction of an oxygen rich lattice. These results show that, as with E1, both the relative bulk and surface concentrations of defects will be different. At the {001} surface of La_2CuO_4, the reduction of doubly charged oxygen interstitials is harder than at the {100} surface although both surfaces are more easily reduced than the bulk material. A similar pattern of behaviour is predicted for Nd_2CuO_4 although in this material dissolution of excess oxygen is much more facile.

E3, in table 6.14, corresponds to the ease of oxidising a singly charged oxygen interstitial at the surface. At the {001} surface of La_2CuO_4 and the {100} surfaces of both materials the energy of dissolution of singly charged oxygen interstitials is much lower than E2 and, hence, oxygen interstitials will be doubly charged at both the surface and in the bulk. At the {001} surface of Nd_2CuO_4, E2 and E3 are similar and,

Table 6.14: Calculated stabilities of defects at the {001} and {100} surfaces and in the bulk of La_2CuO_4 and Nd_2CuO_4

	La_2CuO_4			Nd_2CuO_4		
Reaction	bulk*	{001}	{100}	bulk	{001}	{100}
E1	-1.5	-2.4	1.1	0.2	-1.4	3.1
E2	7.7	5.9	3.8	1.1	0.3	-0.2
E3	1.0	0.8	0.7	-1.4	0.5	-2.0
E4	29.1	26.5	9.0	-1.0	-	-10.9

* from reference 224

therefore, the concentration of singly and doubly charged oxygen interstitials will be comparable.

E4 corresponds to lattice reduction by loss of oxygen from the perfect lattice sites. These results show that in La_2CuO_4 cation vacancies are much more stable than electrons. However, the reverse is true at the {100} surface and in the bulk of Nd_2CuO_4 with electrons being more stable than cation vacancies. The stabilities of electrons and cation vacancies at the {001} surface of Nd_2CuO_4 cannot be calculated because of the instability of neodymim vacancies.

From these results, negatively charged impurities e.g. Ca_{RE}' (RE=La, Nd) will be charge compensated by holes at both {001} surfaces and in the bulk of La_2CuO_4, whereas charge compensation in the other crystal environments will be by oxygen vacancies. As discussed above, this will have a detrimental effect on p-type conduction at the {100} surface of La_2CuO_4. Positively charged impurities e.g. $Ce_{RE}^{\cdot}$ (RE=La, Nd) will be charge compensated by oxygen interstitials and cation vacancies in La_2CuO_4 and are therefore not n-type superconductors. In contrast, electrons compensate these impurities in Nd_2CuO_4.

The surface properties of these materials will not only be influenced by the type of defects which compensate aliovalent impurities, but also by nature of the impurities themselves. This is investigated in the next section by considering both impurity segregation and site solution.

6.6 Surface Impurity Substitution and Site Solution

Cation impurities control many of the properties of ceramic oxides. In the case of high-T_C materials related to La_2CuO_4 and Nd_2CuO_4 they are intimately connected with the superconductivity. The influence of surface composition and stoichiometry is investigated in two ways. First, the difference in the substitution energies of Mg^{2+},

Ca^{2+}, Sr^{2+}, Ba^{2+}, Ce^{4+} and Th^{4+} at surface and bulk rare-earth and copper sites in La_2CuO_4 and Nd_2CuO_4 is calculated. Second the relative importance of mixed site solution at copper and rare-earth sites is considered. In the final section of this chapter, these results are used to calculate how surface and bulk impurity concentrations differ.

6.6.1 Surface and Bulk Substitution Energies

Substitution energies for the impurities at both copper and rare-earth sites at each of the surfaces and in the bulk are given in tables 6.15 and 6.16. The substitution energies vary significantly between different surfaces and this is because the structures and relaxation behaviour of the surfaces are different. In general, for a given substitution type the energy increases with increasing ion size. In order to compare the substitution energies, an interaction energy is defined, which is the difference in energy in substituting the defect at a given site at the surface ($E_{SURFACE}$) and in the bulk (E_{BULK}):

$$E_{INT} = E_{SURFACE} - E_{BULK} \qquad (6.6)$$

If this energy is negative then at equilibrium the defect will segregate to a given surface site, although for aliovalent defects their surface concentration is also affected by the space charge.

The interaction energies at copper sites for divalent impurities are plotted against host-impurity ion size mismatch in figures 6.7 and 6.8. Those for Mg^{2+} are small at each surface which is to be expected because the ion sizes of Mg^{2+} and Cu^{2+} are similar. For the other three divalent impurities the interaction energies at the {100} surfaces of both cuprates and the {001} surface of Nd_2CuO_4 are exothermic

Table 6.15: Substitution energies at copper sites at the {100}, the {001} and in the bulk of La_2CuO_4

Cation	{100}	{001}	bulk
Mg	1.0	1.6	1.5
Ca	5.1	10.4	10.3
Sr	7.0	15.8	16.4
Ba	8.4	20.3	22.6
Ce	-52.1	-46.2	-45.7
Th	-47.3	-39.7	-39.2

Table 6.16: Substitution energies at copper sites at the {100}, the {001} and in the bulk of Nd_2CuO_4

Cation	{100}	{001}	bulk
Mg	1.0	1.3	1.1
Ca	4.2	4.7	6.4
Sr	5.6	6.2	9.1
Ba	6.8	6.6	12.1
Ce	-48.8	-48.4	-44.4
Th	-45.9	-41.3	-39.5

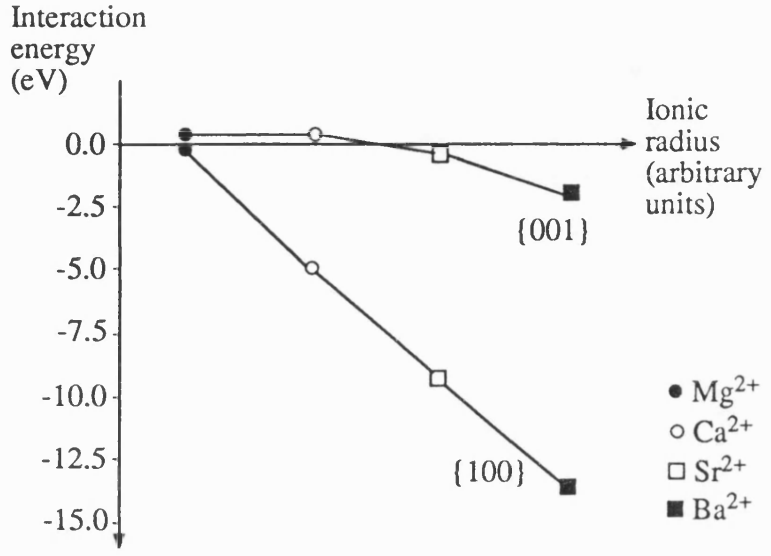

Figure 6.7: Interaction energies of divalent cations at {001} and {100} surface copper sites in La_2CuO_4

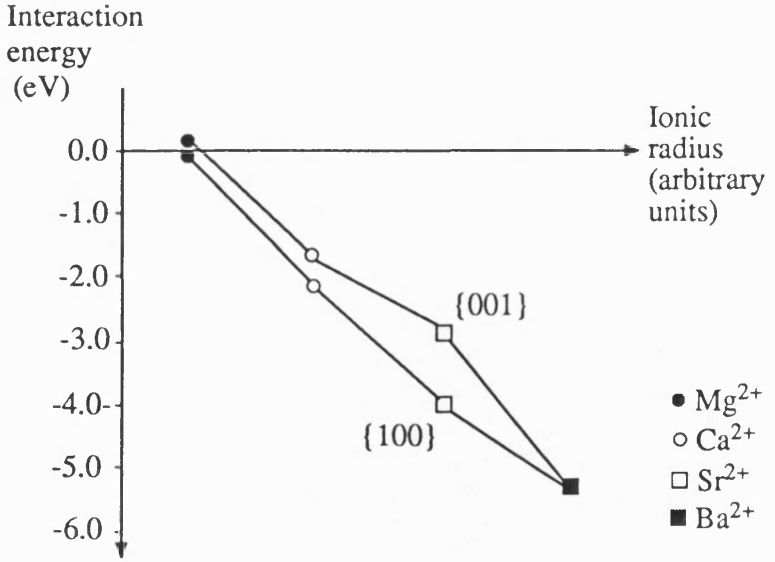

Figure 6.8: Interaction energies of divalent cations at {001} and {100} surface copper sites in Nd_2CuO_4

and increase with increasing ion size. This is in accord with an increase in interaction energy with increasing ion size for the segregation of Ca^{2+}, Sr^{2+} and Ba^{2+} at the {100} surface of MgO and Na^{+} and K^{+} at the {111} surface of Li_2O (242). In contrast, the calculated interaction energy of Ca^{2+} at the {001} surface is identical to that of Mg^{2+} and slightly endothermic, whereas those for Sr^{2+} and Ba^{2+} are exothermic. This difference between the trends in interaction energies at these surfaces can be understood by considering their structures. As discussed in Chapter 5, the {001} surface of La_2CuO_4 terminates in a layer of LaO and relaxation about sub-surface copper is restricted. The terminating planes of the other surfaces all contain copper and the possible relaxation about the divalent impurities is much greater. Thus, the crystal environment of the copper site of {001} surface of La_2CuO_4 is markedly different from that at the other three surfaces. When Mg^{2+} and Ca^{2+} are substituted at surface sites the relaxation is restricted and similar to that in the bulk. Consequently their interaction energies are close to zero. For Sr^{2+} and Ba^{2+}, relaxation is greater at the surface because they are much larger than Cu^{2+} and the interaction energies are exothermic.

The interaction energies at rare-earth sites for divalent impurities are plotted against host-impurity ion size mismatch in figures 6.9 and 6.10. The interaction energies at none of the surfaces vary monotonically but as the difference in the radii of the divalent cation and the rare-earth cation increases the interaction energy becomes more exothermic. The ionic radii of the Ca^{2+}, Nd^{3+} and La^{3+} cations are similar (their ionic radii are 1.03, 1.17 and 1.12 Å respectively (155)) and the relaxation arising from the relief of elastic strain at the surface will be small. In contrast, the difference in the radii of Mg^{2+}, Sr^{2+} and Ba^{2+} (their ionic radii 0.68, 1.33 and 1.49 respectively Å (18)), compared with Nd^{3+} and La^{3+} is more appreciable. The strain induced by substituting these cations at rare earth sites in the bulk is thus greater than that for Ca^{2+}. The relief of this strain is more effective at the surface than

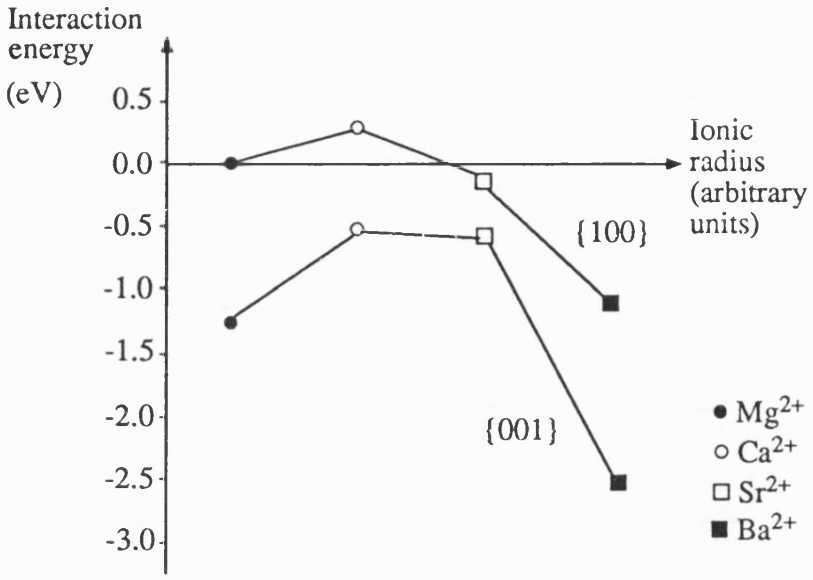

Figure 6.9: Interaction energies of divalent cations at {001} and {100} surface lanthanum sites in La_2CuO_4

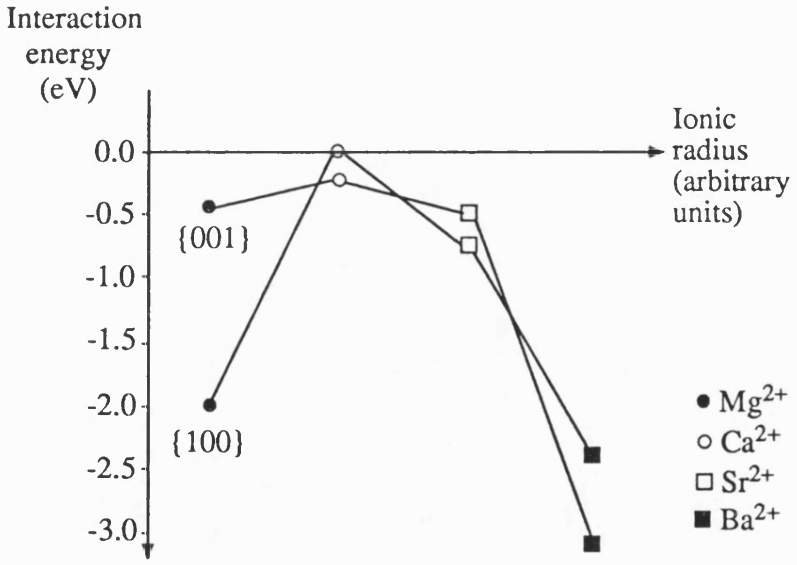

Figure 6.10: Interaction energies of divalent cations at {001} and {100} surface neodymium sites of Nd_2CuO_4

in the bulk and, therefore, the interaction energies of Mg^{2+} and Ba^{2+} and to a lesser extend Sr^{2+} will be more exothermic than those of Ca^{2+}. Note that the magnitude of the interaction energies are also influenced by the image charge interaction, surface relaxation and Madelung site energy and these are different at each surface.

The interaction energies of Ce^{4+} and Th^{4+} cations at each of the four surfaces are presented in table 6.17. At both the {100} surfaces and at the {001} surface of La_2CuO_4 the interaction energies at lanthanum sites of Ce^{4+} and Th^{4+} are positive indicating that they will not segregate to these surface sites. In contrast, interaction energies are exothermic for neodymium site substitution at the {001} surface of Nd_2CuO_4 and at copper sites at each of the four surfaces. This behaviour cannot be explained by just the Madelung site potentials (table 6.1) and, therefore, it must be due to details of the relaxation about the defect.

By themselves the interaction energies can be used to determine whether an ion will segregate from a given bulk to surface site. For binary oxides where only one site is available this information can be used to determine the degree of segregation of uncharged impurities and this was done for the specific case of alkaline earths in sapphire in Chapter 4 (note that in this case it was assumed that there was only one surface site and no account of kink and step sites was taken). For ternary oxides, the possibility of solution at different bulk cation sites (243) and surface cation sites and must also be considered. This is discussed in the next section.

6.6.2 Energetics of Solution in La_2CuO_4 and Nd_2CuO_4

The divalent cations Ca^{2+}, Sr^{2+}, Ba^{2+}, and the tetravalent cations Ce^{4+} and Th^{4+} substitute at rare earth sites in the bulk of La_2CuO_4 and Nd_2CuO_4. When La_2CuO_4 is doped with an appropriate concentration of the divalent impurities it is rendered a p-type superconductor. In contrast, Nd_2CuO_4 is an n-type superconductor

Table 6.17: Interaction energies of cerium and thorium at copper and rare-earth sites of La_2CuO_4 and Nd_2CuO_4 (energies in eV)

	La_2CuO_4				Nd_2CuO_4			
	{001}		{100}		{001}		{100}	
	Cu	La	Cu	La	Cu	La	Cu	La
Ce	-0.5	0.4	-6.4	0.0	-4.4	-0.8	-5.1	0.3
Th	-0.5	0.4	-8.1	0.4	-6.2	-0.6	-1.7	0.1

when doped with appropriate concentrations of the tetravalent cations. The difference in behaviour between these two cuprates can be understood by considering the charge compensating impurities and this was done in section 6.5. Doping either ternary oxide with Mg^{2+} leads to substitution at copper sites and this disrupts the periodic potential of the CuO_2 planes thereby disrupting high-T_C behaviour (244).

Solution at copper sites may be represented by the defect equations

$$XO + Cu^x_{Cu} = X^x_{Cu} + Cu^x_{Cu} + O^x_O \qquad (6.7)$$

for divalent cations and for tetravalent cations compensated by either electrons:

$$XO_2 + Cu^x_{Cu} = X_{Cu}^{\cdot\cdot} + 2e' + 1/2O_2 + Cu^x_{Cu} + O^x_O \qquad (6.8)$$

or cation vacancies:

$$XO_2 + Cu^x_{Cu} = X_{Cu}^{\cdot\cdot} + Cu^x_{Cu} + O^x_O + 1/4RE_2CuO_4 + 1/2V_{RE}''' + 1/2V_{Cu}'' \qquad (6.9)$$

with corresponding energies E5, E6a and E6b respectively. The analogous equations for solution at lanthanum or neodymium (RE=La, Nd) sites are:

$$XO + RE^x_{RE} + 1/4O_2(g) = X_{RE}' + h^{\cdot} + RE^x_{RE} + 3/2O^x_O \qquad (6.10)$$

or

$$XO + RE^x_{RE} = X_{RE}' + 1/2V_O^{\cdot\cdot} + RE^x_{RE} + 3/2O^x_O$$

(6.11)

for divalent cations with charge compensating defects as holes or oxygen vacancies respectively and for tetravalent cations compensated by either electrons:

$$XO_2 + RE^x_{RE} = X_{RE}^{\cdot} + e' + RE^x_{RE} + 3/2O^x_O + 1/4O_2 \qquad (6.12)$$

or cation vacancies:

$$XO_2 + RE^x_{RE} = X_{RE}^{\cdot} + RE^x_{RE} + 3/2O^x_O + 1/4V_{RE}''' + 1/8V_{Cu}'' + 1/8RE_2CuO_4 \qquad (6.13)$$

for tetravalent cations with corresponding energies E7a, E7b, E8a E8b. In order to calculate the energies of E5 to E8 the lattice energies of the constituent oxides are required and these are given in table 6.18. The solution energies of divalent impurities are given in tables 6.19 and 6.20.

Mg^{2+} is the only divalent cation that has been considered that will dissolve at bulk and surface copper sites in La_2CuO_4 (table 6.19). The other three divalent cations will dissolve at lanthanum sites in the bulk and at the {001} surface of La_2CuO_4. In agreement with the calculations on surface stoichiometry, the behaviour of impurities is different at the {100} surface than in the bulk and the {001} surface because Ca^{2+}, Sr^{2+} and Ba^{2+} will dissolve at copper sites.

The results presented in table 6.20 demonstrate that there will be differences in the mode of solution at the {001} and {100} surfaces and the bulk of Nd_2CuO_4. In the bulk Ca^{2+}, Sr^{2+} and Ba^{2+} will dissolve at neodymium sites, whereas, Mg^{2+} is predicted to substitute at both neodymium and copper sites. At the {001} surface Mg

Table 6.18: Calculated lattice energies of binary oxides (energies in eV)

Oxide	Lattice Energy
MgO	-42.03
CaO	-37.14
SrO	-34.83
BaO	-32.67
CeO_2	-109.29
ThO_2	-104.97
La_2O_3	-130.10
Nd_2O_3	-137.42
CuO	- 42.75*
CuO	-41.14**

* For calculations in La_2CuO_4

** For calculations in Nd_2CuO_4

Table 6.19: Calculated bulk and surface solution energies (eV) of divalent impurities in La_2CuO_4

Impurity	bulk		{001}		{100}	
	E5	E7a	E5	E7a	E5	E7b
Mg	0.8	2.4	0.9	1.4	0.3	1.6
Ca	4.0	0.3	4.8	0.1	-0.5	0.0
Sr	7.3	-0.3	7.8	-0.9	-0.9	-0.5
Ba	11.0	-0.1	10.2	-1.6	-1.7	-1.1

Table 6.20: Calculated bulk and surface solution energies (eV) of divalent impurities in Nd_2CuO_4

Impurity	bulk		{001}		{100}	
	E5	E7b	E5	E7a	E5	E7b
Mg	2.0	2.2	2.2	0.5	1.9	-1.0
Ca	2.4	1.1	0.7	-0.5	0.2	-1.0
Sr	2.8	1.3	-0.2	-0.5	-0.7	-0.7
Ba	3.6	2.3	-1.9	-2.2	-1.7	-1.4

and Ca dissolve exclusively at neodymium sites. Sr^{2+} and Ba^{2+} will also dissolve at neodymium sites but some copper site solution can be expected. A similar trend is expected at the {100} surface, although Ba^{2+} substitution at copper sites is more favoured at neodymium sites.

A comparison of results for the bulk of the two materials shows that the solution energy at a given site varies systematically with ionic radius i.e. at copper sites the solution energies increase with increasing ion size and at lanthanum or neodymium sites the solution energies decrease and then increase. Similar behaviour has also been observed for bulk cation solution energies at copper (245) and barium (246) sites in $YBa_2Cu_3O_7$. The trends in the solution energies at each of the {100} and {001} surfaces of the cuprates are different from each other and the bulk. This is because the surface solution energies depend not only on the impurity substitution energy, but also the nature of the charge compensating defect. These in turn are related to the structure and relaxation behaviour.

The solution energies of Ce^{4+} and Th^{4+} in the bulk and at the four surfaces are given in table 6.21 and 6.22. In the bulk and at the {001} surface of La_2CuO_4, Ce^{4+} and Th^{4+} will dissolve exclusively at lanthanum sites because the ionic sizes of Ce^{4+} and Th^{4+} (155) are much closer to those of lanthanum than copper. However, at the {100} surface the impurities relax appreciably, and substitution at copper sites can be expected.

Solution of tetravalent impurities in the bulk and at the two surfaces of Nd_2CuO_4 will only occur at neodymium sites (table 6.22). Note that the solution energy is also reduced at the copper sites of both surfaces but solution at neodymium sites is still more favourable.

To summarise this section, two aspects of cation impurity distribution in two ternary oxides have been described. These are the difference in substituting the defect

Table 6.21: Calculated bulk and surface solution energies (eV) of quaternary impurities in La_2CuO_4

Impurity	bulk		{001}		{100}	
	E6b	E8b	E6b	E8b	E6b	E8b
Ce	7.8	2.3	8.0	3.2	0.6	1.9
Th	10.0	2.1	10.2	2.9	1.1	2.1

Table 6.22: Calculated bulk and surface solution energies (eV) of quaternary impurities in Nd_2CuO_4

Impurity	bulk		{001}		{100}	
	E6a	E8a	E6a	E8a	E6a	E8a
Ce	10.9	1.1	3.6	-1.1	3.8	0.3
Th	10.8	1.2	1.8	0.8	6.9	0.2

at the surface and in the bulk and surface and bulk solution energies. A defect will segregate if the interaction energy between a given surface and bulk site is negative. For example, Ba^{2+} at the {001} surface of La_2CuO_4 (Figure 6.9). Segregation can also occur when the energy required to dissolve it at either site at the surface is less than that in the bulk. For example, Ba^{2+} at the {100} surface of Nd_2CuO_4 (table 6.20). Isovalent surface impurity concentrations can be estimated from these results using the McLean isotherm (149). This can also be done when the impurity is aliovalent, provided that the surface plane is charge neutral. This charge neutrality assumption is valid when either the impurities form neutral clusters or when the formation energies of impurities and charge compensating defects are the same (247). The binding energies of the impurity clusters are small in the bulk (224) and also at the surface. Therefore, either the charge neutrality condition must be relaxed or defect formation energies must be compared. Both approaches are discussed in the next section.

6.7 Space Charge Effects

In this section, the way in which the space charge influences surface segregation is discussed. The space charge does not effect isovalent impurity segregation e.g. Mg_{Cu}^{x} at the {001} surface of La_2CuO_4. However, where solution at two sites is favoured, e.g. Sr_{Cu}^{x} and Sr_{La}' at the {100} surface of La_2CuO_4 then it will indirectly change impurity concentrations. The space charge develops because the constraint of charge neutrality which exists in each unit cell in the bulk is relaxed at the surface. This condition still applies over the surface region (which might extend over several hundred angstroms (248)), but within a given unit cell a greater concentration of a defect may be present if it has a lower formation energy. For the case of a solid where Schottky disorder (i.e. the majority defects are cation and anion vacancies) predominates this can be illustrated as follows. Suppose the free energy

necessary to form a cation vacancy is less than that required to form an anion vacancy. Then, at a temperature where thermal equilibrium can be achieved, there will be a tendency to form an excess of cation vacancies and this will result in a region of negative space charge below the surface. The excess concentration of cations will be deposited at the surface which thus acts as a vacancy source (The surface composition might alternatively be described as having an excess of anion vacancies although this is exactly the same as an excess of cations). At equilibrium then, a dipole region will exist at the surface with an associated electric field gradient. This potential difference changes the innate formation free energies of the vacancies into effective formation energies in such a way that the bulk of the crystal is electrically neutral. The charge distribution that develops will retard the further formation of cation vacancies while enhancing the formation of anion vacancies in the space charge region.

The potential arising from a near-surface inhomogeneous defect distribution has been calculated by Kliewer and Koehler (249) for Schottky defects in M^+X^-. Yan et al. (250) extended their work to include dipole interactions and defect segregation. In what follows, the approach of Kliewer and Koehler is summarised and the way in which it can be used to investigate space charge effects in non-stoichiometric compounds discussed.

Consider an electrically neutral crystal having free {100} surfaces at x=0 and x=2L with bidimensional periodicity in the surface plane and assume that the potential $\phi(x)$ arising from a distribution of Schottky defects in NaCl can be described by Poisson's equation for a medium with static dielectric constant ϵ. The boundary conditions for the potential are:

$$\phi = 0 \text{ at } x = 0 \text{ and } x = 2L \qquad (6.14)$$

and

$$d\phi/dx = 0 \text{ at } x = L \qquad (6.15)$$

Boundary condition 6.15 follows immediately from symmetry and expresses the fact that, since the entire crystal is neutral, each half will also be neutral. Thus, only the section of the crystal from x=0 to x=L need be considered. It is further assumed that the system is in a state of thermal equilibrium. That is, the defects all have sufficiently high mobilities to reach the state predicted by the minimisation of the free energy of the system. At low temperatures this assumption has limited validity as pointed out by Kliewer (251) and Yan et al. (252).

There are three types of defects which may arise. These are anion vacancies, cation vacancies and bound vacancy pairs which arise from the Coulombic attraction between oppositely charged species. The pairs are considered to have a binding energy B when they are on nearest neighbour sites and otherwise no binding energy, hence, ignoring the long range effects of the Coulombic interaction.

The free energy per unit area of the crystal from x=0 to x=L is:

$$F = \int_0^L [\, n_+(x)F^+ + n_-(x)F^- + n_B(x)(F^+ + F^- - B)$$

$$+ 1/2\rho(x)\phi(x)\,] - TS_C \qquad (6.16)$$

where $n_+(x)$ is the density of cations at a distance x below the surface, $n_-(x)$ the density of anion vacancies, $n_B(x)$ the density of bound pairs, F(x) the corresponding free energies and S_C the configurational entropy. The charge density $\rho(x)$ is given by:

$$\rho(x) = e\,[\, n_-(x) - n_+(x)] \qquad (6.17)$$

and is related to $\phi(x)$ by Poisson's equation:

$$d^2\phi(x)/dx^2 = -4\pi\rho(x)/\epsilon \qquad (6.18)$$

Kliewer and Koehler minimised the free energy (equation 6.16) to obtain the defect densities at temperature T. They found that when the concentration of vacancies and bound pairs are much less than one the defect densities are given by:

$$n_+(x) = N \exp\{-(F^+ - e\phi(x))/kT\} \qquad (6.19)$$

$$n_-(x) = N \exp\{-(F^- + e\phi(x))/kT\} \qquad (6.20)$$

$$n_B(x) = N z_n \exp\{-(F^+ + F^- - B)/kT\} \qquad (6.21)$$

where N is the number of lattice sites per unit volume and z_n the number of nearest unlike neighbours of an ion. Therefore, substituting 6.8 and 6.9 into 6.6:

$$d^2\phi(x)/dx^2 = 4\pi eN/\epsilon \, [\exp\{-(F^+ - e\phi(x))/kT\}$$

$$- \exp\{-(F^- + e\phi(x))/kT\}] \qquad (6.22)$$

Now as discussed above, the charge density on a plane in the bulk is zero because of the charge neutrality condition and, therefore, the bulk potential is given by:

$$e\phi(\infty) = 1/2 \, (F^+ - F^-) \qquad (6.23)$$

Kliewer and Koehler further showed that by defining:

$$z(x) = (e\phi(x) - e\phi(\infty)/kT \qquad (6.24)$$

Poisson's equation can be rewritten as:

$$d^2z(x)/dx^2 = \kappa^2 \sinh z(x) \qquad (6.25)$$

with

$$\kappa^2 = 8\pi Ne^2/\epsilon kT \exp\{ -(F^+ + F^-)/2kT\} \qquad (6.26)$$

When $\kappa L >> 1$ then z is given by:

$$z(x) = 4\tanh^{-1}\{e^{-s(x)} \tanh(z_0/4)\} \qquad (6.27)$$

where $z = z_0$ at $x = 0$ and $s = \kappa x$. Thus the potential, zero at the surface becomes $\phi(\infty)$ in the bulk of the crystal.

Of central importance to this derivation are the defect formation energies. They not only determine the bulk potential but also the concentration of defects in the space charge region. For Schottky and Frenkel defects the free energies can be calculated by the methods described in Chapter 2. In non-stoichiometric crystals, the energies of electronic defects can also be calculated (see section 6.4), but their relationship to the defect formation energies of equation 6.16 is ambiguous. This problem can be resolved by relating the space charge to the interaction energies (178) of the defects responsible for non-stoichiometry. The added advantage of this definition is that a two site segregation model is incorporated in the treatment of the

space charge.

The defect with the greatest interaction energy forms in excess at the surface and the sub-surface region is rich in the charge compensating defect. For low bulk impurity concentrations, n(∞), a reasonable measure of the thickness of the space charge region is given by:

$$\kappa^{-1} = (\epsilon kT/e^2 8\pi n(\infty))^{1/2} \qquad (6.28)$$

where e is the electronic charge. This equation is valid when the defect concentrations are much less than one. Using the computed values for the static dielectric constant, ϵ, of 198.0 (224) and 24.3 for La_2CuO_4 and Nd_2CuO_4 respectively the screening length can be determined for a given bulk concentration. For bulk concentrations of 100 ppm and 1000 ppm and a temperature of 1000 K the corresponding screening lengths for La_2CuO_4 are 1.5×10^{-8} m and 4.7×10^{-9} m and for Nd_2CuO_4 are 5.14×10^{-9} m and 1.62×10^{-9} m. Furthermore, the boundary acts as a defect sourec (178) when the ratio of defects in the space charge region in the absence of the surface is much less than the surface defect concentration. This can be quantified by defining a parameter A such that:

$$A = \kappa^{-1}(N/N_S)\exp[(F_{INT}^{+} + F_{INT}^{-})/2kT] \qquad (6.29)$$

where F_{INT}^{+} and F_{INT}^{-} are the interaction energies of cation and anion vacancies and N_S is the density of sites on the surface. When $A < 1$, the boundary acts as a defect source.

Mackrodt and Allan (228) have shown that the majority defects in the oxygen rich materials are holes and doubly charged oxygen interstitials. The interaction energies at the {100} and {001} surfaces of Nd_2CuO_4 are -0.9 and -2.6 eV for holes

and -1.1 and -2.2 eV for doubly charged oxygen interstitials respectively. Thus, the {100} surface will be negatively charged with an excess of oxygen interstitials and this will be compensated by an excess of holes in the sub-surface region. In contrast, the {001} surface will be positively charged with holes. In both cases $A < 1$ and, therefore, the boundary will act as an infinite source of oxygen interstitials and holes.

The interaction energies of holes and doubly charged oxygen interstitial energies at the {001} surface of La_2CuO_4 are -0.3 and 0.9 eV respectively. Thus in this case the surface will be positively charged with a sub-surface excess of oxygen interstitials and holes. However, the surface will not act as a defect sink because $A > 1$. Thus both the potential arising from the space charge and the difference in the bulk and surface concentrations will be small.

At the {100} surface of La_2CuO_4 holes are less stable than oxygen vacancies. The interaction energy is defined as the energy required to exsolve a hole from the bulk and dissolve an oxygen vacancy at the surface. The interaction energies for holes and doubly charged oxygen interstitials are 0.8 and -2.0 eV respectively. This surface will be negatively charged with an excess of oxygen interstitials and the space charge region will be positively charged and can be subdivided into two regions. Near the surface (the first 8 Å) the ratio of the concentration oxygen vacancies to holes will be greater than that in the bulk, whereas in the remainder of the space charge region the concentration of oxygen vacancies will be negligible. As the value of A is 0.07 the surface will act as a defect sink and, therefore, the increased concentration of oxygen vacancies in the CuO_2 planes will be significant. If this inhomogeneity becomes 'frozen in' during preparation, it may be a source of intergranular weak links. The possibility of weak links arising from the space charge of oxygen vacancies has also been postulated by Clarke et al. (186) in $YBa_2Cu_3O_{7-x}$.

These results compare favourably with the work of Rogers et al. (253) who found evidence for near-surface enrichment by oxygen in a polycrystalline sample of

$La_2CuO_{4.13}$. However, it should be noted that the concentrations in theory and experiment are markedly different.

In the extrinsic regime the properties of the space charge are controlled by aliovalent impurities. Mg^{2+}, Ca^{2+}, Sr^{2+} and Ba^{2+} segregation to the two surfaces of La_2CuO_4 and Ce^{4+} and Th^{4+} segregation to the surfaces of Nd_2CuO_4 is considered. For singly charged positive impurities (with an interaction energy of F_{INT}^{I}) and singly charged electrons (with an interaction energy of F_{INT}^{e}) the bulk potential is given by (254):

$$e\phi(\infty) = 1/2(F_{INT}^{I} - F_{INT}^{e}) + kT\ln(1 + \delta) \qquad (6.30)$$

with

$$\delta = \frac{2A\sinh\{(F_{INT}^{e} - F_{INT}^{I})/4kT\}}{1 + A\cosh\{(F_{INT}^{e} - F_{INT}^{I})/4kT\}} \qquad (6.31)$$

Equation 6.19 and 6.20 are valid when $\delta < 1$. An analogous equation gives the bulk potential that is due to negatively charged impurities and holes.

Copper site solution is predicted for Mg^{2+} at both the {001} surface and in the bulk of La_2CuO_4. The interaction energy is 0.1 eV and, therefore, the concentration of Mg^{2+} at this surface will be similar to that in the bulk. The other three divalent cation impurities dissolve at bulk and surface lanthanum sites and will be charge compensated by holes, the interaction energy of the latter being -0.3 eV. The interaction energy of Ca^{2+} is positive and, hence, this cation will not segregate to this surface. The interaction energy of Sr^{2+} is small and negative and, therefore, the concentration of this cation at the surface and the bulk will be similar. The sub-surface concentration of these impurities will increase because the surface will be

positively charged due to an excess of holes. As A > 1 the concentration of defects in the space charge region as a whole will be similar to that of the bulk. In contrast to Ca^{2+} and Sr^{2+}, the {001} surface will act as a defect source for Ba^{2+} because A = 0.05. As δ = 0.5, the bulk potential and surface impurity concentration can be calculated from equation 6.30 (254). For a bulk impurity concentration of 100ppm the value of $e\phi(\infty)$ is 0.3 eV and the surface concentrations of Ba_{La}' and holes are 283 x 10^3 and 94 x 10^3 ppm respectively.

At the {100} surface of La_2CuO_4, Mg^{2+} dissolves at surface copper sites. Using equation 4.21 and assuming the entropy of segregation is zero, the surface concentration at 1000 K for an impurity concentration of 100 ppm is then 0.03. The other three cations segregate to both surface copper and lanthanum sites. Solution at copper sites will only be significant at the surface, however, because the substitution energies on other planes are significantly higher (figure 6.11). In each case the cation interaction energies are exothermic (Ca^{2+}; -0.6 eV; Sr^{2+} -0.6 eV; Ba^{2+} -1.3 eV) and the cations will segregate to the surface. The surface concentration of aliovalent defects will be influenced by the interaction energy of positive charge (holes in the bulk and vacancies at the surface) which was calculated to be 0.8 eV. Thus, although the {100} surface will be negatively charged and enriched by calcium, strontium and barium, it will not act as a defect source because in each case A > 1. The importance of segregation to copper sites can be gauged by calculating the difference in exsolving the M_{La}' (M = Ca, Sr, Ba) from the bulk and then dissolving it at the surface. The assumption used here is that the corresponding change in the bulk concentration is small enough not to influence the space charge. The energies of this reaction for Ca^{2+}, Sr^{2+} and Ba^{2+} are -0.8, -0.6 and -1.6 eV respectively. Using equation 4.21, surface concentrations of 0.5, 0.1 and full monolayer coverage are predicted. However, this assumes that the substitution energy is independent of coverage. From figure 6.12, this is clearly not the case. Using equation 4.35 and assuming that the segregation

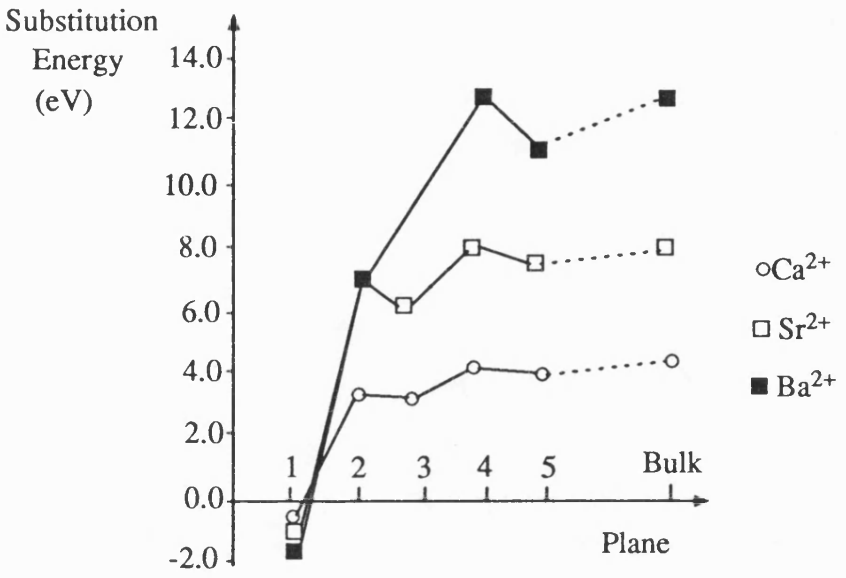

Figure 6.11: Plot of the variation of substitution energy of Ca^{2+}, Sr^{2+} and Ba^{2+} ions at {100} copper sites of La_2CuO_4

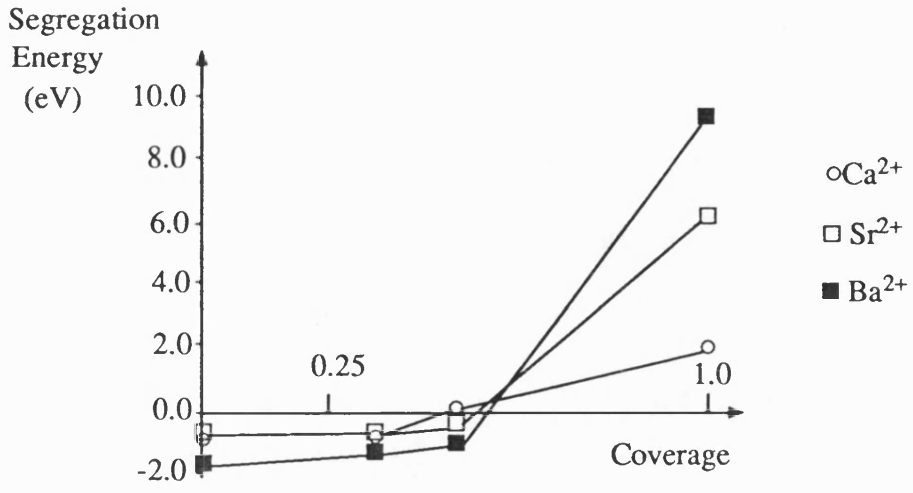

Figure 6.12: Plot of the variation of segregation energy of Ca^{2+}, Sr^{2+}, and Ba^{2+} ions from bulk lanthanum to {100} surface copper sites in La_2CuO_4

entropy is negligible, the calculated surface coverages at 1000 K for a bulk concentration of 100 ppm of calcium, strontium and barium at copper sites are 0.2 0.05 and 0.42 of a monolayer respectively. Note that as the concentration of surface impurities increases this will influence the formation energies of other defects.

These results are supported by the photoemission studies of Egdell et al. (255) and Roshko et al. (256) who observed strontium segregation at free surfaces and grain boundaries of $La_{2-x}Sr_xCuO_4$ respectively. Evidence for the segregation of Ca^{2+} to grain boundary copper sites of $La_{2-x}Ca_xCuO_4$ has also been found (257) and is in accord with these results. However, it should be noted that although grain boundaries are less dense than the bulk, direct comparison with surface phenomena should be treated with care.

At the {001} surface of Nd_2CuO_4, Ce^{4+} and Th^{4+} are predicted to segregate to neodymium sites. The interaction energy of electrons (-1.4 eV) is more negative than that of either Ce^{4+} (-0.8 eV) and Th^{4+} (-0.6 eV) and therefore the surface will be negatively charged with a excess of Ce^{4+} and Th^{4+} in the space charge region. As $A < 1$ for both Ce^{4+} and Th^{4+} the surface will act as a defect source but the exact surface concentrations cannot be estimated because the requirement that the number of impurities on the surface (n_S) is much less than the total number of surface sites (N_S) is not fulfilled. At the {100} surface the interaction energies of Ce^{4+} and Th^{4+} are small and positive whereas that for electrons is negative (-1.1 eV). Thus the surface will be negatively charged will the sub-surface concentration of tetravalent cations will increase. In common with the {100} surface of Nd_2CuO_4 this surface will act as a defect source but again the concentration of defects cannot be calculated because the requirement $n_S << N_S$ does not hold.

6.8 Summary

In this chapter, atomistic simulation has been used to investigate the surface defect properties of ternary oxides. Infinitely dilute defect concentrations were only considered for which the materials are semi-conductors. At higher hole or electron concentrations La_2CuO_4 and Nd_2CuO_4 become metallic and these results must be treated with caution.

The results show that defect and impurity behaviour at the {001} surface of La_2CuO_4 is similar to that in the bulk and is attributed to the small relaxation of this surface. In contrast, the surface stoichiometry and defect properties at the {001} surface of Nd_2CuO_4 and the {100} surfaces of both materials show markedly different behaviour. Although this is due to a combination of the surface structure, relaxation and Madelung site potentials the relationship between these properties and the defect behaviour is by no means clear and surface defect formation energies must be calculated explicitly.

The treatment of aliovalent defects and impurities at the surfaces of these two oxides was different from that described in chapter 4 because the binding energies of defects and impurities are negligible. Thus, the charge neutrality condition on each plane no longer applies and interactions with the space charge must be considered. Although this discussion was fairly simple, three cases were identified. The first was when the surface did not act a defect source and therefore the concentration of defects on the surface plane was less than that in the space charge region in the absence of the surface. The second case was when the surface acted as a defect source and the bulk potential and surface defect concentrations could be determined quantitatively. In the last case the enhanced surface defect concentration is so large that the approximations made in the analytical derivation of the expressions break down. A quantitative description of the space charge must then be obtained by numerical methods (258).

However, at such high defect concentrations it is possible that the material will become metallic and therefore the space charge will be screened.

Conclusions

This thesis has been concerned with the application of computer simulation techniques to study surface phenomena. There have been two major achievements. The first was extending the simulations to include the vibrational entropy contribution to surface and segregation free energies of corundum structured oxides. The second was extending these techniques to study defects at the surfaces of ternary oxides.

In Chapter 4, calculations on the segregation of magnesium and calcium to the $\{10\bar{1}0\}$ prism and calcium to the basal surface of α-Al_2O_3 were discussed. These impurities were considered because small additions of MgO, but not CaO, promote the densification of α-Al_2O_3. The calculated segregation potential energies were used to calculate the change in impurity coverage at the prism surface. The results for the prism surface compared favourably with experiment, even though the vibrational entropy of segregation had not been calculated explicitly. Calcium was predicted to segregate at the basal surface of α-Al_2O_3. The mismatch between theory and experiment for this surface was attributed to kinetic factors.

The vibrational contribution to the basal surface free energy and the segregation of calcium at the basal surface were calculated using lattice dynamics. All previous studies on corundum structured oxides have neglected this effect. The calculations showed that the major component to the surface and segregation free energies is the potential energy. This is in accord with calculations on cubic oxides.

In Chapter 5 and 6, computer simulation techniques were extended to include ternary oxide surfaces. Two oxides were considered: La_2CuO_4 and Nd_2CuO_4. These materials are important because they are the parent compounds of p-type and n-type superconductors respectively.

In Chapter 5, the structures and energies of the {001} and {100} surfaces were discussed and compared to those of the higher index surfaces. It was found that

surface relaxation, which disrupts the CuO_2 planes, alters the relative stabilities of ternary oxide surfaces. This was demonstrated by calculating the equilibrium morphologies which showed significant changes on relaxation. The equilibrium morphologies were also compared with experiment and it was concluded that kinetic factors play an important role in determining the morphologies of crystals grown in a laboratory.

The non-stoichiometry and composition of the {001} and {100} surfaces of La_2CuO_4 and Nd_2CuO_4 were discussed in Chapter 6. Defect formation energies at each of the surfaces were significantly different from previous calculations on bulk behaviour. The difference in calculated bulk and surface energies could not be predicted by a simple comparison of the pure bulk and surface Madelung site energies. This is because relaxation about the defect and the image charge also influence surface defect formation energies. The relative stabilities of positively (oxygen vacancies and holes) and negatively (cation vacancies, oxygen interstitials and electrons) charged defects at the four surfaces were also calculated. At the {100} La_2CuO_4, oxygen vacancies are more stable than holes, in contrast to the {001} surface and in the bulk. This behaviour will also disrupt the CuO_2 planes at the {100} surface. In Nd_2CuO_4, cation vacancies are less stable than electrons at the {001} and {100} surfaces and in the bulk.

Impurities also influence the surface properties of oxides. Surface and bulk substitution energies of divalent and tetravalent cations at copper sites were calculated. These were used to determine impurity interaction energies (the difference in substituting the energy at the surface and in the bulk). For isovalent impurities in binary oxides these correspond to segregation energies. For ternary oxides, the solution of impurities at two cation sites must be considered. Calculations on the surface and bulk solution energies showed that calcium, strontium and barium segregation to {100} surface copper sites of La_2CuO_4 can be expected.

Any treatment of aliovalent surface defect concentrations in ceramic oxides must take into account of the formation of a space charge. This was done by defining a parameter, A, which represented the ratio of defects or impurities at the surface to the concentration of defects in the space charge region in the absence of the boundary. When A is greater than 1 the boundary does not act as a defect source. When A is less than 1 defects accumulate at the boundary. However, when the concentration of particular impurities is high, La_2CuO_4 and Nd_2CuO_4 are metallic and the space charge will be screened. The results must then be treated with caution.

The implications for high temperature superconducting behaviour in doped La_2CuO_4 and Nd_2CuO_4 are concerned with their materials interface properties. Surface relaxation will disrupt the CuO_2 planes and this effect can extend over distances greater than 10 Å (similar to the superconducting coherence length in the ab plane). The CuO_2 planes will also be disrupted by oxygen vacancies and the segregation of impurities to copper sites. These will influence intergranular weak links and surface conductivity because the superconducting current is carried by the CuO_2 planes.

To conclude, the work described in this thesis has successfully demonstrated that computer simulation techniques can be applied to study the effects of temperature on corundum structured oxides. The inclusion of the anharmonic contribution to the surface and segregation free energy will be an important addition to this work.

Ternary oxides have also been studied successfully by computer simulation techniques. The work described in Chapter 5 and 6, combined with the work on bulk defect properties by Allan and Mackrodt, shows that the material properties of La_2CuO_4 and Nd_2CuO_4 are well understood. Further work on the grain boundaries of ternary oxides can only enhance this understanding.

References

1. D.A.Bonnell and D.R.Clarke, J. Am. Ceram. Soc., 71 629 (1989)

2. G.Binnig, C.F.Quate and Ch.Gerber, Phys. Rev. Lett., 56 930 (1986)

3. J.Nowotny and L.-C.Dufour (Eds.), Mat. Sci. Mon., vol.47, (Elsevier, Oxford, 1988)

4. V.E.Henrich, Rep. Prog. Phys., 48 1481 (1985)

5. F.A.Kroeger, Adv. Ceram. vol. 10, p1, Ed. W.D.Kingery, (The American Ceramic Society, Columbus, Ohio, 1984)

6. F.A.Grant, Rev. Mod. Phys., 31 652 (1959)

7. J.B.Goodenough, Prog. Solid State Chem., 5 143 (1972)

8. A.W.Sleight, J.L.Gillson, P.E.Bierstedt, Solid State Comm., 17 27 (1975)

9. J.R.Gavaler, Appl. Phys. Lett., 23 480 (1973)

10. L.R.Testardi, J.H.Wernick and W.A.Royer, Solid State Comm., 15 1 (1974)

11. J.G.Bednorz and K.A.Mueller, Z. Phys. B, 64 189 (1986)

12. H.Takagi, S.Uchida, K.Kitazawa and S.Tanaka, Jap. J. Appl. Phys. Lett. 26 1123 (1987)

13. R.J.Cava, R.B.Van Dover, B.Batlogg and E.A.Rietman, Phys. Rev. Lett., 58 408 (1987)

14. C.W.Chu, P.H.Hor, R.L.Gao, and Z.J.Huang, Science, 235 567 (1987)

15. M.K.Wu, J.R.Ashburn, C.J.Torng, P.H.Hor, R.L.Meng, L.Gao, Z.J.Huang, Y.Q.Wang and C.W.Chu, Phys. Rev. Lett., 58 908 (1987)

16. J.D.Jorgensen, M.A.Beno, D.G.Hinks, L.Sonderholm, K.J.Volin, R.L.Hittermann, J.D.Grace, I.K.Schuller, C.U.Segre, K.Zhang and M.S.Kleefisch, Phys. Rev. B, 36 3608 (1987)

17. R.J.Cava, B.Batlogg, R.B.Van Dover, D.W.Murphy, S.Sunshine,

T.Siegrist, J.P.Remeika, E.A.Reitman, S.Zahurak and G.P.Espinosa, Phys. Rev. Lett., 58 1676 (1987)

18. A.F.Wells, 'Structural Inorganic Chemistry', p894, 4th edn. (Clarendon Press, Oxford, 1984)

19. C.Michel, M.Hervieu, M.M.Borel, A.Grandin, F.Deslandes, J.Provost and B.Raveau, Z. Phys. B, 68 421 (1987)

20. H.Maeda, Y.Tanaka, M.Fukutomi and T.Asano, Jap. J. Appl. Phys., 27 1209 (1988)

21. R.M.Hazen, C.T.Prewitt, R.J.Angel, N.L.Ross, L.W.Fingen, C.G.Hadidiacos, D.R.Velben, P.J.Heany, P.H.Hor, R.L.Meng, Y.Y.Sun, Y.K.Wang, Y.Y.Xue, Z.J.Huang, L.Gao, J.Bechtold and C.W.Chu, Phys. Rev. Lett., 60 1174 (1988)

22. C.Politis, Appl. Phys. A, 45 261 (1988)

23. Z.Z.Sheng and A.M.Herman, Nature, 332 55 (1988)

24. R.M.Hazen, L.W.Finger, R.J.Angel, C.T.Prewitt, C.G.Hadidiacos, P.J.Heaney, D.R.Velben, Z.Z.Sheng, A.El.Ali, and A.M.Hermann, Phys. Rev. Lett., 60 1657 (1988)

25. S.Parkin, V.Y.Lee, E.M.Engler, A.I.Nazzal, T.C.Huang, G.Gorman, R.Savoy and R.Beyers, Phys. Rev. Lett., 60 2539 (1988)

26. Z.Kakol, J.Spalek and J.M.Honig, J. Solid State Chem., 288 79 (1989)

27. L.F.Mattheiss, E.M.Gyorgy, D.W.Johnson, Phys. Rev. B, 37 3745 (1988)

28. Y.Tokura, H.Takagi and S.Uchida, Nature, 337 345 (1989)

29. Y.Tokura, H.Takagi and S.Uchida, Phys. Rev. Lett., 62 1197 (1989)

30. J.T.Markert and M.B.Maple Solid State Comm., 70 145 (1989)

31. A.C.W.P.James, D.Murphy and S.Zahurak, Nature, 338 240 (1989)

32. J.Roubort, S.J.Rothman, B.K.Flandmeyer, L.J.Nowicki, J.E.Baker, J. Mat. Res., 3 116 (1988)

33. T.M.French and G.A.Somorjai, J. Phys. Chem., 74 2489 (1970)

34. J.B.Pendry, 'Low Energy Electron Diffraction', (Academic Press, London, 1974)

35. G.Binnig and H.Rohrer, Helv. Phys. Acta, 55 726 (1982)

36. S.Baik, D.E.Fowler, J.M.Blakely and R.Raj, J. Am. Ceram. Soc., 68 281 (1985)

37. J.D.Cawley and J.W.Halloran, J. Am. Ceram. Soc., 69 C195 (1986)

38. W.Hirschwald, Mat. Sci. Mon., vol.47, p61, Eds. J.Nowotny and L.-C.Dufour, (Elsevier, Oxford, 1988)

39. M.J.Norgett and A.B.Lidiard, Phil. Mag., 18 1193 (1968)

40. C.R.A.Catlow, PhD Thesis, Oxford (1974)

41. M.J.L.Sangster and A.M.Stoneham, Phil. Mag. B, 43 597 (1981)

42. R.James, PhD Thesis, London (1979)

43. G.V.Lewis and C.R.A.Catlow, Radiat. Eff., 73 307 (1983)

44. M.S.Islam, Supercond. Sci. Technol., in press

45. P.W.Tasker, Phil. Mag. A, 39 119 (1979)

46. W.C.Mackrodt, P.W.Tasker and E.A.Colbourn, Surf. Sci. 152/153 940 (1985)

47. P.W.Tasker, Adv. Ceram. vol.10, p176, Ed. W.D.Kingery, (The American Ceramic Society, Columbus, Ohio, 1984)

48. D.M.Duffy and P.W.Tasker, Harwell Rept. TP953 (1982), Harwell Lab., U.K.

49. D.M.Duffy and P.W.Tasker, Phil Mag. A, 47 817 (1983)

50. D.M.Duffy and P.W.Tasker, Phil Mag. A, 54 759 (1986)

51. P.W.Tasker and A.M.Stoneham, J. Chim. Phys. (France), 84 147 (1987)

52. A.M.Stoneham, Appl. Surf. Sci., 14 249 (1982/3)

53. A.M.Stoneham and P.W.Tasker, J. Phys. C, 18 L543 (1985)

54. S.C.Parker and G.D.Price, NATO A.S.I. Series C, vol.225, p591, Ed. E.K.H.Salje, (D. Reidel Publ. Company, Dordrecht, 1988)

55. G.D.Price, S.C.Parker and M.Leslie, Phys. Chem. Minerals, 15 181 (1987)

56. P.W.Tasker, Solid State Ionics, 8 233 (1983)

57. P.Masri, P.W.Tasker and J.Hoare, Harwell Rept. R10752 (1983), Harwell Lab., U.K.

58. W.C.Mackrodt and P.W.Tasker, J. Am. Ceram. Soc., 72 1576 (1989)

59. P.Tschaufeser and S.C.Parker to be published

60. P.Tschaufeser, Private communication

61. J.H.Harding, S.C.Parker and P.W.Tasker, 'Non-Stoichiometric Compounds', p337, Eds. J.Nowotny and W.Weppner (1989) (Kluwer, New York, 1989)

62. P.Wynblatt and W.C.McCune, Mat. Sci. Mon., vol.47, p247, Eds. J.Nowotny and L.-C.Dufour, (Elsevier, Oxford, 1988)

63. D.M.Smyth, Adv. Ceram. vol. 23, p339, Eds. C.R.A.Catlow and W.C.Mackrodt, (The American Ceramic Society, Columbus, Ohio, 1987)

64. Y.-M.Chang and C.-J.Peng, Adv. Ceram. vol. 23, p361, Eds. C.R.A.Catlow and W.C.Mackrodt, (The American Ceramic Society, Columbus, Ohio, 1987)

65. N.L.Allan, C.R.A.Catlow and E.A.Colbourn, Chem. In Britain, 26 1079 (1990)

66. M.H.Cohen, 'High Temperature Superconductivity: The First Two Years' p319, Ed R.M.Metzger, (Gordon and Breach Sci. Publ., New York, 1989)

67. J.Nowotny, M.Rekas, D.D.Sarma and W.Weppner Mat. Sci. Mon., vol.47, p669, Eds. J.Nowotny and L.-C.Dufour, (Elsevier, Oxford, 1988)

68. P.P.Ewald, Ann. Physik, 64 253 (1921)

69. M.J.Norgett, Harwell Rept. R7650 (1974), Harwell Lab., U.K.

70. M.J.Norgett, Harwell Rept. R7015 (1972), Harwell Lab., U.K.

71. C.R.A.Catlow, C.M.Freeman and R.L.Royle, Physica B+C, 131 1 (1985)

72. D.E.Parry, Surf. Sci., 49 433 (1975)

73. D.E.Parry, Surf. Sci., 54 195 (1975)

74. M.P.Tosi, Solid State Phys., 16 1 (1964)

75. M.J.Norgett and R.Fletcher, J. Phys. C, 3 163 (1970)

76. M.Born and K.Huang, 'Dynamical Theory of Crystal Lattices', (Oxford University Press, Oxford, 1954)

77. W.C.Davidson, AEC Rept. ANL-5990 (Rev) (1959)

78. R.Fletcher and M.J.D.Powell, Computer J., 6 16 (1963)

79. C.R.A.Catlow and M.J.Norgett, Harwell Rept. M2936 (1976), Harwell Lab., U.K.

80. N.F.Mott and M.J.littleton, Trans. Farad. Soc., 34 485 (1938)

81. M.Leslie, SERC Daresbury Rept. DL/SCI/TM31T (1982), SERC Daresbury Lab., U.K.

82. P.W.Tasker, Harwell Rept. R9130 (1978), Harwell Lab., U.K.

83. J.H.Harding, Harwell Rept. R13127 (1988), Harwell Lab., U.K.

84. D.M.Heyes, M.Barber, J.H.R.Clarke, J. Chem. Soc., Farad. Trans. II, 10 1485 (1977)

85. D.M.Duffy and P.W.Tasker, Harwell Rept. R11059 (1983), Harwell Lab., U.K.

86. B.I.Bleaney and B.Bleaney, 'Electricity and Magnetism', p55, 3rd edn., (Oxford Uni. Press, Oxford, 1985)

87. A.M.Stoneham and P.W.Tasker, Mat. Sci. Mon. vol.47, p1, Eds. J.Nowotny and L.-C.Dufour, (Elsevier, Oxford 1988)

88. M.Matsui, J. Chem. Phys., 91 489 (1989)

89. C.R.A.Catlow, NATO A.S.I. Series C, vol.225, p619, Ed. E.K.H.Salje, (D.

Reidel Publ. Company, Dordrecht, 1988)

90. M.Matsui, private communication

91. T.W.Tsang and L.M.Falicov, Phys. Rev. B, 12 3441 (1975)

92. D.J.Chadi and M.L.Cohen, Phys. Rev. B, 8 5747 (1973)

93. A.Baldereschi, Phys. Rev. B, 7 5212 (1973)

94. G.Filippini, C.M.Gramaccioli, M.Simonetta, G.B.Suffritti, Acta Cryst. A, 32 259 (1976)

95. A.Patel, G.D.Price and M.J.Mendelssohn, submitted to Phys. Chem. Minerals

96. W.Cochran, 'The Dynamics of Atoms in Crystals', p101, (Edward Arnold, London, 1979)

97. S.C.Parker and G.D.Price, Adv. Solid State Chem., vol.1, p295, (JAI Press, London, 1989)

98. R.Car and M.Parrinello, Phys. Rev. Lett., 55 2471 (1985)

99. M.J.Gillan, J. Chem. Soc., Faraday Trans. 2, 85 521 (1989)

100. M.C.Payne, P.D.Bristowe and J.D.Joannopoulos, Phys. Rev. Lett., 58 1348 (1987)

101. M.Needels, M.C.Payne, and J.D.Joannopoulos, Phys. Rev. Lett., 58 1765 (1987)

102. D.C.Allan and M.P.Teter, Phys. Rev. Lett., 59 1136 (1987)

103. M.J.Sanders, M.Leslie and C.R.A.Catlow, J. Chem. Soc. Chem. Comm. 1273 (1984)

104. R.Walker, J. Phys. C, 14 L979 (1981)

105. M.J.Gillan and M.J.Dixon, J. Phys. C, 13 1901 (1980)

106. W.Jost, J. Chem. Phys. 1 466 (1933)

107. A.B.Woods, W.Cochran and B.N.Brockhouse, Phys. Rev. B, 119 980 (1960)

108. E.A.Colbourn, W.C.Mackrodt and P.W.Tasker, Physica B, 131 41 (1985)

109. M.J.Norgett, J. Phys. C, 4 298 (1971)

110. I.D.Faux, J. Phys. C, 4 L211 (1971)

111. A.B.Lidiard and M.J.Norgett, 'Computational Solid State Physics', p385, Eds. F.Hermann, N.W.Dalton and T.R.Koehler, (Plenum, New York, 1972)

112. B.G.Dick and A.W.Overhauser, Phys. Rev., 112 90 (1958)

113. C.R.A.Catlow and W.C.Mackrodt (Eds.), 'Computer Simulation of Solids', (Spinger-Verlag, New York, 1982)

114. P.W.Fowler and P.Tole, Surf. Sci. 197 457 (1988)

115. A.J.Martin and H.Bilz, Phys. Rev. B, 19 6593 (1979)

116. E.A.Colbourn, W.C.Mackrodt and P.W.Tasker, J. Mat. Sci., 18 1917 (1983)

117. P.J.Lawrence, PhD thesis, Bath, (1988)

118. M.Causa, R.Dovesi, C.Pisani, C.Roetti, Surf. Sci., 175 551 (1986)

119. W.R.Busing, Acta. Crystallogr. A, 28 252 (1970)

120. G.V.Lewis and C.R.A.Catlow, J. Phys. C, 18 1149 (1985)

121. G.V.Lewis, C.R.A.Catlow and A.N.Cormack, J. Phys. Chem. Solids, 46 1227 (1985)

122. S.C.Parker, PhD Thesis, London (1982)

123. P.T.Wedepohl, Proc. Phys. Soc., 56 3122 (1972)

124. P.T.Wedepohl, J. Phys. C, 10 1855 (1977)

125. Y.S.Kim and R.G.Gordon, J. Chem. Phys., 60 1842 (1974)

126. P.Hohenberg and W.Kohn, Phys. Rev. B, 136 864 (1964)

127. L.H.Thomas, Proc. Camb. Philos. Soc., 23 542 (1926)

128. E.Fermi, Z. Phys., 48 73 (1928)

129. K.A.Kruekner and J.D.Perez, Phys. Rev. A, 2 2161 (1970)

130. J.C.Slater, Phys. Rev., 81 385 (1951)

131. P.A.M.Dirac, Proc. Camb. Philos. Soc., 26 376 (1930)

132. A.I.M.Rae, Chem. Phys. Lett., 18 574 (1973)

133. J.H.Harding and A.H.Harker, Harwell Rept. R10425 (1982), Harwell Lab., U.K.

134. N.L.Allan, D.L.Cooper and W.C.Mackrodt, Molecular Simulation, submitted

135. A.I.M.Rae, Mol. Phys., 29 467 (1975)

136. W.C.Mackrodt and R.F.Stewart, J. Phys. C, 12 431 (1979)

137. W.C.Mackrodt, Private communication.

138. G.V.Lewis, Physica B, 131 114 (1985)

139. N.L.Allan and W.C.Mackrodt, J. Chem. Soc. Farad. Trans. 2, 85 385 (1989)

140. N.L.Allan, J.M.Lawton and W.C.Mackrodt, Phil. Mag. B, 59 191 (1989)

141. R.L.Coble, J. Appl. Phys., 32 793 (1961)

142. K.A.Berry and M.P.Harmer, J. Am. Ceram. Soc., 69 143 (1986)

143. A.H.Heuer, J. Am. Ceram. Soc., 62 317 (1979)

144. H.L.Marcus and M.E.Fine, J. Am. Ceram. Soc., 55 568 1972

145. R.C.McCune and R.C.Ku, Adv. Ceram. vol. 10, p217, Ed. W.D.Kingery, (The American Ceramic Society, Columbus, Ohio, 1984)

146. C.A.Handwerker, P.A.Morris and R.L.Coble, J.Am.Ceram.Soc., 72 130 (1989)

147. W.C.Mackrodt, Adv. Ceram. vol. 23, p293, Eds. C.R.A.Catlow and W.C.Mackrodt, (The American Ceramic Society, Columbus, Ohio, 1987)

148. W.C.Mackrodt and P.W.Tasker, Mat. Res. Symp. Proc., 60 291 (1986)

149. D.McLean, 'Grain Boundaries in Metals', (Clarendon Press, Oxford, 1957)

150. S.Baik and C.L.White, J.Am.Ceram.Soc., 70 682 (1987)

151. S.M.Mukhopadhyay, A.P.Jardine, J.M.Blakely and S.Baik, J. Am. Ceram. Soc 71 358 (1988)

152. F.A.Kroeger and V.J.Vink, 'Solid State Phys. vol.3', p307, Eds. F.Seitz and D.Turnbull (Academic Press, New York, 1956)

153. W.D.Kingery, H.K.Bowen and D.R.Uhlmann, 'Introduction to Ceramics' 2nd ed. (Wiley, New York, 1976)

154. W.C.Mackrodt, in Adv.Ceram. vol. 10, p62, Ed. W.D.Kingery, (The American Ceramic Society, Columbus, Ohio, 1984)

155. F.A.Cotton and G.Wilkinson, 'Advanced Inorganic Chemistry', 5th Edition, (Wiley, New York, 1988)

156. M.F.Yan, R.M.Cannon and H.K.Bowen, in Adv. Ceram. vol. 6, p255, Eds. M.F.Yan and A.H.Heuer, (The American Ceramic Society, Columbus, Ohio, 1984)

157. E.M.Levin, C.R.Robbins and H.F.McMurdie, 'Phase Diagrams For Ceramacists', (The American Ceramic Society, Columbus, Ohio, 1964)

158. M.J.Davies, P.R.Kenway, P.J.Lawrence, S.C.Parker, W.C.Mackrodt and P.W.Tasker, J.Chem.Soc.,Farad.Trans. 2, 85 555 (1989)

159. S.Baik, Private communication.

160. K.Ando, Adv. Ceram. vol. 23, p293, Eds. C.R.A.Catlow and W.C.Mackrodt, (The American Ceramic Society, Columbus, Ohio, 1987)

161. R.F.Cook and A.G.Schrott, J.Am.Ceram.Soc., 71 50 (1988)

162. V.S.Stubican and J.W.Osenbach, in Adv.Ceram. vol. 10, p406, Ed. W.D.Kingery, (The American Ceramic Society, Columbus, Ohio, 1984)

163. M.J.Gillan, Phil. Mag. A, 43 301 1981

164. P.Masri, P.W.Tasker, J.P.Hoare, J.H.Harding, Surf. Sci. 173 439 (1986)

165. J.H.Harding and A.M.Stoneham, Phil. Mag. B, 43 705 (1981)

166. T.B.Shaffer, 'High Temperature Materials' (Plenum Press, New York,

1964)

167. W.C.Mackrodt, Solid State Ionics, 12 175 (1984)

168. W.Cochran, 'The Dynamics of Atoms in Crystals', p101 (Edward Arnold, London, 1979)

169. P.Masri and P.W.Tasker, Surf. Sci. 149 209 (1985)

170. C.C.Chang, J.Appl.Phys., 39 5570 (1968)

171. R.C.Kurtz and V.E.Henrich, Surf. Sci., 129 345 (1983)

172. S.E.Trullinger and S.L.Cunningham, Phys. Rev. Letts. 30 913 (1973)

173. P.W.Tasker, E.A.Colbourn and W.C.Mackrodt, J. Am. Ceram. Soc., 68 74 (1985)

174. J.H.Harding, Harwell Rept. TP.1078 (1984), Harwell Lab., U.K.

175. J.H.Harding, Phys. Rev. B, 32 6861 (1985)

176. N.L.Allan, W.C.Mackrodt and M.Leslie, Adv.Ceram. vol. 23, p293, Eds. C.R.A.Catlow and W.C.Mackrodt, (The American Ceramic Society, Columbus, Ohio, 1987)

177. J.M.Blakely and H.V.Thapliyal, in 'Interfacial Segregation', eds W.C.Johnson and J.M.Blakely (American Society for Metals, Ohio, 1979)

178. D.M.Duffy and P.W.Tasker, Phil. Mag. A, 50 143 (1984)

179. C.R.A.Catlow, J.Corish, P.W.M.Jacobs and A.B.Lidiard, J.Phys. C, 14 L121 (1981)

180. G.Jacucci and F.Taylor, J. Phys. F, 9 1489 (1979)

181. E.A.Colbourn and W.C.Mackrodt, Solid State Ionics, 8 221 (1983)

182. J.B.Goodenough, Supercond. Sci. Tech., 3 26 (1990)

183. S.Shamoto, M.Oneda, M.Sato, and S.Hosoya, Japan. J. Appl. Phys. Suppl. 3(Part 2), 26 1131 (1987)

184. S.-W.Cheong, J.D.Thompson and Z.Fisk, Physica C, 158 109 (1989)

185. A.Roshko, J.S.Moodara and Y.M.Chiang, Physica C, 162-164 1625

(1989)

186. D.R.Clarke, T.M.Shaw and D.Dimos, J. Am. Ceram. Soc., 72 1103 (1989)

187. E.S.Dana, 'A Textbook of Mineralogy', 4th Ed. p208, (Wiley, London, 1949)

188. Hk.Mueller-Buschbaum, Angew. Chem., int. Ed. Engl., 16 647 (1977)

189. D.C.Johnston, J.P.Stokes, D.P. Goshorn and J.T.Lewandowski, Phys. Rev. B, 153-155 4007 (1987)

190. J.C.Phillips, 'High-T_C Superconductors', Chapter III, (Academic Press, London, 1989)

191. V.B.Grande, Hk.Mueller-Buschbaum and M.Schweizer, Z. Anorg. Allg. Chem. 428 120 (1977)

192. A.W.Sleight, 'High-Temperature Superconducting Materials', p14, eds. W.E.Hatfield and J.H.Miller (Marcel Dekker, New York 1988)

193. N.L.Allan and W.C.Mackrodt, Phil. Mag. A, 58 555 (1988)

194. J.M.Longo and P.M.Raccah, J. Solid State Chem. 6 526 (1973)

195. Hk.Mueller-Buschbaum, and W.Wollsclaeger, Z. Anorg. Allg. Chem. 414 76 (1975)

196. P.W.Tasker, J. Phys. C, 12 4977 (1979)

197. F.Bertaut, Compt. Rendu., 246 3447 (1958)

198. G.C.Benson and K.S.Yun, 'The Solid Gas Interface', p203, Ed. E.A.Flood, (Arnold, London, 1967)

199. J.T.Kummer and Y.Y.Yao, Can. J. Chem., 45 421 (1967)

200. P.A.Cox and A.A.Williams, Surf. Sci., 152/3 791 (1985)

201. S.Ferrer and G.A.Somorjai, Surf. Sci. 94 41 (1980)

202. N.Brookes, A.Viesco, P.D.Johnson and J.P.Remeika, Surf. Sci. 203 1627 (1988)

203. M.J.Davies, PhD Thesis, Bath, to be submitted

204. Y.Hidaka and M.Suzuki, Nature, 338 635 (1989)

205. K.A.Kubat-Matyin, Z.Fisk and R.R.Ryan, Acta Cryst. C, 44 1518 (1988)

206. A.Migliori, W.M.Visscher, S.E.Brown, Z.Fisk, S.W.Cheong, B.Alten, E.T.Ahrens, K.A.Kubat-Martin, J.D.Maynard, Y.Huang, D.R.Kirk, K.A.Gillis, H.K.Kim and M.H.W.Chan, Phys. Rev. B, 41 2098 (1990)

207. J.Karalewski, D.Nikl and W.Assmus, Physica C, 153-155 429 (1988)

208. J.D.Thompson, S.W.Cheong, S.E.Brown, Z.Fisk, S.B.Oseroff, M.Tovar, D.C.Vier and S.Schutz Phys. Rev. B, 37 5916 (1990)

209. P.W.Tasker and D.M.Duffy, Surf. Sci. 137 91 (1984)

210. V.E.Henrich, Mat. Sci. Mon. vol.47, p23, Eds. J.Nowotny and L.-C.Dufour, (Elsevier, Oxford 1988)

211. W.C.Mackrodt, Phys. Chem. Minerals, 15 228 (1988)

212. J.W.Gibbs, 'Collected Works', (Longman, New York, 1928)

213. G.Wulff, Z. Kristallogr. Kristallgeom., 34 949 (1901)

214. W.C.Mackrodt, R.J.Davey and S.N.Black, J. Crystal Growth, 80 441 (1987)

215. M.A.Subramanian, J.Gopalkrishnan, C.C.Toradi, T.R.Askew, R.B.Flippen, A.W.Sleight, J.J.Lin and S.J.Poon, Science, 240 495 (1988)

216. B.Raveau, C.Michel, M.Hervieu, F.Deslandes and A.Maignan in 'High Temperature Superconductivity - The first Two Years' p1 ed. R.M.Metzger (Gordon and Breach Science Publishers, New York, 1989)

217. J.M.Tarascon, L.H.Greene, B.G.Baguley, W.R.McKinnon, P.Barboux and G.W.Hull, in 'Novel Superconductivity' p705 eds. S.A.Wolf and V.Z.Kresin (Plenum, New York, 1987)

218. P.M.Grant, Adv. Mater., 2 246 (1990)

219. J.Moreland, J.W.Ekin, L.F.Goodrich, T.E.Capobianco, A.F.Clark, J.Kwo,

M.Hong, S.H.Liou, Phys. Rev. B, 35 8856 (1987)

220. T.Seiyama, Mat. Sci. Mon., vol47, eds. J.Nowotny and L.-C. Dufour, p189, (Elsevier, Amsterdam, 1988)

221. W.C.Mackrodt and R.F.Stewart, J.Phys. C, 10 1431 (1977)

222. D.M.Duffy and A.M.Stoneham, J.Phys. C, 17 L195 (1984)

223. W.C.Mackrodt, J. Chem. Soc. Farad. Trans. 2, 85 541 (1989)

224. N.L.Allan and W.C.Mackrodt, Phil. Mag. A, 58 555 (1988)

225. D.M.Duffy, J.P.Hoare and P.W.Tasker, J.Phys. C, 15 5691 (1982)

226. P.J.Lawrence, S.C.Parker and P.W.Tasker, J. Am. Ceram. Soc., 71 C389 (1988)

227. P.R.Kenway, S.C.Parker and W.C.Mackrodt, Molecular Simulation 4 175 (1989)

228. N.L.Allan and W.C.Mackrodt, J. Am. Ceram. Soc., in press

229. T.Takahashi, F.Maeda, H. Katayama-Yoshida, Y.Okabe, T.Suzuki, A.Fujimori, S.Hosoya, S.Shamoto and M.Sato, Phys. Rev. B, 37 9788 (1988)

230. J.H.Weaver, H.M.Meyer, T.J.Wagener, D.M.Hill Y.Gao, D.Peterson, Z.Fisk and A.J.Arko, Phys. Rev. B 38 4668 (1988)

231. J.M.Tarascon, L.H.Greene, W.R. Mckonnon, G.W. Hull, and T.H.Geballe Science, 235 1373 (1987)

232. J.M.Tarascon, E.Wang, L.H.Greene, B.G.Bagley, G.W.Hull, S.M.D'Egiodio, P.F.Miceli, Z.Z.Wang, T.W.Jing, J.Clayhold, D.Brauner and N.P.Ong, Phys. Rev. B, 40 4494 (1989)

233. D.M.Duffy and P.W.Tasker, J.Appl.Phys. 56 971 (1984)

234. M.-Y.Su, E.A.Cooper, C.E.Elsbernd, and T.O.Mason, J. Am. Ceram., in press

235. X.Zhang C.R.A.Catlow and W.Zhou, Physica C, 168 417 (1990)

236. J.C.Phillips, 'Physics of High-T_C Superconductors', Chapter VIII

(Academic Press Inc. Ltd., London, 1989)

237. J.Yu, A.J.Freeman, and J.H.Xu, Phys. Rev. Lett., 58 1035 (1987)

238. L.F.Matthiess, Phys. Rev. Lett., 58 1028 (1987)

239. D.W.Bullett and W.G.Dawson, J. Phys. Rev., 20 1853 (1987)

240. M.W.Shafer, T.Penny and B.L.Olson Phys. Rev. B, 36 4047 (1987)

241. N.L.Allan and W.C.Mackrodt, Phil. Mag. Lett., 60 183 (1989)

242. W.C.Mackrodt, 'Ceramic Microstructures', eds. A.G.Evans and J.Pask, p271 (Plenum, New York, 1987)

243. G.V.Lewis and C.R.A.Catlow, J. Chem. Solids, 47 89 (1986)

244. T.Hasagawa, K.Kisho, M.Aoki, N.Ooba, K. Kitazawa, S.Uchida, S.Tamaka, Japan J. Appl. Phys., 26 L337 (1987)

245. R.C.Baetzold, Phys. Rev. B, 38 11304 (1988)

246. M.S.Islam and R.C.Baetzold, Phys. Rev. B, 40 10926 (1989)

247. J.Frenkel, 'Kinetic Theory of Liquids', p36, (Oxford University Press, New York, 1946)

248. W.D.Kingery, J. Am. Ceram. Soc. 57 1 (1974)

249. K.L.Kliewer and J.S.Koehler, Phys. Rev. A, 40 1226 (1965)

250. M.F.Yan, R.M.Cannon and H.K.Bowen, J. Appl. Phys., 54 764 (1983)

251. K.L.Kliewer Phys. Rev. A, 40 1241 (1965)

252. M.F.Yan, R.M.Cannon and H.K.Bowen, J. Appl. Phys., 54 779 (1983)

253. J.W.Rogers, N.D.Shinn, J.E.Schirber, E.L.Venturini, D.S.Ginley and B.Morosin, Phys. Rev. B, 38 5021 (1988)

254. D.M.Duffy and P.W.Tasker, Phil. Mag. A, 50 155 (1984)

255. R.G.Egdell, W.R.Flavell and M.S.Golden, Supercond. Sci. 3 8 (1990)

256. Y.M.Chiang, D.A.Rudman, D.K.Leung, J.A.S.Ikeda, A.Roshko and B.D.Fabes, Physica C, 152 77 (1988)

257. A.Roshko, Private communication

258. D.Bingham, P.W.Tasker and A.N.Cormack, Phil. Mag. A, 60 1 (1989)

Appendix 1

Non-Empirical Potentials used in Chapter 4

Energies in eV and distances in Å

Al^{3+} shell Al^{3+} shell

5.5670480728	1.0583543777
1.9018163681	1.1906480789
0.6267266273	1.3229427338
0.1989530325	1.4552364349
0.0602402575	1.5875310898
0.0168372579	1.7198257446
0.0038457250	1.8521194458
0.0002095541	1.9844141006
-0.0006822753	2.1167078018
-0.0008281469	2.2490024567
-0.0008001158	2.3812961578
-0.0007484076	2.5135908127
-0.0007013259	2.6458854675
-0.0006624085	2.7781791687
-0.0006294786	2.9104738235
-0.0006017198	3.0427675247
-0.0005753213	3.1750621796
-0.0005309612	3.4396505356
-0.0004928606	3.7042388916
-0.0004602026	3.9688272476
-0.0004313551	4.2334165573
0.0000000000	4.4980049133

Al^{3+} shell O^{2-} shell

375.3889160156	0.5291770101
45.5217742920	1.0583543777
27.4393615723	1.1906480789
16.5209045410	1.3229427338
9.9241685867	1.4552364349
5.9452943802	1.5875310898
3.5532150269	1.7198257446
2.1202993393	1.8521194458
1.2644119263	1.9844141006
0.7540940046	2.1167078018
0.4499310851	2.2490024567
0.2685672045	2.3812961578
0.1603066921	2.5135908127
0.0956229568	2.6458854675
0.0569506772	2.7781791687
0.0338350087	2.9104738235
0.0200335532	3.0427675247
0.0118117779	3.1750621796
0.0040404648	3.4396505356
0.0013428195	3.7042388916
0.0004250517	3.9688272476
0.0001258957	4.2334165573

0.0000000000 4.4980049133

O^{2-} shell O^{2-} shell

23.8096771240 1.0583543777
17.5060272217 1.1906480789
13.0766620636 1.3229427338
9.7808971405 1.4552364349
7.2644815445 1.5875310898
5.3352394104 1.7198257446
3.8685264587 1.8521194458
2.7687892914 1.9844141006
1.9568386078 2.1167078018
1.3664588928 2.2490024567
0.9432928562 2.3812961578
0.6439008117 2.5135908127
0.4346213341 2.6458854675
0.2899468541 2.7781791687
0.1909908056 2.9104738235
0.1240097284 3.0427675247
0.0791572928 3.1750621796
0.0300666504 3.4396505356
0.0097075216 3.7042388916
0.0019627323 3.9688272476
-0.0005347712 4.2334165573
0.0000000000 4.4980049133

Al^{3+} shell Ca^{2+} shell

485.5278320313 0.5291770101
35.1964569092 1.0583543777
17.7159423828 1.1906480789
8.6284055710 1.3229427338
4.0824546814 1.4552364349
1.8831586838 1.5875310898
0.8486286402 1.7198257446
0.3735997677 1.8521194458
0.1601703167 1.9844141006
0.0662945509 2.1167078018
0.0259211659 2.2490024567
0.0090129972 2.3812961578
0.0021734592 2.5135908127
-0.0004522044 2.6458854675
-0.0013727262 2.7781791687
-0.0016341626 2.9104738235
-0.0016598753 3.0427675247
-0.0016106572 3.1750621796
-0.0014802057 3.4396505356
-0.0013657236 3.7042388916
-0.0012712148 3.9688272476
-0.0011905967 4.2334165573
0.0000000000 4.4980049133

O^{2-} shell Ca^{2+} shell

490.7390136719	0.5291770101
59.2502441406	1.0583543777
38.7875976563	1.1906480789
25.5459899902	1.3229427338
16.7957000732	1.4552364349
10.9786043167	1.5875310898
7.1187200546	1.7198257446
4.5738086700	1.8521194458
2.9108095169	1.9844141006
1.8351745605	2.1167078018
1.1465997696	2.2490024567
0.7102253437	2.3812961578
0.4362245798	2.5135908127
0.2656456232	2.6458854675
0.1602936387	2.7781791687
0.0957335234	2.9104738235
0.0564855039	3.0427675247
0.0328349285	3.1750621796
0.0104196072	3.4396505356
0.0028666721	3.7042388916
0.0005524794	3.9688272476
-0.0000362774	4.2334165573
0.0000000000	4.4980049133

Ca^{2+} shell Ca^{2+} shell

67.6298065186	1.0583543777
40.4976348877	1.1906480789
24.2686157227	1.3229427338
14.2970285416	1.4552364349
8.2177648544	1.5875310898
4.5996284485	1.7198257446
2.5078716278	1.8521194458
1.3329811096	1.9844141006
0.6908536553	2.1167078018
0.3487377167	2.2490024567
0.1709182858	2.3812961578
0.0807779431	2.5135908127
0.0363026559	2.6458854675
0.0150337331	2.7781791687
0.0052638873	2.9104738235
0.0010227326	3.0427675247
-0.0006526113	3.1750621796
-0.0012875327	3.4396505356
-0.0011081873	3.7042388916
-0.0009351010	3.9688272476
-0.0008281469	4.2334165573
0.0000000000	4.4980049133

Appendix 2

Non-Empirical Potentials used in Chapter 5

Energies in eV and distance in Å

Cu^{2+} shell Cu^{2+} shell

75.2947387695	1.0583543777
37.6233673096	1.1906480789
18.8722229004	1.3229427338
9.5023002625	1.4552364349
4.7951889038	1.5875310898
2.4194688797	1.7198257446
1.2172746658	1.8521194458
0.6087278128	1.9844141006
0.3014336824	2.1167078018
0.1470565200	2.2490024567
0.0701581836	2.3812961578
0.0323360935	2.5135908127
0.0140844770	2.6458854675
0.0016707175	2.9104738235
0.0000000000	3.1750621796

Cu^{2+} shell La^{3+} shell

2093.5678710938	0.5291770101
150.6905364990	1.0583543777
87.6615142822	1.1906480789
51.7414550781	1.3229427338
30.3836975098	1.4552364349
17.5530548096	1.5875310898
9.9435625076	1.7198257446
5.5326652527	1.8521194458
3.0345735550	1.9844141006
1.6464605331	2.1167078018
0.8856495023	2.2490024567
0.4725876451	2.3812961578
0.2498361468	2.5135908127
0.1304435730	2.6458854675
0.0668668151	2.7781791687
0.0333424844	2.9104738235
0.0158979483	3.0427675247
0.0070373528	3.1750621796
0.0006601114	3.4396505356
-0.0004526288	3.7042388916
-0.0003942284	3.9688272476
-0.0002038281	4.2334165573
0.0000000000	4.4980049133

Cu^{2+} shell O^{2-} shell

579.7153320313	0.2997787595
72.8338775635	0.8289555907
45.8854827881	0.9612498283

28.9237060547	1.0935440063
18.1938171387	1.2258386612
11.4012012482	1.3581323624
7.1117057800	1.4904270172
4.4149131775	1.6227207184
2.7280168533	1.7550153732
1.6781902313	1.8873100281
1.0277967453	2.0196037292
0.6265239716	2.1518983841
0.3798806667	2.2841920853
0.2288821340	2.4164867401
0.1368171573	2.5487804413
0.0809706450	2.6810750961
0.0473022312	2.8133697510
0.0271694325	2.9456634521
0.0082968399	3.2102518082
0.0020770777	3.4748411179
0.0002537973	3.7394294739
-0.0001569533	4.0040178299
0.0000000000	4.2686061859

La^{3+} shell La^{3+} shell

267.5600585938	1.0583543777
156.3569030762	1.1906480789
93.3763427734	1.3229427338
56.6985015869	1.4552364349
34.9430999756	1.5875310898
21.7873382568	1.7198257446
13.6443386078	1.8521194458
8.4980897903	1.9844141006
5.2166566849	2.1167078018
3.1378688812	2.2490024567
1.8453435898	2.3812961578
1.0615272522	2.5135908127
0.5984259844	2.6458854675
0.3311707377	2.7781791687
0.1800058484	2.9104738235
0.0958366990	3.0427675247
0.0496814586	3.1750621796
0.0115325451	3.4396505356
0.0014402079	3.7042388916
-0.0005979096	3.9688272476
-0.0006428140	4.2334165573
0.0000000000	4.4980049133

La^{3+} shell O^{2-} shell

931.0944824219	0.5926781893
99.0900268555	1.1218547821
62.9529876709	1.2541494370
41.2384338379	1.3864440918
27.5127563477	1.5187377930
18.4745025635	1.6510324478
12.3812484741	1.7833261490

8.2416896820	1.9156208038
5.4359560013	2.0479145050
3.5487060547	2.1802091599
2.2920160294	2.3125038147
1.4644422531	2.4447975159
0.9255762696	2.5770921707
0.5785463452	2.7093858719
0.3573981524	2.8416805267
0.2178830504	2.9739751816
0.1307314038	3.1062688828
0.0768595934	3.2385635376
0.0241122134	3.5031518936
0.0056338347	3.7677402496
-0.0000559564	4.0323286057
-0.0012687140	4.2969169617
0.0000000000	4.5615053177

O^{2-} shell O^{2-} shell

23.8096771240	0.7702169418
17.5060272217	0.9025111794
13.0766620636	1.0348052979
9.7808971405	1.1670999527
7.2644815445	1.2993936539
5.3352394104	1.4316883087
3.8685264587	1.5639820099
2.7687892914	1.6962766647
1.9568386078	1.8285713196
1.3664588928	1.9608650208
0.9432928562	2.0931596756
0.6439008117	2.2254533768
0.4346213341	2.3577480316
0.2899468541	2.4900426865
0.1909908056	2.6223363876
0.1240097284	2.7546310425
0.0791572928	2.8869247437
0.0300666504	3.1515130997
0.0097075216	3.4161024094
0.0019627323	3.6806907654
-0.0005347712	3.9452791214
0.0000000000	4.2098674774

Nd^{3+} shell Nd^{3+} shell

189.6097259521	1.0583543777
99.4454498291	1.1906480789
52.0159912109	1.3229427338
26.9907684326	1.4552364349
13.7416744232	1.5875310898
6.7681980133	1.7198257446
3.1861257553	1.8521194458
1.4242277145	1.9844141006
0.6047251225	2.1167078018
0.2458956242	2.2490024567
0.0975218415	2.3812961578

0.0389394984	2.5135908127
0.0164037310	2.6458854675
0.0076070800	2.7781791687
0.0040223487	2.9104738235
0.0023671442	3.0427675247
0.0015689339	3.1750621796
0.0008278743	3.4396505356
0.0004354371	3.7042388916
0.0001273653	3.9688272476
-0.0000468095	4.2334165573
0.0000000000	4.4980049133

Nd^{3+} shell O^{2-} shell

899.5068359375	0.6191371083
104.4732971191	1.1483144760
66.2998657227	1.2806081772
42.3114013672	1.4129028320
26.9106140137	1.5451965332
16.9915008545	1.6774911880
10.6402997971	1.8097858429
6.6090049744	1.9420795441
4.0735521317	2.0743741989
2.4930191040	2.2066679001
1.5160570145	2.3389625549
0.9168472886	2.4712562561
0.5517900586	2.6035509109
0.3305780292	2.7358455658
0.1971038580	2.8681392670
0.1168470383	3.0004339218
0.0687398911	3.1327276230
0.0400233120	3.2650222778
0.0129268616	3.5296106339
0.0037546861	3.7941989899
0.0009088195	4.0587873459
0.0001380063	4.3233766556
0.0000000000	4.5879650116

Nd^{3+} shell Cu^{2+} shell

2033.3408203125	0.5291770101
119.6591186523	1.0583543777
62.6959838867	1.1906480789
32.3711547852	1.3229427338
16.3232727051	1.4552364349
8.0421819687	1.5875310898
3.8904428482	1.7198257446
1.8576784134	1.8521194458
0.8786126971	1.9844141006
0.4121308923	2.1167078018
0.1916331649	2.2490024567
0.0881729126	2.3812961578
0.0400215462	2.5135908127
0.0178333633	2.6458854675
0.0077146105	2.7781791687

0.0031821518	2.9104738235
0.0011792313	3.0427675247
0.0003459139	3.1750621796
-0.0000998131	3.4396505356
-0.0001118665	3.7042388916
-0.0000677050	3.9688272476
-0.0000281864	4.2334165573
0.0000000000	4.4980049133

Appendix 3

Non-Empirical Potentials used for Impurity Interactions in Chapter 6

Energies in eV and distances in Å

Ba^{2+} shell Ba^{2+} shell

276.6674804688	1.0583543777
164.5711517334	1.1906480789
100.3873138428	1.3229427338
62.2913208008	1.4552364349
39.2861022949	1.5875310898
25.1851501465	1.7198257446
16.3437194824	1.8521194458
10.6539793015	1.9844141006
6.9210090637	2.1167078018
4.4530229568	2.2490024567
2.8257484436	2.3812961578
1.7630720139	2.5135908127
1.0787925720	2.6458854675
0.6456947923	2.7781791687
0.3769879937	2.9104738235
0.2139165401	3.0427675247
0.1174005866	3.1750621796
0.0307195336	3.4396505356
0.0053825453	3.7042388916
-0.0005266068	3.9688272476
-0.0011666992	4.2334165573
0.0000000000	4.4980049133

Ba^{2+} shell O^{2-} shell

887.2707519531	0.6164911389
92.5080718994	1.1456680298
58.6659240723	1.2779626846
38.5836486816	1.4102563858
26.0233917236	1.5425510406
17.7833709717	1.6748447418
12.1989889145	1.8071393967
8.3480396271	1.9394340515
5.6750564575	2.0717277527
3.8214731216	2.2040224075
2.5442285538	2.3363161087
1.6728115082	2.4686107635
1.0854082108	2.6009054184
0.6946231127	2.7331991196
0.4381209612	2.8654937744
0.2719913125	2.9977874756
0.1658308506	3.1300821304
0.0989325047	3.2623758316
0.0320368186	3.5269651413
0.0080413483	3.7915534973
0.0004615195	4.0561418533
-0.0012906000	4.3207302094

0.0000000000 4.5853185654

Ba^{2+} shell Cu^{2+} shell

2096.0612792969 0.5291770101
157.8134002686 1.0583543777
93.6735229492 1.1906480789
56.8845367432 1.3229427338
34.6336669922 1.4552364349
20.8932037354 1.5875310898
12.4314613342 1.7198257446
7.2868394852 1.8521194458
4.2061042786 1.9844141006
2.3894901276 2.1167078018
1.3350172043 2.2490024567
0.7329009175 2.3812961578
0.3948392272 2.5135908127
0.2082968950 2.6458854675
0.1071261168 2.7781791687
0.0532945618 2.9104738235
0.0252512284 3.0427675247
0.0110688880 3.1750621796
0.0010413884 3.4396505356
-0.0006130466 3.7042388916
-0.0005131573 3.9688272476
-0.0002825197 4.2334165573
0.0000000000 4.4980049133

Ba^{2+} shell La^{3+} shell

3588.3527832031 0.5291770101
274.0480957031 1.0583543777
161.8529663086 1.1906480789
97.8372497559 1.3229427338
60.1419525146 1.4552364349
37.5552673340 1.5875310898
23.7862548828 1.7198257446
15.1948204041 1.8521194458
9.7051792145 1.9844141006
6.1456327438 2.1167078018
3.8346500397 2.2490024567
2.3493032455 2.3812961578
1.4106359482 2.5135908127
0.8292365074 2.6458854675
0.4766635895 2.7781791687
0.2674656510 2.9104738235
0.1460217237 3.0427675247
0.0771741271 3.1750621796
0.0186056644 3.4396505356
0.0027139345 3.7042388916
-0.0006533270 3.9688272476
-0.0008531222 4.2334165573
0.0000000000 4.4980049133

Ba^{2+} shell Nd^{3+} Shell

3359.0737120601	0.5291770000
243.5714843993	1.0583540000
142.9796889336	1.1906482500
85.2881959843	1.3229425000
51.4124667816	1.4552367500
31.1607832156	1.5875310000
18.8334924063	1.7198252500
11.2455697919	1.8521195000
6.5875524060	1.9844137500
3.7725473269	2.1167080000
2.1100536358	2.2490022500
1.1527467963	2.3812965000
0.6151719327	2.5135907500
0.3205894790	2.6458850000
0.1630045190	2.7781792500
0.0808054241	2.9104735000
0.0389449503	3.0427677500
0.0182170555	3.1750620000
0.0034935663	3.4396505000
0.0003995135	3.7042390000
-0.0001698205	3.9688275000
-0.0002237058	4.2334160000
0.0000000000	4.4980045000

Ca^{2+} shell Cu^{2+} shell

973.5700574989	0.5291770000
77.1427244621	1.0583540000
42.9273668374	1.1906482500
23.4458610156	1.3229425000
12.5788855514	1.4552367500
6.6453071505	1.5875310000
3.4633886161	1.7198252500
1.7822652929	1.8521195000
0.9052418972	1.9844137500
0.4531291854	2.1167080000
0.2228463680	2.2490022500
0.1071262362	2.3812965000
0.0499019085	2.5135907500
0.0221795332	2.6458850000
0.0091087999	2.7781792500
0.0031882160	2.9104735000
0.0006651302	3.0427677500
-0.0002917429	3.1750620000
-0.0005815807	3.4396505000
-0.0004204690	3.7042390000
-0.0002971858	3.9688275000
-0.0002302374	4.2334160000
0.0000000000	4.4980045000

Ca^{2+} shell Ca^{2+} shell

67.6298234049	1.0583540000
40.4976596402	1.1906482500

24.2686226888	1.3229425000
14.2970313701	1.4552367500
8.2177671445	1.5875310000
4.5996293526	1.7198252500
2.5078730560	1.8521195000
1.3329810172	1.9844137500
0.6908538949	2.1167080000
0.3487377663	2.2490022500
0.1709183162	2.3812965000
0.0807779371	2.5135907500
0.0363026635	2.6458850000
0.0150337382	2.7781792500
0.0052638903	2.9104735000
0.0010227329	3.0427677500
-0.0006526114	3.1750620000
-0.0012875331	3.4396505000
-0.0011081874	3.7042390000
-0.0009351012	3.9688275000
-0.0008281469	4.2334160000
0.0000000000	4.4980045000

Ca^{2+} shell O^{2-} shell

490.7392661540	0.5774908601
59.2502625286	1.1066678601
38.7876205718	1.2389621101
25.5459953942	1.3712563601
16.7957047286	1.5035506101
10.9786068416	1.6358448601
7.1187230784	1.7681391101
4.5738101095	1.9004333601
2.9108113114	2.0327276101
1.8351747111	2.1650218601
1.1466003294	2.2973161101
0.7102256752	2.4296103601
0.4362247005	2.5619046101
0.2656457531	2.6941988601
0.1602936509	2.8264931101
0.0957335687	2.9587873601
0.0564854454	3.0910816101
0.0328349512	3.2233758601
0.0104197377	3.4879643601
0.0028668090	3.7525528601
0.0005524608	4.0171413601
-0.0000361957	4.2817298601
0.0000000000	4.5463183601

Ca^{2+} shell La^{3+} shell

1675.2612131102	0.5291770000
134.3829943520	1.0583540000
78.2342820037	1.1906482500
46.8495461377	1.3229425000
28.6475809538	1.4552367500
17.6208964130	1.5875310000

10.7375676392	1.7198252500
6.4154045242	1.8521195000
3.7407778358	1.9844137500
2.1276477442	2.1167080000
1.1823203236	2.2490022500
0.6433523334	2.3812965000
0.3433935923	2.5135907500
0.1798763460	2.6458850000
0.0923015079	2.7781792500
0.0461677632	2.9104735000
0.0222693421	3.0427677500
0.0101503110	3.1750620000
0.0013637346	3.4396505000
-0.0003129704	3.7042390000
-0.0003690329	3.9688275000
-0.0001954024	4.2334160000
0.0000000000	4.4980045000

Ca^{2+} shell Nd^{3+} shell

1519.6537213488	0.5291770000
113.6842186639	1.0583540000
63.6931960293	1.1906482500
35.9355377511	1.3229425000
20.0599429196	1.4552367500
10.9195996711	1.5875310000
5.7523492062	1.7198252500
2.9265406603	1.8521195000
1.4391952849	1.9844137500
0.6851943012	2.1167080000
0.3159874531	2.2490022500
0.1408745168	2.3812965000
0.0602944315	2.5135907500
0.0243371240	2.6458850000
0.0088124305	2.7781792500
0.0024025242	2.9104735000
-0.0000987898	3.0427677500
-0.0009628603	3.1750620000
-0.0012363692	3.4396505000
-0.0012189517	3.7042390000
-0.0012524260	3.9688275000
-0.0012584132	4.2334160000
0.0000000000	4.4980045000

Ce^{4+} shell Ce^{4+} shell

254.6559448242	1.0583543777
145.6989135742	1.1906480789
84.8994293213	1.3229427338
50.2344360352	1.4552364349
30.0787353516	1.5875310898
18.0928649902	1.7198257446
10.8197736740	1.8521194458
6.3650932312	1.9844141006
3.6544542313	2.1167078018

2.0389757156	2.2490024567
1.1043643951	2.3812961578
0.5813391805	2.5135908127
0.2980797291	2.6458854675
0.1491257548	2.7781791687
0.0728350282	2.9104738235
0.0345881209	3.0427675247
0.0158686787	3.1750621796
0.0027993154	3.4396505356
0.0003156918	3.7042388916
0.0000552461	3.9688272476
0.0000677649	4.2334165573
0.0000000000	4.4980049133

Ce^{4+} shell Cu^{2+} shell

2092.3388671875	0.5291770101
143.9192199707	1.0583543777
81.9971923828	1.1906480789
47.0006103516	1.3229427338
26.6300811768	1.4552364349
14.7860383987	1.5875310898
8.0310659409	1.7198257446
4.2761468887	1.8521194458
2.2395114899	1.9844141006
1.1570415497	2.1167078018
0.5905717015	2.2490024567
0.2976673841	2.3812961578
0.1477407813	2.5135908127
0.0717937946	2.6458854675
0.0337694995	2.7781791687
0.0150688365	2.9104738235
0.0060819648	3.0427675247
0.0019608270	3.1750621796
-0.0004476837	3.4396505356
-0.0005619859	3.7042388916
-0.0004014184	3.9688272476
-0.0003355586	4.2334165573
0.0000000000	4.4980049133

Ce^{4+} shell O^{2-} shell

973.8674316406	0.5635732412
105.0317993164	1.0927505493
66.6914367676	1.2250442505
43.3989562988	1.3573389053
28.5843811035	1.4896326065
18.8650817871	1.6219272614
12.3959283829	1.7542219162
8.0815858841	1.8865156174
5.2191352844	2.0188102722
3.3365650177	2.1511039734
2.1112365723	2.2833986282
1.3223466873	2.4156932831
0.8199484944	2.5479869843

0.5033265352	2.6802816391
0.3057281375	2.8125753403
0.1835451126	2.9448699951
0.1086613536	3.0771636963
0.0631974339	3.2094583511
0.0196621567	3.4740467072
0.0048123971	3.7386350632
0.0003080717	4.0032234192
-0.0006762883	4.2678127289
0.0000000000	4.5324010849

Ce^{4+} shell La^{3+} shell

3614.3749162480	0.5291770000
262.6858097884	1.0583540000
152.1038431750	1.1906482500
89.8399735207	1.3229425000
53.9212757552	1.4552367500
32.8110364975	1.5875310000
20.1371668735	1.7198252500
12.3540236539	1.8521195000
7.4985404401	1.9844137500
4.4654159348	2.1167080000
2.5963721094	2.2490022500
1.4719687306	2.3812965000
0.8145942339	2.5135907500
0.4410626789	2.6458850000
0.2341100373	2.7781792500
0.1219046994	2.9104735000
0.0620846222	3.0427677500
0.0307372330	3.1750620000
0.0064420198	3.4396505000
0.0006999651	3.7042390000
-0.0002694267	3.9688275000
-0.0002433005	4.2334160000
0.0000000000	4.4980045000

Ce^{4+} shell Nd^{3+} shell

3357.3046875000	0.5291770101
223.2038879395	1.0583543777
125.4153747559	1.1906480789
71.1031646729	1.3229427338
40.4668426514	1.4552364349
22.9531555176	1.5875310898
12.8438711166	1.7198257446
7.0170497894	1.8521194458
3.7152662277	1.9844141006
1.9002895355	2.1167078018
0.9398964643	2.2490024567
0.4515287876	2.3812961578
0.2121350169	2.5135908127
0.0982667208	2.6458854675
0.0451912843	2.7781791687
0.0207719766	2.9104738235

0.0095347092	3.0427675247
0.0044156052	3.1750621796
0.0010510359	3.4396505356
0.0004373419	3.7042388916
0.0003124261	3.9688272476
0.0002147249	4.2334165573
0.0000000000	4.4980049133

Mg^{2+} shell Cu^{2+} shell

31.6174595805	1.0583540000
14.7872391134	1.1906482500
6.8930885522	1.3229425000
3.2083566424	1.4552367500
1.4906723871	1.5875310000
0.6901550184	1.7198252500
0.3174796416	1.8521195000
0.1445267455	1.9844137500
0.0647462315	2.1167080000
0.0283001460	2.2490022500
0.0118926037	2.3812965000
0.0046621706	2.5135907500
0.0015779152	2.6458850000
0.0000000000	2.7781792500

Mg^{2+} shell La^{3+} shell

1022.7375779451	0.5291770000
77.7190205702	1.0583540000
44.9190542446	1.1906482500
25.8804598044	1.3229425000
14.6070881698	1.4552367500
8.0127957418	1.5875310000
4.2714521099	1.7198252500
2.2231521641	1.8521195000
1.1376564513	1.9844137500
0.5766079899	2.1167080000
0.2912418346	2.2490022500
0.1471967914	2.3812965000
0.0745460157	2.5135907500
0.0378005671	2.6458850000
0.0191486188	2.7781792500
0.0096955514	2.9104735000
0.0049373125	3.0427677500
0.0025987431	3.1750620000
0.0009927966	3.4396505000
0.0007108511	3.7042390000
0.0006493456	3.9688275000
0.0005696062	4.2334160000
0.0000000000	4.4980045000

Mg^{2+} shell Mg^{2+} shell

11.4674350657	1.0583540000
4.7367852365	1.1906482500

1.9058026093	1.3229425000
0.7484842677	1.4552367500
0.2870929355	1.5875310000
0.1074087261	1.7198252500
0.0390772143	1.8521195000
0.0137804957	1.9844137500
0.0047274862	2.1167080000
0.0016386043	2.2490022500
0.0006607758	2.3812965000
0.0003891719	2.5135907500
0.0003317486	2.6458850000
0.0003254892	2.7781792500
0.0003246728	2.9104735000
0.0003205906	3.0427677500
0.0003146033	3.1750620000
0.0002960972	3.4396505000
0.0002767747	3.7042390000
0.0002588129	3.9688275000
0.0002427562	4.2334160000
0.0000000000	4.4980045000

Mg^{2+} shell O^{2-} shell

43.2804102601	1.0748643224
26.6829401780	1.2071585724
16.4046168940	1.3394528224
10.0436986145	1.4717470724
6.1201430608	1.6040413224
3.7122335729	1.7363355724
2.2428165037	1.8686298224
1.3509144943	2.0009240724
0.8118814607	2.1332183224
0.4871011717	2.2655125724
0.2918073586	2.3978068224
0.1745114888	2.5301010724
0.1041282518	2.6623953224
0.0619384787	2.7946895724
0.0366896582	2.9269838224
0.0216172750	3.0592780724
0.0126535301	3.1915723224
0.0042272778	3.4561608224
0.0013514879	3.7207493224
0.0004003300	3.9853378224
0.0001015113	4.2499263224
0.0000000000	4.5145148224

Mg^{2+} shell Nd^{3+} shell

966.8961421307	0.5291770000
53.2912739234	1.0583540000
26.3599098019	1.1906482500
12.5521271249	1.3229425000
5.6995227932	1.4552367500
2.4655640819	1.5875310000
1.0202963545	1.7198252500

0.4066982548	1.8521195000
0.1576731360	1.9844137500
0.0603279057	2.1167080000
0.0233388845	2.2490022500
0.0095015098	2.3812965000
0.0043056565	2.5135907500
0.0023029180	2.6458850000
0.0014862013	2.7781792500
0.0011468325	2.9104735000
0.0009930687	3.0427677500
0.0009277532	3.1750620000
0.0008371278	3.4396505000
0.0006833641	3.7042390000
0.0004827909	3.9688275000
0.0003382802	4.2334160000
0.0000000000	4.4980045000

Sr^{2+} shell Cu^{2+} shell

1558.9873046875	0.5291770101
111.4207000732	1.0583543777
64.3996429443	1.1906480789
37.1241912842	1.3229427338
21.1350555420	1.4552364349
11.8605403900	1.5875310898
6.5650053024	1.7198257446
3.5860099792	1.8521194458
1.9320363998	1.9844141006
1.0252008438	2.1167078018
0.5344932079	2.2490024567
0.2728770971	2.3812961578
0.1357787848	2.5135908127
0.0654002428	2.6458854675
0.0301509909	2.7781791687
0.0130522028	2.9104738235
0.0050905980	3.0427675247
0.0016196026	3.1750621796
-0.0001826196	3.4396505356
-0.0001667751	3.7042388916
-0.0000126631	3.9688272476
0.0000500916	4.2334165573
0.0000000000	4.5

Sr^{2+} shell La^{3+} shell

2608.9443359375	0.5291770101
201.5770111084	1.0583543777
118.0174560547	1.1906480789
70.1389160156	1.3229427338
42.3998870850	1.4552364349
26.0368347168	1.5875310898
16.1154785156	1.7198257446
9.9450016022	1.8521194458
6.0621871948	1.9844141006
3.6299095154	2.1167078018

2.1301746368	2.2490024567
1.2246789932	2.3812961578
0.6898554564	2.5135908127
0.3805885911	2.6458854675
0.2052853703	2.7781791687
0.1079031229	2.9104738235
0.0549057648	3.0427675247
0.0267804153	3.1750621796
0.0051015019	3.4396505356
0.0003179698	3.7042388916
-0.0002872196	3.9688272476
-0.0001545148	4.2334165573
0.0000000000	4.4980049133

Sr^{2+} shell O^{2-} shell

694.8359375000	0.5987638831
78.8980255127	1.1279411316
50.9216156006	1.2602348328
33.5304412842	1.3925294876
22.2564849854	1.5248241425
14.7832355499	1.6571178436
9.7836074829	1.7894124985
6.4336090088	1.9217061996
4.1961450577	2.0540008545
2.7113237381	2.1862945557
1.7343358994	2.3185892105
1.0977716446	2.4508838654
0.6872818470	2.5831775665
0.4253656864	2.7154722214
0.2600100636	2.8477659225
0.1567389965	2.9800605774
0.0929651856	3.1123542786
0.0540639646	3.2446489334
0.0168066658	3.5092372894
0.0042458847	3.7738256454
0.0005132034	4.0384149551
-0.0003206204	4.3030033112
0.0000000000	4.5675916672

Sr^{2+} shell Sr^{2+} shell

151.7082214355	1.0583543777
87.8962707520	1.1906480789
52.1175994873	1.3229427338
31.5668334961	1.4552364349
19.3137969971	1.5875310898
11.7894468307	1.7198257446
7.1179580688	1.8521194458
4.2316284180	1.9844141006
2.4719524384	2.1167078018
1.4169225693	2.2490024567
0.7955942750	2.3812961578
0.4364740849	2.5135908127
0.2330795527	2.6458854675

0.1204628348	2.7781791687
0.0597514771	2.9104738235
0.0280391499	3.0427675247
0.0121448785	3.1750621796
0.0012714760	3.4396505356
-0.0003638621	3.7042388916
-0.0002590851	3.9688272476
-0.0000655877	4.2334165573
0.0000000000	4.4980049133

Sr^{2+} shell Nd^{3+} shell

2440.3663159425	0.5291770000
172.3830284041	1.0583540000
97.1834074544	1.1906482500
55.5676408559	1.3229425000
32.0506272404	1.4552367500
18.4256386102	1.5875310000
10.4273382975	1.7198252500
5.7622853366	1.8521195000
3.0998604122	1.9844137500
1.6230942533	2.1167080000
0.8276655114	2.2490022500
0.4109668992	2.3812965000
0.1983927646	2.5135907500
0.0928482536	2.6458850000
0.0419481055	2.7781792500
0.0182668586	2.9104735000
0.0076743068	3.0427677500
0.0032116208	3.1750620000
0.0007846032	3.4396505000
0.0004261841	3.7042390000
0.0002370411	3.9688275000
0.0000971569	4.2334160000
0.0000000000	4.4980045000

Th^{4+} shell O^{2-} shell

1219.7417839548	0.5500794915
122.7710521354	1.0792564915
76.5718802988	1.2115507415
49.3450636658	1.3438449915
32.5998280025	1.4761392415
21.8580096807	1.6084334915
14.7443757735	1.7407277415
9.9409362745	1.8730219915
6.6676401753	2.0053162415
4.4342987830	2.1376104915
2.9174637018	2.2699047415
1.8961740064	2.4021989915
1.2162626459	2.5344932415
0.7693710970	2.6667874915
0.4795460658	2.7990817415
0.2941432065	2.9313759915
0.1771349973	3.0636702415

0.1043179391	3.1959644915
0.0326798268	3.4605529915
0.0075121065	3.7251414915
-0.0002354082	3.9897299915
-0.0018530570	4.2543184915
0.0000000000	4.5189069915

Th^{4+} shell Th^{4+} shell

6408.2375307767	0.5291770000
448.1170644377	1.0583540000
258.9436782794	1.1906482500
153.3548742924	1.3229425000
92.4495015892	1.4552367500
56.5580754918	1.5875310000
35.1068817809	1.7198252500
22.0737197055	1.8521195000
13.9862889964	1.9844137500
8.8667536395	2.1167080000
5.5847173624	2.2490022500
3.4741167794	2.3812965000
2.1243077973	2.5135907500
1.2716747279	2.6458850000
0.7423384513	2.7781792500
0.4209686745	2.9104735000
0.2307359168	3.0427677500
0.1216061283	3.1750620000
0.0290837967	3.4396505000
0.0054381495	3.7042390000
0.0010817183	3.9688275000
0.0007171921	4.2334160000
0.0000000000	4.4980045000

Th^{4+} shell Cu^{2+} shell

2798.2904604086	0.5291770000
190.2748932445	1.0583540000
110.3610195676	1.1906482500
65.7796625815	1.3229425000
39.4943453327	1.4552367500
23.5540894520	1.5875310000
13.8571789342	1.7198252500
8.0185293598	1.8521195000
4.5574657057	1.9844137500
2.5415862294	2.1167080000
1.3891328089	2.2490022500
0.7430189878	2.3812965000
0.3880269840	2.5135907500
0.1971057758	2.6458850000
0.0966874481	2.7781792500
0.0452541617	2.9104735000
0.0197187692	3.0427677500
0.0076400161	3.1750620000
0.0002914707	3.4396505000
-0.0001913202	3.7042390000

0.0002158135 3.9688275000
0.0003352866 4.2334160000
0.0000000000 4.4980045000

Th^{4+} shell La^{3+} shell

4814.6759959263 0.5291770000
345.3243889586 1.0583540000
200.4306039717 1.1906482500
119.1371044386 1.3229425000
72.0412617399 1.4552367500
44.2545606233 1.5875310000
27.5879899386 1.7198252500
17.3724174956 1.8521195000
10.9619734164 1.9844137500
6.8709443983 2.1167080000
4.2475811757 2.2490022500
2.5773484066 2.3812965000
1.5305050848 2.5135907500
0.8877876731 2.6458850000
0.5021085115 2.7781792500
0.2763373669 2.9104735000
0.1474588701 3.0427677500
0.0759753380 3.1750620000
0.0176071714 3.4396505000
0.0032363863 3.7042390000
0.0006439026 3.9688275000
0.0004623798 4.2334160000
0.0000000000 4.4980045000

Th^{4+} shell Nd^{3+} shell

4489.6702377637 0.5291770000
296.0552957920 1.0583540000
170.0969793970 1.1906482500
99.6966686254 1.3229425000
59.1547178144 1.4552367500
35.3314343031 1.5875310000
21.0739669061 1.7198252500
12.4332775475 1.8521195000
7.1961528634 1.9844137500
4.0641185153 2.1167080000
2.2332439551 2.2490022500
1.1921222224 2.3812965000
0.6173921394 2.5135907500
0.3097590533 2.6458850000
0.1502392394 2.7781792500
0.0703676021 2.9104735000
0.0317386812 3.0427677500
0.0138631499 3.1750620000
0.0025124095 3.4396505000
0.0004890394 3.7042390000
-0.0000157574 3.9688275000
-0.0002140554 4.2334160000
0.0000000000 4.4980045000

O^- shell Cu^{2+} shell (in La2cuo4)

542.8291015625	0.2997787595
60.8247833252	0.8289555907
36.7275238037	0.9612498283
22.0542755127	1.0935440063
13.1380167007	1.2258386612
7.7517919540	1.3581323624
4.5262231827	1.4904270172
2.6146736145	1.6227207184
1.4942407608	1.7550153732
0.8446859717	1.8873100281
0.4720715284	2.0196037292
0.2605223656	2.1518983841
0.1416594982	2.2841920853
0.0756292343	2.4164867401
0.0394121744	2.5487804413
0.0198574215	2.6810750961
0.0095092952	2.8133697510
0.0041861646	2.9456634521
0.0003365984	3.2102518082
-0.0003234644	3.4748411179
-0.0002783721	3.7394294739
-0.0001624316	4.0040178299
0.0000000000	4.2686061859

O^- shell La^{3+} shell (in La2cuo4)

882.1491699219	0.5926781893
87.1246337891	1.1218547821
54.1404876709	1.2541494370
34.6577301025	1.3864440918
22.5465850830	1.5187377930
14.7073554993	1.6510324478
9.5269546509	1.7833261490
6.0941724777	1.9156208038
3.8388853073	2.0479145050
2.3784275055	2.1802091599
1.4485931396	2.3125038147
0.8670775294	2.4447975159
0.5098738074	2.5770921707
0.2942909002	2.7093858719
0.1663907766	2.8416805267
0.0917963386	2.9739751816
0.0490405895	3.1062688828
0.0250140242	3.2385635376
0.0048163049	3.5031518936
-0.0003940270	3.7677402496
-0.0011931818	4.0323286057
-0.0009191367	4.2969169617
0.0000000000	4.5615053177

O^- shell O^{2-} shell (in La2cuo4)

28.7885589600 0.7702169418
20.3985900879 0.9025111794
14.5848379135 1.0348052979
10.4114532471 1.1670999527
7.3736085892 1.2993936539
5.1634817123 1.4316883087
3.5701894760 1.5639820099
2.4366798401 1.6962766647
1.6419744492 1.8285713196
1.0928792953 1.9608650208
0.7187412977 2.0931596756
0.4670983553 2.2254533768
0.2999058366 2.3577480316
0.1901011467 2.4900426865
0.1187970042 2.6223363876
0.0730198026 2.7546310425
0.0439856686 2.8869247437
0.0146257803 3.1515130997
0.0038843702 3.4161024094
0.0003951590 3.6806907654
-0.0004683670 3.9452791214
0.0000000000 4.2098674774

O^- shell Cu^{2+} shell (in Nd2cuo4)

542.8293977128 0.3254438550
60.8248052727 0.8546208550
36.7275292614 0.9869151050
22.0542845881 1.1192093550
13.1380197225 1.2515036050
7.7517944697 1.3837978550
4.5262247264 1.5160921050
2.6146748916 1.6483863550
1.4942407942 1.7806806050
0.8446862035 1.9129748550
0.4720715158 2.0452691050
0.2605222913 2.1775633550
0.1416593922 2.3098576050
0.0756291655 2.4421518550
0.0394122287 2.5744461050
0.0198572927 2.7067403550
0.0095094020 2.8390346050
0.0041861835 2.9713288550
0.0003366473 3.2359173550
-0.0003235842 3.5005058550
-0.0002784076 3.7650943550
-0.0001624725 4.0296828550
0.0000000000 4.2942713550

O^- shell La^{3+} shell (in Nd2cuo4)

844.7630581489 0.6244288600
87.5313366165 1.1536058600
53.5097939517 1.2859001100
32.7434580198 1.4181943600

19.8437503027	1.5504886100
11.8507585126	1.6827828600
6.9624811697	1.8150771100
4.0227794229	1.9473713600
2.2858766067	2.0796656100
1.2776780557	2.2119598600
0.7027630997	2.3442541100
0.3805791045	2.4765483600
0.2030135687	2.6088426100
0.1066491605	2.7411368600
0.0550838822	2.8734311100
0.0278608988	3.0057253600
0.0136700036	3.1380196100
0.0063941217	3.2703138600
0.0009644932	3.5349023600
-0.0001676433	3.7994908600
-0.0002443891	4.0640793600
-0.0001407006	4.3286678600
0.0000000000	4.5932563600

O^- shell O^{2-} shell (in Nd2cuo4)

28.7885738551	0.7702171235
20.3985897032	0.9025113735
14.5848408717	1.0348056235
10.4114549127	1.1670998735
7.3736108136	1.2993941235
5.1634839340	1.4316883735
3.5701901796	1.5639826235
2.4366804503	1.6962768735
1.6419748061	1.8285711235
1.0928799096	1.9608653735
0.7187414642	2.0931596235
0.4670985519	2.2254538735
0.2999059444	2.3577481235
0.1901012257	2.4900423735
0.1187970392	2.6223366235
0.0730198087	2.7546308735
0.0439856790	2.8869251235
0.0146257880	3.1515136235
0.0038843711	3.4161021235
0.0003951592	3.6806906235
-0.0004683670	3.9452791235
0.0000000000	4.2098676235

Appendix 4

The Kroeger-Vink Notation

The Kroeger-Vink (152,153) notation is used throughout this thesis to describe point defects, bound clusters and the substitution of impurities at lattice sites. For the case of a binary oxide of formula MO the defects that can be present are:

(a) vacant sites; vacant lattice sites on either of the crystal sub-lattices are given as $V_M^{''}$ and $V_O^{\cdot\cdot}$ where the superscripts refer to unit charges, ''' for negative and '·' for positive.

(b) interstitial ions; $M_i^{\cdot\cdot}$ or $O_i^{''}$ interstitials with the superscript referring to unit charges.

(c) misplaced ions and solutes; when an M ion is misplaced onto an O site it is represented as $M_O^{''''}$ where the subscript gives the type of site that M is on. If an impurity (I) with the same charge as the host ion substitutes at the host lattice site it is written as I_M^x. If the impurity is charged such as L^{3+} then is written as $L_M^{\cdot}$ and the superscript gives the appropriate charge with respect to the undoped site.

(d) free electrons and holes; in ionic materials, electrons are normally localised at a particular atom site in a way that can be described in terms of the ion valence. However, this might not always be the case and some fraction of the electrons, denoted $e^{'}$ may not be localised at a particular site. Similarly, missing electrons or holes are denoted by $h^{\cdot}$.

(e) bound impurities; defects might associate to form a cluster. These are indicated by bracketing the components of such a cluster. e.g. $(V_M^{''}V_O^{\cdot\cdot})^x$.

Appendix 5

Figures A5.1 to A5.15 are sketches of the {n10} (n=1,2) and the {10m} (m=1,2,3,4,5,6) surfaces of La_2CuO_4 and Nd_2CuO_4. Not that in these figures, copper, lanthanum, neodymium and oxygen are represented by:

- ● Cu
- ⊘ La/Nd
- ○ O

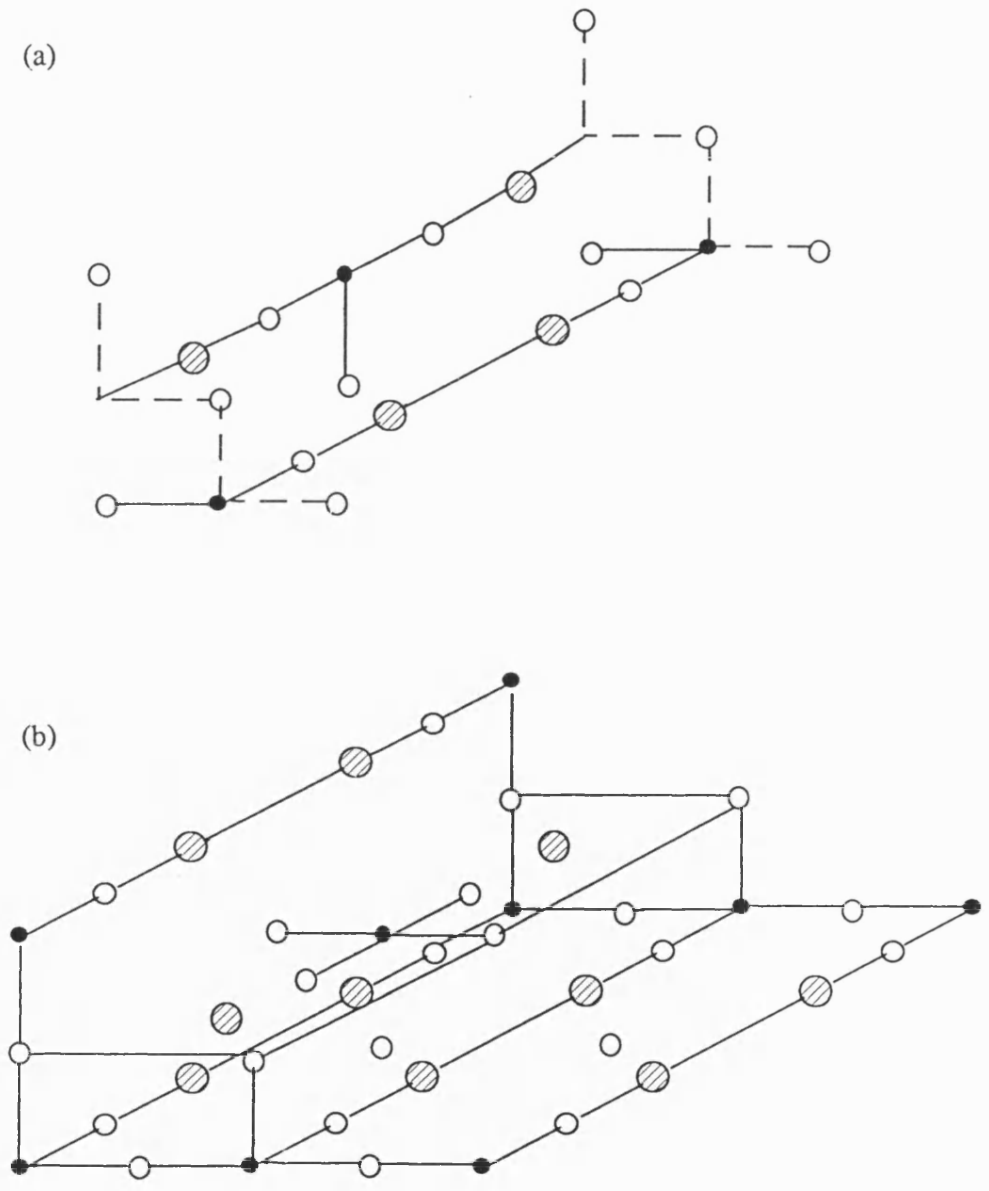

Figure A5.1: Sketches of (a) the {110} and (b) the {210} surfaces of La_2CuO_4

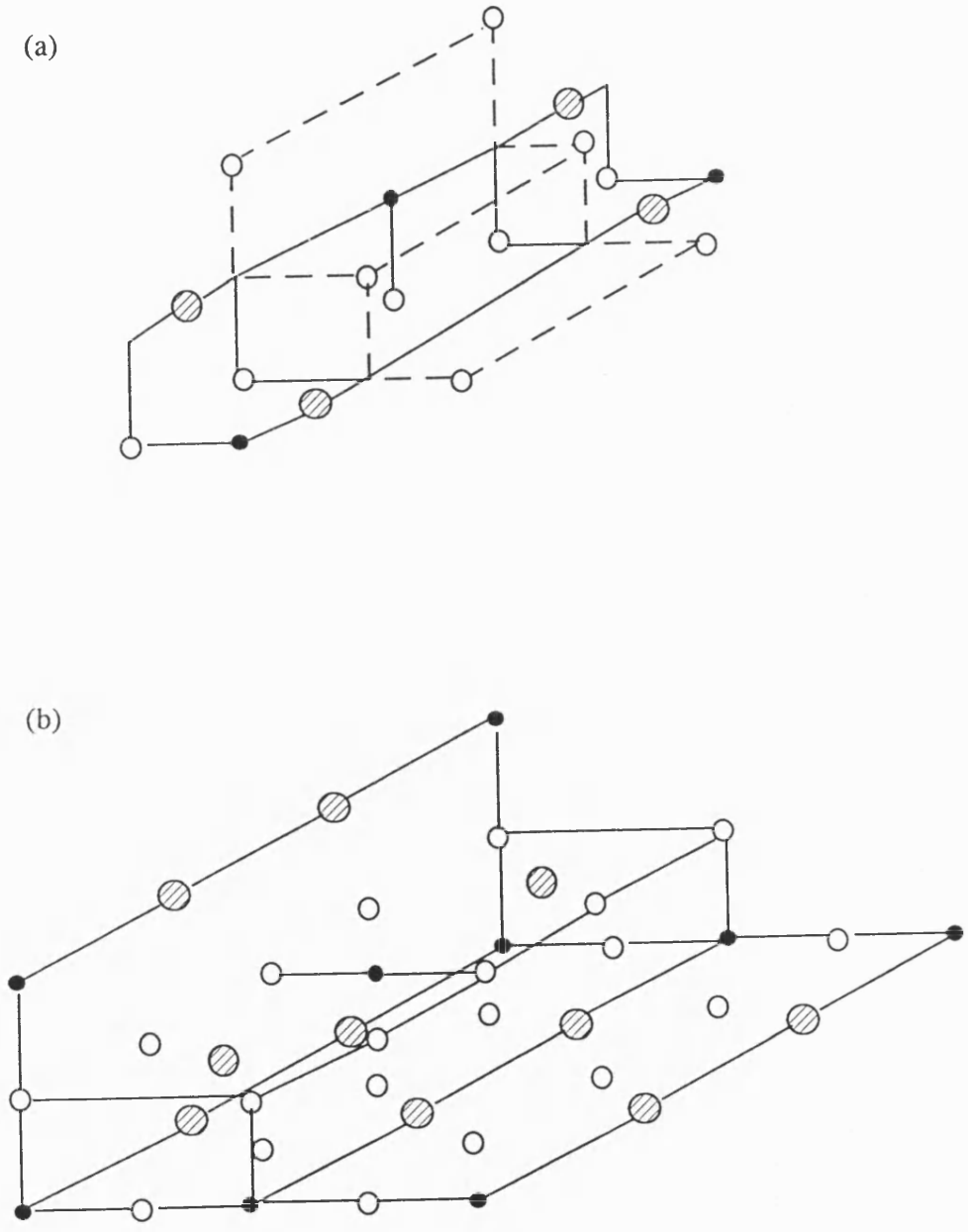

Figure A5.2: Sketches of (a) the {110} and (b) the {210} surfaces of Nd_2CuO_4

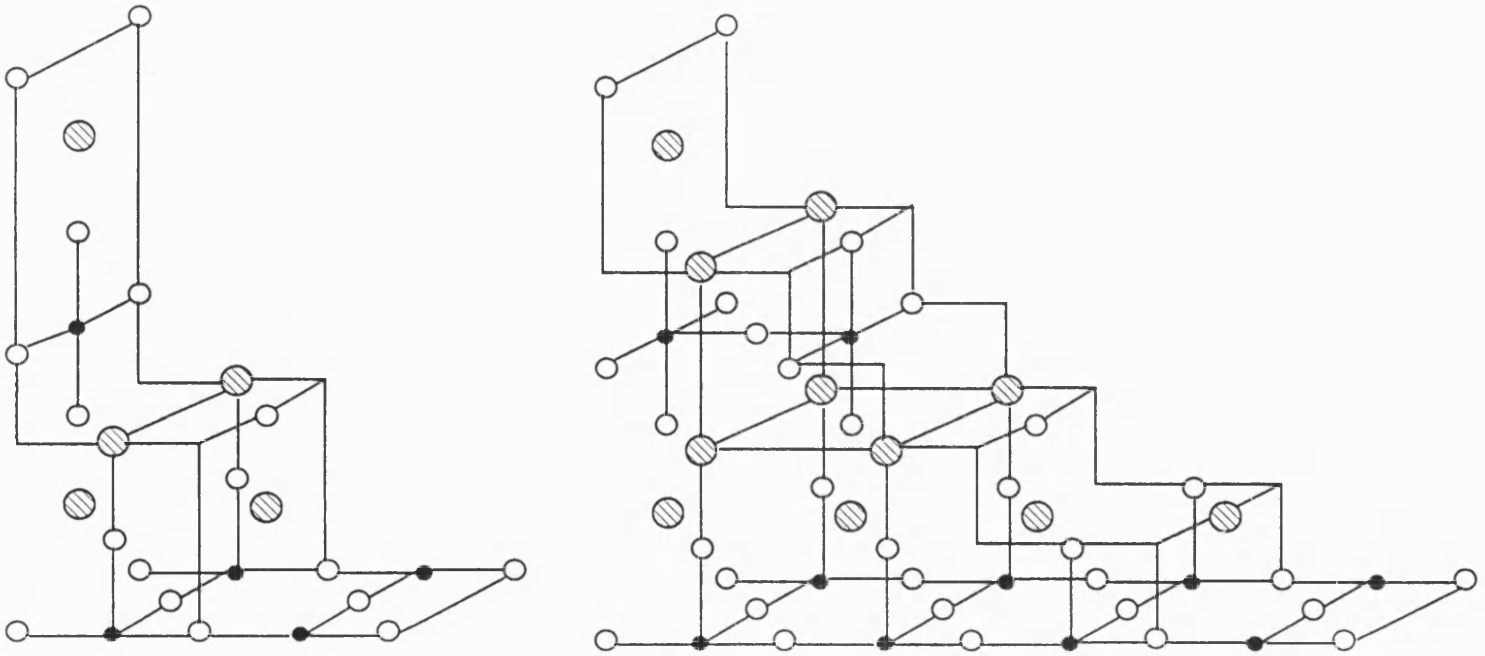

(a) (b)

Figure A5.3: Sketches of (a) the {102} and (b) the {104} surfaces of La_2CuO_4

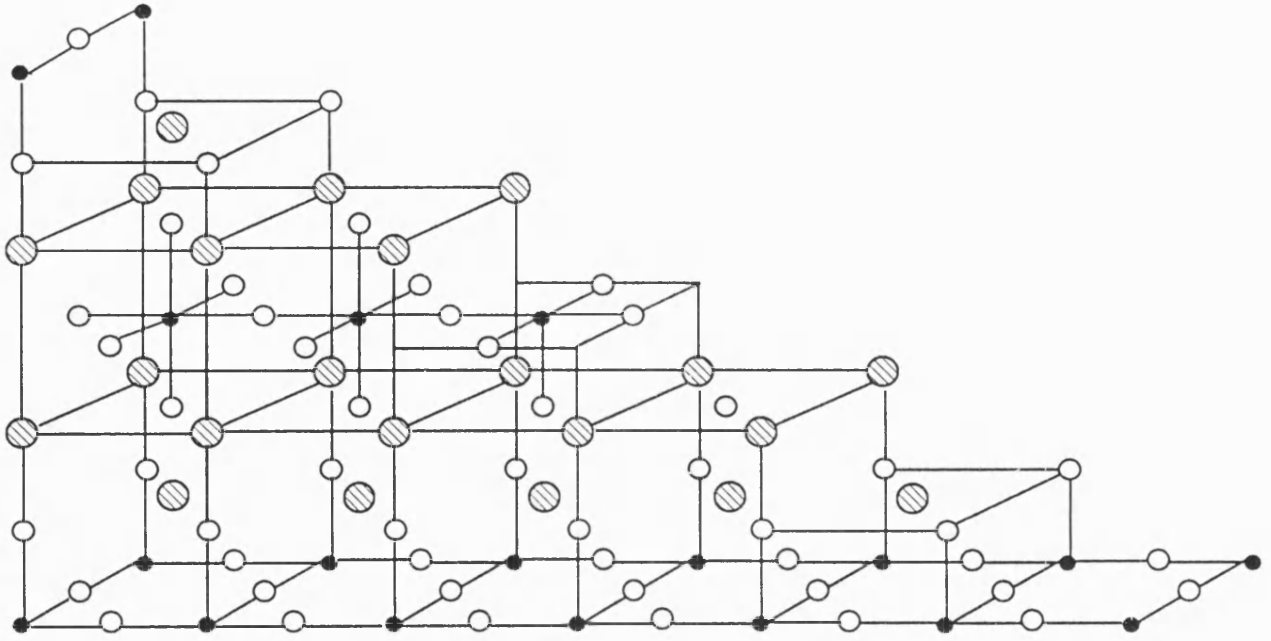

Figure A5.4: Sketch of the {106} surface of La_2CuO_4

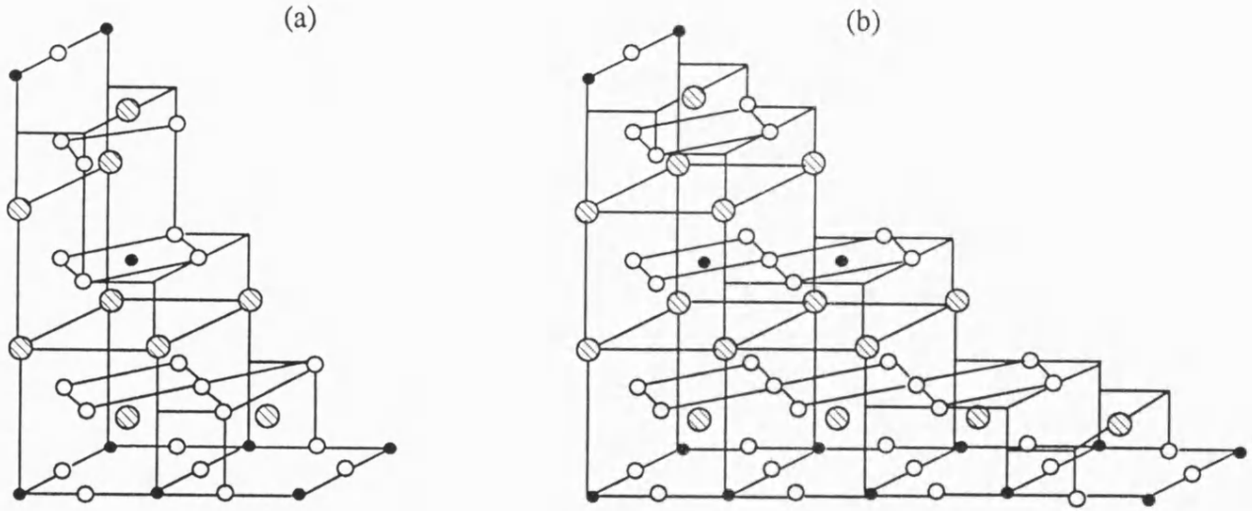

Figure A5.5: Sketches of (a) the {102} and (b) the {104} surfaces of Nd_2CuO_4

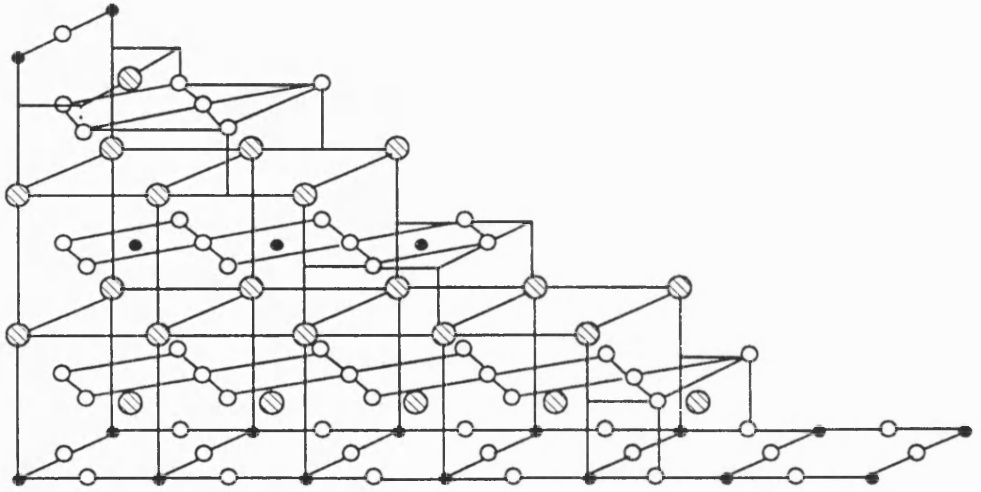

Figure A5.6: Sketch of the {106} surface of Nd_2CuO_4

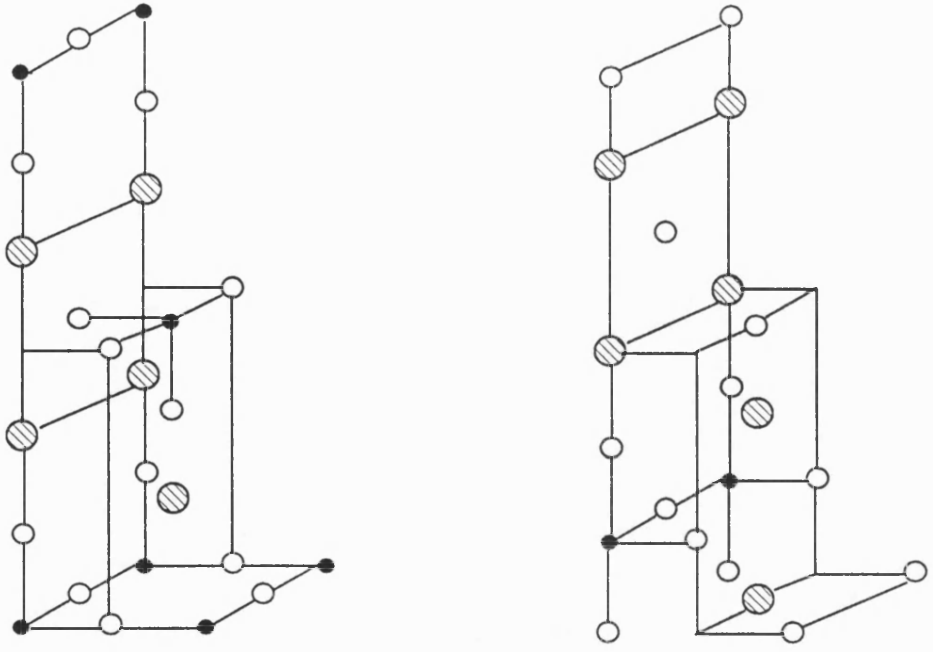

OCu termination

O termination

Figure A5.8: Sketches of the {101} surfaces of La_2CuO_4

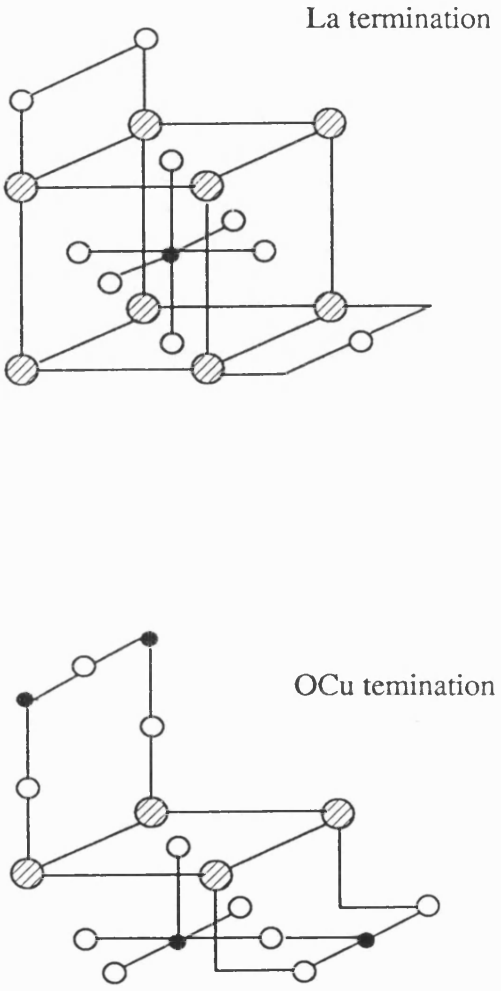

Figure A5.9: Sketches of the {103} surfaces of La_2CuO_4

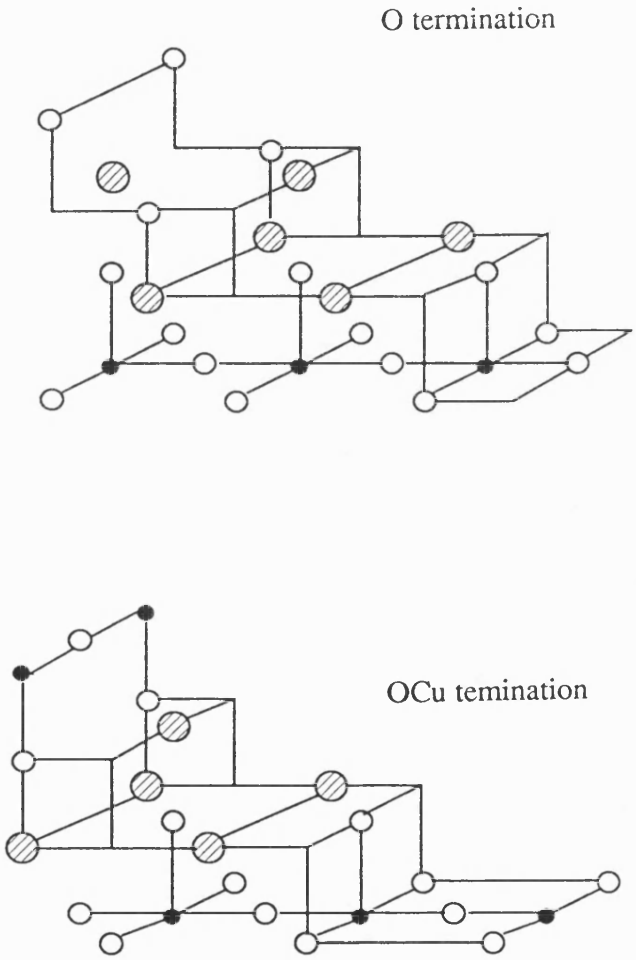

Figure A5.10: Sketches of the {105} surfaces of La_2CuO_4

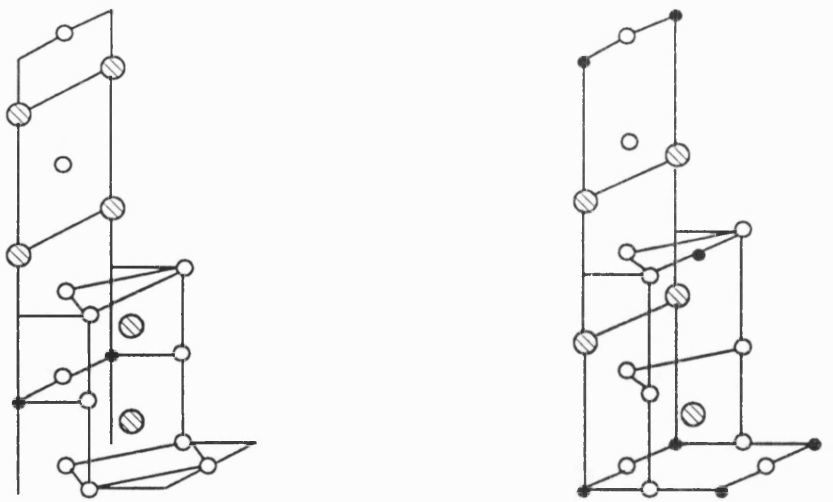

O termination

OCu termination

Figure A5.11: Sketches of the {101} surfaces of Nd_2CuO_4

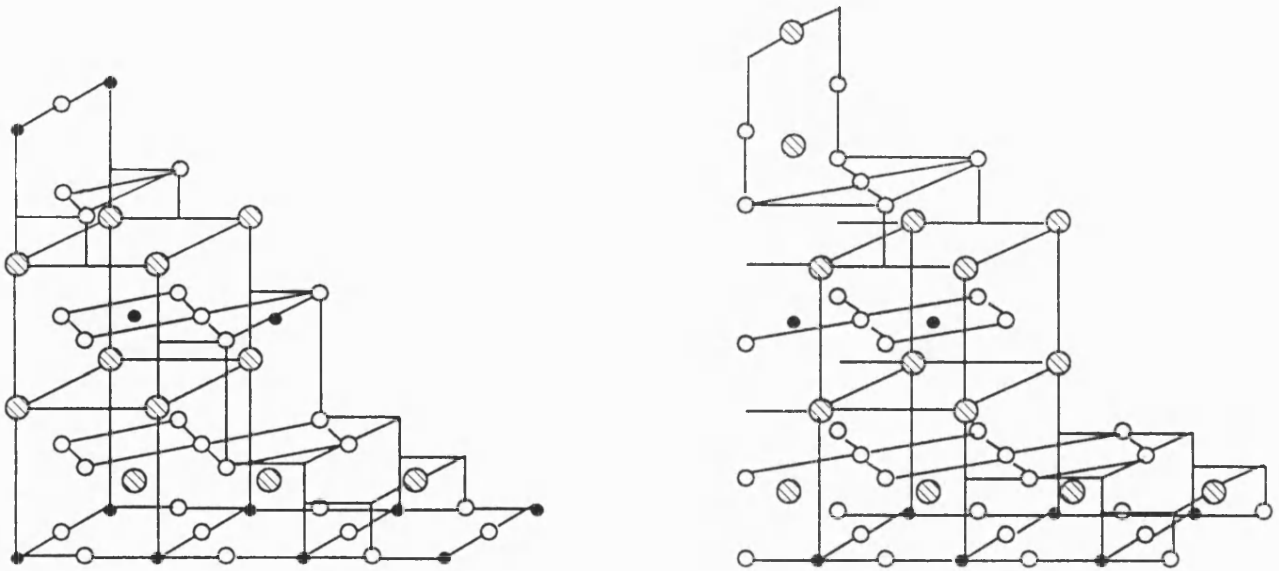

OCu termination

Nd termination

Figure A5.12: Sketches of the {103} surfaces of Nd_2CuO_4

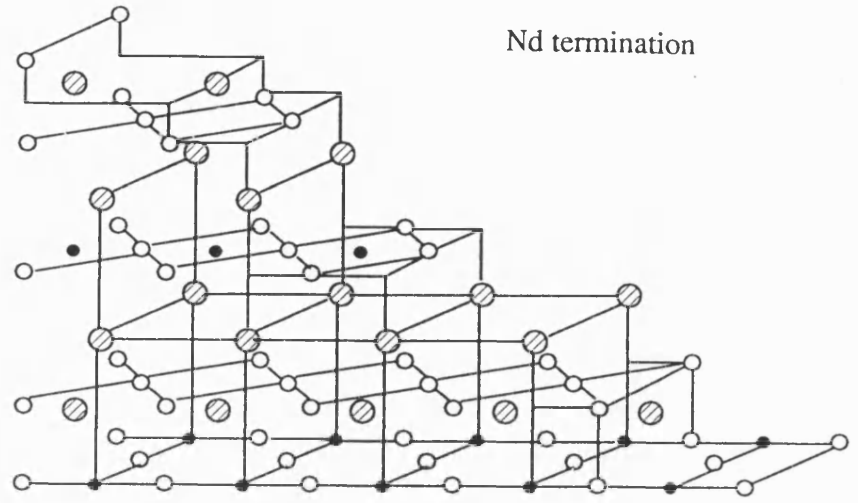

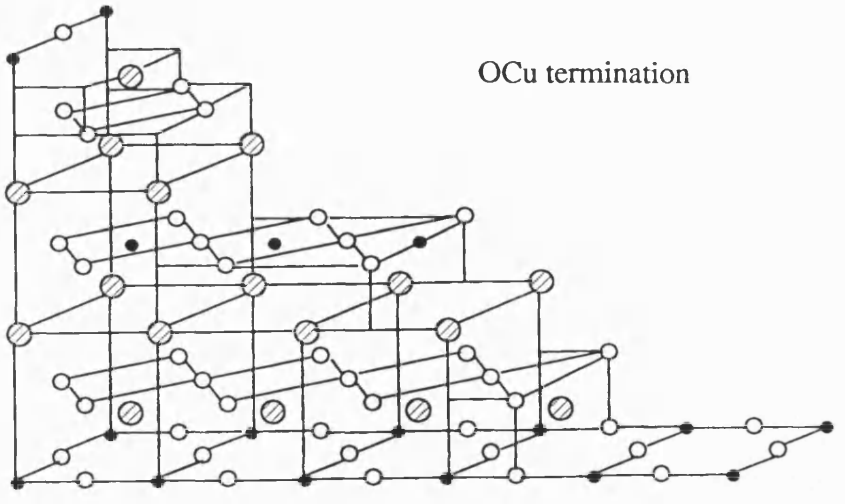

Figure A5.13: Sketches of the {105} surfaces of Nd_2CuO_4

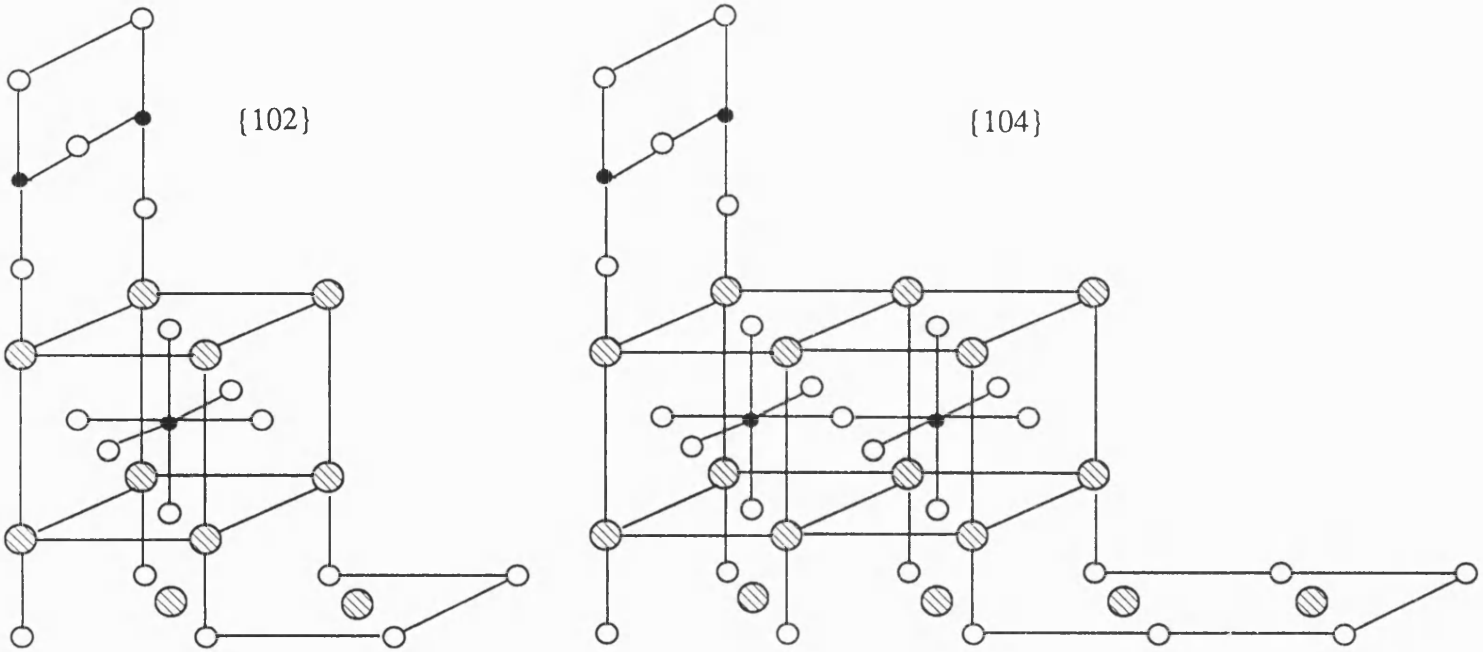

Figure A5.14: Sketches of the reconstructed {102} and {104} surfaces of La_2CuO_4

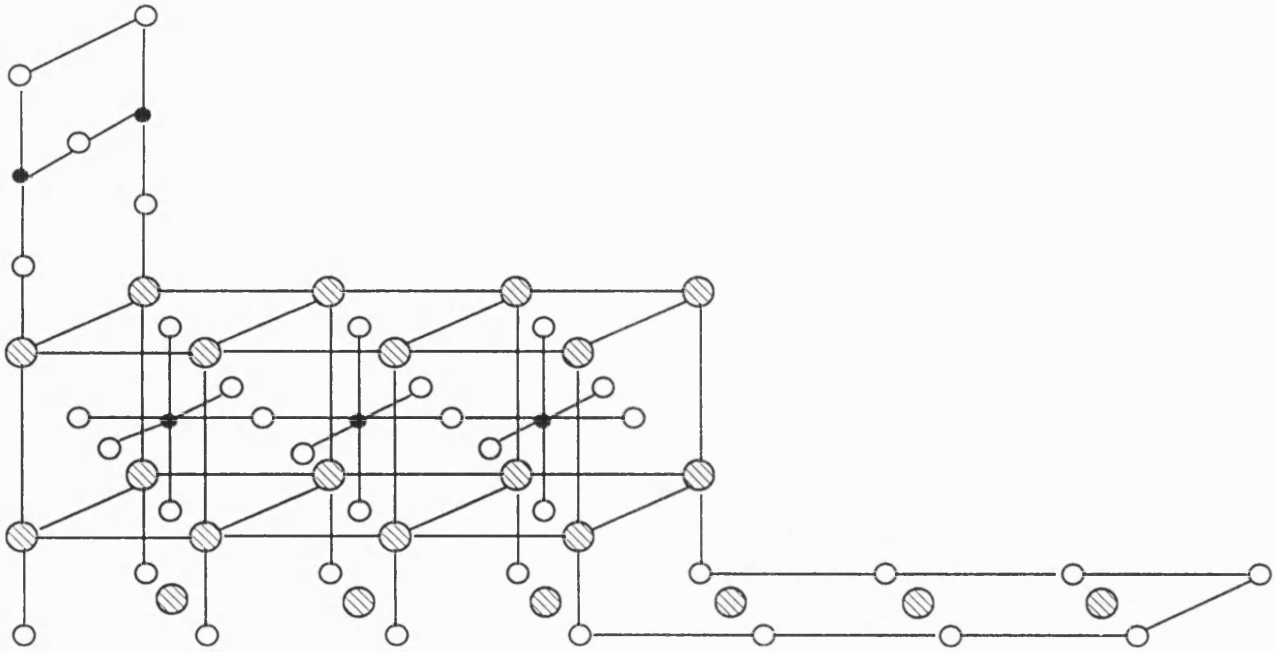

Figure A5.15: Sketch of the reconstructed {106} surface of La_2CuO_4